UNIVERSITÀ DEGLI STUDI DI PADOVA

Department

of Civil, Environmental and Architectural Engineering

Water and Geological Risk Engineering Program

Master Thesis

Adjustment of Depth-Duration-Frequency Curves Under Changing Climate

Rashid Akbary
(2039971)

Supervisors

Professor Marco Marani,

Department of Civil, Environmental and Architectural Engineering

Professor Marco Borga,

Department of Land, Environment, Agriculture and Forest,

Academic Year 2022/23

Dedication

To my beloved mother, Robaba Mohammadi, whose memory continues to inspire and guide me each day, and to my steadfast father, M. Ibrahim Akbary, for his unwavering love and support.

Acknowledgement

I would like to express my deepest appreciation to my supervisors, Professor Marco Marani, and Professor Marco Borga for their persistent direction, support, and mentorship throughout the course of this dissertation. Their insights and patience have been invaluable in shaping this work

Abstract

The impact of climate change on extreme rainfall events presents a critical challenge for urban planning, agriculture, and water resource management. This study aims to redefine Depth-Duration-Frequency (DDF) curves under changing climate conditions, focusing on the Veneto region in Northern Italy. Utilizing data from 29 rain gauge stations, we observed significant variability in rainfall patterns, which raises questions about the applicability of traditional, stationary DDF curves for future infrastructure planning. To improve the predictive capability of DDF curves, we employed Convection-Permitting Models (CPMs) and compared their outputs with observational data. While initial comparisons revealed biases in the CPMs, bias-correction techniques significantly improved the model's alignment with observational data.

Our results indicate that there is a projected increase in 1-hour rainfall across a range of return periods by the year 2100. Specifically, increases ranged from 29% to 66% for various return periods after bias-correction. The study reveals that traditional methods based on the Clausius-Clapeyron relation may not be sufficient for capturing the nuances of extreme rainfall events, highlighting the importance of CPMs in future climate projections.

The findings underscore the need for region-specific climate adaptation strategies and pave the way for more robust, climate-resilient infrastructure planning. These insights are not just pertinent for Northern Italy but could be indicative of larger, global patterns, emphasizing on how we approach climate change mitigation and adaptation.

Table of Contents

List of Figures

Chapter 1

1. Introduction

The rising occurrence of extreme weather events due to climate change continues to have severe societal implications, particularly for urban and rural development, public infrastructure, agriculture, and human health (Mailhot & Duchesne, 2010; Rosenberg et al., 2010). Extreme rainfall events are of particular interest due to its potential to increase in both intensity and frequency as a result of global warming (Bao et al., 2017; Fischer & Knutti, 2015; Prein et al., 2017).

Local depth-duration-frequency (DDF) curves are fundamental to the design of most hydraulic engineering structures. These curves are designed to reflect the statistical characteristics of precipitation and to represent the extreme rainfall depth (mm) for various time spans (ranging from minutes to days) and average recurrence intervals (years). Typically, precipitation depth for different durations are estimated by fitting a theoretical probability distribution to annual maximum (AM) precipitation samples or peaks over threshold (POT) samples. DDF curves for urban and small-catchment applications usually refer to rainfall durations between about 5 minutes and 24 hours and return periods ranging from 2 to 100 years (Martel et al., 2021). Currently, the derivation of DDF curves for engineering design predominantly rests on the assumption of stationarity in extreme rainfall properties (Arnbjerg-Nielsen et al., 2013; Cheng & AghaKouchak, 2014). However, this concept is increasingly challenged by our improved understanding of the climate system. Long-term interannual variability due to variability inherent to the climate system, including phenomena like the Atlantic Multidecadal Oscillation and the El Nino Southern Oscillation, has been shown to decisively impact rainfall and temperature patterns (Milly et al., 2008). More importantly, anthropogenic emissions of greenhouse gases

(GHG), are modifying the global water cycle in ways that are now known to significantly modify the frequency and intensity of extreme rainfall events (Mamoon et al., 2019; Myhre et al., 2019). Studies have documented marked increases in the magnitude of daily rainfall during the second half of the 20th century (Min et al., 2011), and further escalation in rainfall extremes is anticipated in future decades (Donat et al., 2016). Short-duration rainfall is showing even more marked increases in the frequency of severe events (Dallan et al., 2022; Fowler, Ali, et al., 2021; Fowler, Wasko, et al., 2021; Westra et al., 2014).

The increase in daily and sub-daily extreme rainfall, both observed and projected, raises doubts about using historical DDF curves for future civil infrastructure planning. An erroneous assumption about possible changes in DDF curves can result in inadequate infrastructure that is vulnerable to failure (under-design) or can lead to costly overdesign. Thus, there is a pressing need to define how information about the changing climate can be incorporated into the development of DDF curves representing the future extremes impacting water infrastructure (Schlef et al., 2023).

An approach proposed for assessing the possible changes in DDF curves is through the use of simulated projections from climate models which is a method grounded in physical principles but affected by significant model uncertainties. A critical aspect of this approach is the model ability to describe changes in rainfall, and particularly in their extremes. This ability hinges heavily on whether climate models can successfully represent convective processes, responsible for rainfall generation, particularly at small spatial and temporal scales. Convective processes generate rainfall patterns at scale of a few kilometers, such that the resolution of climate models used for these objectives need to be of the same order of magnitude (Berg et al., 2019). This requirement contrasts with the typical resolution of Global and Regional Climate Models, most often measured in tens of kilometers. However, in the past decade, a new generation of Convection-Permitting Models (CPMs) has been developed, which operate at horizontal resolutions $\leq$4 km, thereby representing a potentially powerful tool for modeling shorter-duration rainfall extremes (Meredith et al., 2021) (Barlage et al. 2021). The potential of CPMs to offer a detailed and sophisticated depiction of such extremes in Northern Italy is a promising avenue for enhanced water management and risk mitigation strategies.

This study leverages recent advancements in CPMs to define how these can be used to redefine DDF curves under changing climate conditions, with particular reference to Veneto region in Northern Italy. First, I seek to evaluate the hypothesis that an upward shift and steepening trend can be detected in the DDF curves under a global warming scenario. Second, my objective is to understand if the alterations observed are dependent upon the return period. My third and last objective is to elucidate any potential connection between projected changes in the return levels of the DDF curves and the degree of local increase of temperature. Answers to these questions are essential to clarifying and quantifying the impacts of climatic changes on extreme rainfall events, and, therefore, to developing a robust basis for assist in designing climate-proof infrastructure.

The Thesis is organized as follows. Chapter 2 will present the methodology and theoretical background of the work. Chapter 3 will be dedicated to presenting the results, and Chapter 4 will present a discussion of the results and some conclusions.

Chapter 2

2. Theory and Methods

2.1. Precipitation Physics Background

The process of precipitation generation is initiated by the evaporation of water, transforming it into water vapor in the atmosphere. When subject to cooling processes, associated with buoyancy-driven or forced lifting, this vapor may condense around nucleation aerosol particles. This results in cloud formation, and, if conditions are suitable for drop growth, rain falls from these clouds due to gravity (Martel et al., 2021). Depending on the lifting processes at play two main precipitation types may be produced (Poujol et al., 2021).

a. Stratiform precipitation: This precipitation type is defined as a process in which the vertical air motion is generally small compared to fall velocity of ice crystals and snow.
b. Convective precipitation: In the convective precipitation process, the vertical air motion is generally large compared to fall velocity of ice crystals and snow. For instance, the mean vertical air velocity at a given height in the updraft zone has a magnitude of w ~ 1-10 m/s, which equals or exceeds the typical fall speeds of ice crystals and snow.

Because all the above processes depend on the amount of moisture that the atmosphere can hold and may be subject to condensation, a potential dependence of precipitation on temperature becomes immediately evident. According to the thermodynamic-based Clausius-Clapeyron relation, the amount of water vapor that can be held by an air parcel at

saturation is an increasing function of temperature. Hence, in a world that is projected to be warmer, more water vapor will be present in the atmosphere, potentially resulting in an increase in the amounts of precipitation delivered by the two kinds of rainfall-generating mechanisms (Trenberth et al., 2003). Among these types, convective precipitation, chiefly responsible for extreme precipitation events within sub-daily periods, is expected to experience the greatest increase (Dai et al., 2020).

2.1.1. The Thermodynamic and Dynamic Mechanisms of Extreme Precipitation

Understanding the physical processes behind extreme precipitation events is essential for their prediction under a changing climate. To first order, the effects of climate change on extreme precipitation mechanisms has been suggested to be controlled by thermodynamics and by circulation mechanisms. Thermodynamic considerations are based on the Clausius-Clapeyron (CC) equation, which is given as:

$$\frac{\partial s_e}{s_e} = \frac{L_v \partial T}{R_v T^2} \qquad (1)$$

Here s_e represents the saturation water vapor pressure at temperature T (degree Kelvin) (the absolute atmospheric temperature). L_v stands for the latent heat of vaporization, and R_v is the gas constant. This notion suggests that increasing temperatures increases the air water-holding capacity by about 7% per degree Celsius (Fischer & Knutti, 2015). Because rainfall extremes are constrained by the level of moisture availability in the atmosphere, it is initially anticipated that changes in rainfall intensities will correspond with the CC relation (Trenberth et al., 2003). This notion has guided much recent and ongoing research on extreme precipitation changes (Drobinski et al., 2016, 2018; Hardwick Jones et al., 2010; Singleton & Toumi, 2013; Utsumi et al., 2011).

Based on the rationale behind the CC relationship we can compute the future rain intensities according to most likely local increase in temperatures by the following formula (Martel et al., 2021):

$$I_{fut} = I_{ref}\left[\frac{100+R_{sc}}{100}\right]^{\Delta T} \quad (2)$$

Where I_{ref} and I_{fut} refers to reference and future rain intensities. R_{sc} is the rainfall scaling factor based on CC relationship (%/℃), and ΔT indicates the projected difference in local temperature. In implementing of the above formula, several guidelines (CSA, 2019; ARR; Ball et al. 2019) recommend using a value of 5 to 7% for the R_{sc}.

However, the literal interpretation of CC scaling as the main, if not the only, mechanism controlling extreme precipitation is debatable and debated. It was empirically observed that an increase in water-holding capacity does not necessarily lead to more rainfall and several studies found extreme precipitation deviating from the CC relationship in many regions, with changes in the intensity of sub-daily extreme precipitation reaching twice the CC rate in mid-latitude areas (Lenderink et al., 2011; Westra et al., 2014). In contrast, some regions even exhibit decreasing precipitation intensity with warming (Lenderink & Fowler, 2017). Additionally, precipitation types and event durations also influence this correlation (Berg & Haerter, 2013; Wasko et al., 2015).

The dynamic mechanisms responsible for atmospheric vapor transport, on the other hand, must also play a role, which has not yet been thoroughly described (O'Gorman, 2015). These mechanisms have the potential to create conditions conducive to rapid water condensation, thereby controlling the occurrence of various weather systems (Liu et al., 2020; Trenberth, 1999). As our understanding of these dynamics continues to evolve, it becomes more important to grasp their influence on extreme rainfall events under changing climate conditions.

Recent research into extreme rainfall events provides evidence of their likely increase in both intensity and frequency across various timescales. The magnitude of these changes, however, can be region-dependent, thus underscoring the need for a deeper understanding of both thermodynamic and dynamic mechanisms at play in a warming climate (Dallan et al., 2022; Formetta et al., 2022; Fosser et al., 2020; Myhre et al., 2019).

2.1.2. Climate Models and Their Ability to Simulate Extreme Rainfall

Climate models offer a comprehensive view of precipitation extremes on a global scale (Sun et al., 2007), along with more detailed analyses at the regional level (Ban et al., 2014). These models can be utilized to explore various emissions scenarios or specific radiative forcings (Chen et al., 2011; Kodra et al., 2011), and may support investigations into the dynamics of precipitation generation (O'Gorman & Schneider, 2009). However, there are notable constraints in climate model ability to accurately reproduce precipitation extremes, particularly at sub-daily scales. These limitations are partly due to the employment of parameterized convection, a method used to depict deep convection (the vertical transport of air masses over large vertical distances; above the 500 hPa pressure level) occurring on scales smaller than the grid size (Kharin et al., 2007; Kooperman et al., 2014; Wehner, 2013).

Climate models can be categorized into global or regional types. Global models, known as Global Climate Models (GCMs), encompass the entire Earth and typically have resolutions spanning hundreds of kilometers, allowing them to depict broad-scale climate patterns. On the other hand, Regional Climate Models (RCMs) focus on particular areas and offer more detailed resolutions, often around tens of kilometers. This granularity aligns more with actual observations of aspects like topography, land cover, and soil varieties, all of which influence the climate. However, the temporal and spatial resolutions of both GCMs and RCMs are too coarse to directly assess future changes in sub-daily precipitation. To achieve the needed granularity, it becomes essential to employ downscaling and bias correction to refine the outputs to the desired spatial and temporal scales. Given that GCMs and RCMs usually possess resolutions of 10 km or even coarser, they depend on parameterizations to account for subgrid-scale processes. The parameterization of convection, which is vital for these smaller-scale processes, introduces a known source of uncertainty, affecting the model ability to accurately simulate rainfall extremes (Berg et al., 2019). While the limitations and uncertainties in modeling precipitation extremes, particularly at sub-daily scales, are known, it is also essential to recognize the contributions of Global and Regional Climate Models in describing the earth system at large scales.

Shifting our focus to a daily timescale, investigations utilizing multiple Global Climate Models (GCMs) indicate their consistent prediction of changes in heavy rainfall under climate change scenarios. Increases are estimated to be about 7%/°C at midlatitudes (Fischer et al., 2014), consistent with CC scaling. Further analysis by Fischer and Knutti (2015) estimated that up to 18% of heavy daily rainfall could be linked to observed temperature increases, with attribution percentages growing with more intense warming. Bao et al. (2017) and Tabari (2020) emphasized the skill of Regional Climate Models (RCMs) in reproducing observed apparent scaling and in projecting future rainfall intensities and frequencies that surpass observed rates, with increases between 6% and 15% depending on RCM configurations. Pfahl et al. (2017) break down daily heavy rainfall into its thermodynamic and dynamic elements, illustrating that the thermodynamic component alone would result in a uniform increase of approximately 7%/°C across various GCMs. In contrast, atmospheric vapor transport dynamics bring about a modification in regional responses, intensifying the increases in places like the Asian monsoon region, while diminishing them in areas such as the Mediterranean and South African regions. This analysis underscores the intricate nature of rainfall patterns and of their response to both consistent thermodynamic factors and varying regional dynamics. Additional research by Kharin et al. (2013) and Martel et al. (2020) showed an anticipated 3- to 4-fold increase in the frequency of extreme rainfall events in the future. However, it is known that rainfall processes are not explicitly represented at the coarse spatial scales characterizing GCMs, and hence these conclusions cannot be considered to be final.

These complexities in the representation point to the need for refined modeling, especially in the realm of sub-daily precipitation. Rainfall events with sub-daily duration are projected to increase in future scenarios. However, their proper model representation requires short model temporal resolution (sub-hourly to hourly) and high-resolution discretizations (order of one to a few kilometers).

2.1.3. Convection Permitting Models

In the past decade, the emergence of convection-permitting climate models (CPM), with horizontal resolutions of 4 km or less, has greatly enhanced our ability to simulate short-duration rainfall extremes, even at sub-hourly levels (Meredith et al., 2021). This advancement has significant implications for water management practices (Orr et al., 2021). Within these fine spatial resolutions, deep convection is explicitly modeled, rendering the need for deep convection parameterization in CPMs unnecessary (Fosser et al., 2020; Westra et al., 2014). Compared to RCMs, which operate at horizontal resolutions ranging from 10 to 50 km, CPMs provide substantial benefits in modeling rainfall extremes on hourly scales and the daily pattern of rainfall (Ban et al., 2014; Fosser et al., 2015; Kendon et al., 2014; Lind et al., 2020).

This enhancement in rainfall representation makes CPM results potentially more robust in describing future changes in climate. Several studies utilizing CPMs have unveiled a growing intensification of hourly rainfall extremes across various regions. This tendency has been identified in simulations for the UK (Fosser et al., 2020; Kendon et al., 2014), the Alps (Ban et al., 2015, 2020), Belgium (Vanden Broucke et al., 2019) , and Germany (Knist et al., 2020), indicating a trend that is both consistent and widespread. Significantly, CPMs reveal a more pronounced intensification of forthcoming extreme precipitation compared to RCMs (Kendon et al., 2014).

However, CPMs are still relatively new and considered to be in a developmental stage. CPM runs have been found to be affected by bias, such as overly intense precipitation (Kendon et al., 2014), or overly dry and warm conditions over specific continental areas (Barlage et al., 2021; Berthou et al., 2020). Despite these limitations, the lack of accessible high-resolution gridded datasets, both spatially and temporally, hinders the widespread application of bias correction, a commonly recommended solution to these biases (Argüeso et al., 2013). Furthermore, until recently, a comprehensive assessment of the uncertainties remained unattainable, largely due to the substantial computational costs associated with running ensembles at such high resolution.

2.1.3.1. Bias Correction Method

Bias correction is a technique used to establish a correspondence between observed historical rainfall data and the rainfall data generated by climate prediction models. The essence of this process is to apply a mapping that transforms the distribution of historical rainfall from the model to closely mirror the observed historical rainfall distribution. Once established, this mapping can be subsequently used to adjust future rainfall data predicted by the climate model to eliminate bias, thereby yielding more accurate future rainfall sequences. In this study, I am implementing a popular bias correction methodology known as Quantile Mapping (henceforth referred to as QM).

The QM approach is widely utilized for minimizing systematic discrepancies in various meteorological variables, such as precipitation and temperature, obtained from climate models (Cannon, 2008). The principle behind QM is the creation of a transfer function that most accurately maps the model's cumulative density function (CDF) of the variable onto the CDF derived from observational data (Gudmundsson et al., 2012).

The QM process entails estimating the cumulative density functions for observed (F_0) and modeled (F_m) historical rainfall amounts. These estimates are then combined to form a transformation function defined as:

$$x_{Corr} = {F_0}^{-1}[F_m(x_m)] \qquad (3)$$

In this equation, x_m stands for the rainfall intensity as predicted by the climate prediction model, whereas x_{Corr} represents the bias-corrected rainfall intensity. The transformation function ${F_0}^{-1}[F_m]$ consequently yields the observed distribution (or an approximation thereof, depending on the methodology) when applied to the historical time series from the model. When this function is applied to the future time series predicted by the model, it produces a bias-corrected future scenario. In summary the following steps were taken place to implement the QM:

a) The CDFs for both the observed (F_0) and modeled (F_m) historical rainfall data are computed.

b) Using the computed CDFs, a transfer function is created that maps F_m onto F_0.
c) The transfer function is applied to the modeled historical data to ensure that it closely approximates the observed historical data.
d) The transfer function is applied to the future rainfall data predicted by the climate model to obtain bias-corrected future rainfall estimates.

2.2. Statistical and Probabilistic Methods

In order to advance the accuracy of future projections of short-duration rainfall extremes, some existing work suggests the combination of convection-permitting models with sophisticated statistical methodologies that optimally exploit shorter records (Zhang et al., 2017). Responding to this recommendation, this thesis proposes the utilization of the Metastatistical Extreme Value Distribution (MEVD), as proposed by Marani and Ignaccolo (2015). The MEVD approach suggests that the nature of extreme events is shaped by the repeated sampling of the ordinary events. Once the distribution of these ordinary events is determined, the distribution of extremes, defined as yearly maxima, becomes a function of this foundational distribution and of the number of times it is sampled every year (Zorzetto et al., 2016). This approach not only relaxes the asymptotic assumption of the traditional extreme value theory, but also leverages the whole available set of data, rather than relying solely on annual maxima or on a few peaks over a high threshold, as in the case of the Generalized Extreme Value Distribution (GEV). This dual advantage significantly reduces the uncertainty in parameter estimation (Zorzetto et al., 2016).

2.2.1. The Conventional Extreme Value Theory

In traditional Extreme Value Theory (EVT), extremes are identified as "block maxima", meaning the events that have the highest magnitude x within a fixed-length period (frequently 1 year). The ‘n’ events that happen within each block are presumed to be

independent, and their magnitude to adhere to the same overarching cumulative distribution F(x). This notion of block maxima and the underlying assumptions about event independence and distribution within EVT lay the foundation for more specific analyses of extreme values. When analyzing a specific event duration of interest, the study of extreme value often focuses on the distribution of annual maxima, either by evaluating it directly or by examining the distribution of rainfall values exceeding a high threshold (Davison & Smith, 1990).

The traditional Extreme Value Theory (EVT) recognizes a Generalized Extreme Value (GEV) distribution for yearly maxima, under the assumptions that rainfall intensity is independent and identically distributed (i.i.d.), and that the number of occurrences per year tends towards infinity (Fisher & Tippett, 1928; Gumbel, 1958; Jenkinson, 1955). Because of the latter hypothesis, this formulation is often said to be an asymptotic one. The formulation of the GEV distribution encompasses the special cases of the Gumbel, Fréchet, and Weibull distributions. The GEV cumulative distribution function can be articulated as follows (Coles, 2001):

$$\zeta_{GEV}(x) = exp\left\{-\left(1+\xi\left(\frac{x-\mu}{\sigma}\right)\right)^{\frac{-1}{\xi}}\right\}, \qquad (4)$$

where $\zeta(x)$ is defined for $1+\xi\left(\frac{x-\mu}{\sigma}\right) > 0$; elsewhere, $\zeta(x)$ is either 0 or 1 (Smith, 1989). The GEV distribution is characterized by three parameters: the location parameter (μ), which specifies the central tendency of the distribution; the scale parameter (σ), which details the deviation around μ; and the shape parameter (ξ), which describes the tail behavior of the GEV distribution. Depending on the value of ξ, the GEV may correspond to different distributions: when ξ tends to 0, it leads to the Gumbel distribution; when $\xi <$ 0, it results in the Weibull distribution; and when $\xi >$ 0, it gives rise to the Fréchet distribution. GEV parameters are often estimated using a Maximum Likelihood approach (Otten & Van Montfort, 1980; Prescott & Walden, 1980) or using L-moments (Hosking, 1990).

Another approach to EVT theory, closely related to GEV, involves examining the distribution of rainfall values exceeding a certain threshold known as the peak over threshold (POT) approach (Balkema & De Haan, 1974; Pickands, 1975). The POT method involves setting a high-intensity threshold, and then presuming a Poisson distribution for occurrences of events that surpass this threshold, then it models these values by employing a generalized Pareto distribution (GPD). This GPD distribution is a widely-used tool for modeling time series based on the POT method and has been applied to diverse fields such as precipitation (De Michele, 2003), earthquake data (Pisarenko & Sornette, 2003), wind speed (Holmes & Moriarty, 1999), and economic data (Gençay & Selçuk, 2004), among others. Given a sequence Y of independent and random variables, for a large enough threshold u, the cumulative distribution function of the excesses $Y_e = Y - u$, conditional on $Y > u$, is approximated by the GPD (Coles, 2001):

$$\zeta_{GPD}(y_e) = 1 - \left(1 + \xi\left(\frac{y_e}{\sigma}\right)\right)^{\frac{-1}{\xi}}, \qquad (5)$$

where ξ and σ are the shape and the scale parameters, respectively. The interarrival of exceedances is assumed to be exponentially distributed (Poisson process). The parameters involved in the POT approach are often estimated using a Maximum Likelihood approach (Grimshaw, 1993). It may be shown that the POT approach with Poisson exceedance arrivals leads again to a GEV formulation, thereby providing a way of estimating its parameters that uses a larger amount of observational information.

While the methodologies and distributions described above form the core of traditional EVT, and have been utilized in various fields, there are significant challenges and assumptions underlying these approaches that may limit their applicability.

Extreme value theory, despite its conceptual appeal in providing justification for using the GEV distribution and the POT approach, comes with restrictive assumptions. These include the need for large samples from independent and identically distributed data to enable the AMS or POT to asymptotically converge to the GEV and GPD distributions (Fisher & Tippett, 1928). The convergence assumptions, though common, are often not verifiable in practice, as the number of independent rainfall events in a year is far from

infinite (Koutsoyiannis, 2004), and long data records are required, particularly when considering rainfall extremes at sub-daily durations (Libertino et al., 2018). Additionally, the assumptions of the POT approach present limitations, holding for a “large enough” threshold and under similar asymptotic assumptions to the GEV derivation (Pickands, 1975). This complicates the selection of a suitable threshold for the POT approach and reveals that traditional EVT can only use a small fraction of the observations, resulting in a waste of information. These challenges question the overall effectiveness and efficiency of traditional EVT approach, hampering the proper analysis and utilization of extreme value data.

2.2.2. The Metastatistical Extreme Values Framework

To address effectiveness concerns about traditional EVT approaches, Marani and Ignaccolo (2015) proposed the Metastatistical Extreme Value Distribution (MEVD) framework, an innovative approach that relaxes some of the assumptions of extreme value theory.

Unlike traditional extreme value theory, which relies on one or a few large values per observation year, the MEVD method exploits the full data record, regarding both the distributions that describe ordinary values ($F(x;\vec{\theta})$) and the number of occurrences in each year (n) as random variables (Marani & Ignaccolo, 2015). In the MEVD, ordinary events are assumed to be independent and the probability for a yearly maximum being smaller or equal to a particular value (x) is defined as:

$$H(x) = \sum_{n=1}^{\infty} \int_{\Omega_{\vec{\theta}}} \left[F\left(x;\vec{\theta}\right)\right]^n g\left(n;\vec{\theta}\right) d\vec{\theta}\ , \qquad (6)$$

In this expression, $g\left(n;\vec{\theta}\right)$ represents the joint probability distribution which is discrete with respect to the number of events in a year, n, and continuous in relation to the parameter vector $\vec{\theta}$; $\Omega_{\vec{\theta}}$ signifies the entire population of the parameters values. This approach recognizes that extreme instances are samples from 'ordinary events,' independent

realizations of the same stochastic process. Since ordinary events are more numerous than extremes, the MEVD framework can utilize the majority of observational data.

The cumulative distribution for yearly maxima in the MEVD framework is derived from the probability distributions of ordinary values. The empirical extreme value distribution is calculated as a sample average of the distributions of the ordinary events that occur in each year, and these are sampled a varying number of times annually. Following Marani and Ignaccolo (2015), the cumulative distribution function of ordinary events (block maxima) is represented as follows:

$$\zeta_{MEV}(x) = \frac{1}{M}\sum_{j=1}^{M}\left[F\left(x;\vec{\theta}_j\right)\right]^{n_j}, \qquad (7)$$

Where x is the precipitation intensity, M is the number of sampled blocks (years) on record, $F\left(x;\vec{\theta}_j\right)$ is the distribution of the ordinary events for each block j fitted to n_j ordinary events of the jth block. A schematic visualization of the application of the MEVD is presented in Figure 2.1 from Zorzetto et al. (2016).

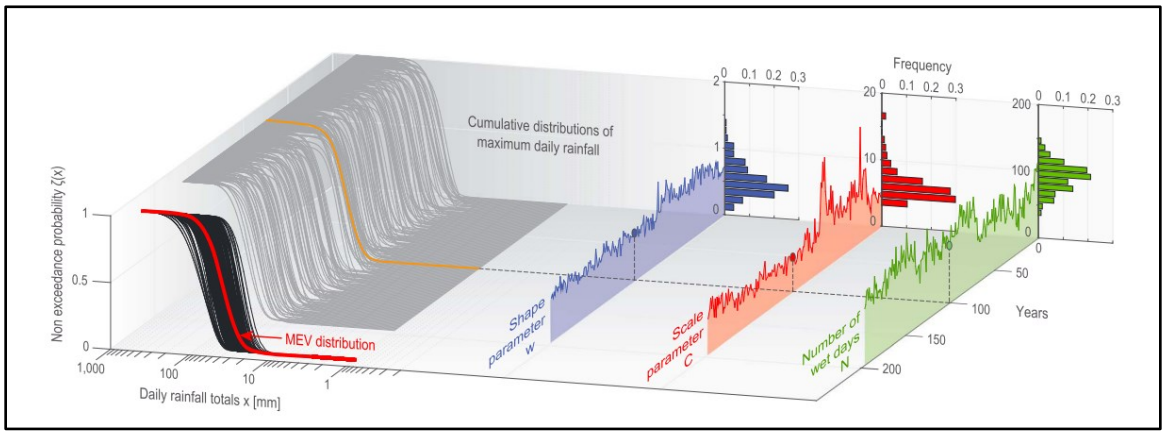

Figure 2-1: This illustration presents the application methodology of MEV to a sequence of daily rainfall data. Each year, the Weibull distribution's scale (C) and shape (w) parameters are calculated by fitting them to ordinary values. The event count 'n' represents the number of rainy days within a specific year. Using this methodology, we can calculate the annual cumulative distribution of maximum daily rainfall, as shown in the sum expression in Equation (4). The MEVD is then determined as the average cumulative distribution of annual peak values over all the years, which is depicted here by a red line. Source: (Zorzetto et al., 2016)

The core premise of the MEVD method is the identification of an appropriate statistical model for ordinary events. Daily and hourly rainfall within the MEVD approach are usually represented using a Weibull distribution (Marani & Ignaccolo, 2015; Marra et al., 2018; Miniussi & Marani, 2020; Zorzetto et al., 2016). Once an appropriate model is found, it can be used to predict the distribution of yearly maxima and the probability of rare, possibly unprecedented, extremes. Recent work on rainfall statistics indeed supports this model choice (e.g., Marani & Ignaccolo, 2015; Marra et al., 2018; Miniussi & Marani, 2020; Zorzetto et al., 2016). Hence, the MEVD-Weibull can be presented as:

$$\zeta_{MEV}(x) = \frac{1}{M}\sum_{j=1}^{M}\left[1 - exp\left(-\left(\frac{x}{C_j}\right)\right)^{w_j}\right]^{n_j}, \qquad (8)$$

Where, C_j and w_j are the scale and shape parameters of the Weibull distribution for year j.

Several research efforts have highlighted the benefits of employing the MEVD method instead of the conventional EVT in analyzing rainfall data. Tested on daily rainfall records, the MEVD method has demonstrated superiority over traditional extreme value theory, especially when estimating return periods longer than the data record length, thereby diminishing the limitations of extreme value analysis from short data records (Zorzetto et al., 2016). Expanding this approach to sub-daily rainfall frequency analysis, Marra et al. (2018) found that although MEV may underestimate the 100-year return period quantiles of hourly rainfall with 5–20 years of actual data, it demonstrates diminished uncertainty and is less sensitive to errors (<30% uncertainty for 5-year records). These findings strongly support the use of MEVD for rainfall frequency analyses and showcase its significantly reduced uncertainty when dealing with short records in estimating rare quantiles (Marra et al., 2018; Miniussi & Marani, 2020; Zorzetto et al., 2016; Zorzetto & Marani, 2020).

In conclusion, the MEVD represents an improvement over traditional approaches, overcoming the problem of data wastage in the estimation of extremes and offering a way to tackle non-stationary processes. By embracing the concept of ordinary events and leveraging the majority of available data, the MEVD method opens new avenues for more

accurate and comprehensive extreme value analysis. Practically, the following steps will be implemented in this thesis for the application of MEV:

a) For each year of each rain gage and the corresponding CPM datasets the ordinary events are identified and separated.
b) A Weibull distribution is fitted to each yearly record of ordinary events. The parameters of the Weibull distribution are estimated using the Probability Weighted Moments (PWM) method. This approach is analytically identical to the L-moments method and is more reliable for small sample sizes compared to the Maximum Likelihood method (Hosking, 1990).
c) Then implementing Eq. (5) the cumulative distribution function of MEV is calculated.
d) The desired quantiles are calculated numerically by inverting Eq. (5).

2.2.2.1. Selection of Ordinary Events

Ordinary events represent independent realizations of specific processes, in our case, precipitation intensities observed over various durations. The identification and selection of these ordinary events are crucial for ensuring a consistent and accurate analysis of precipitation patterns.

The definition of ordinary events in this study is based on the storm-centric approach proposed by Marra et al. (2020). In this method, storms are perceived as independent meteorological objects, and ordinary events of varying durations are extracted directly from these storms. Specifically, storms are described as consecutive wet time intervals, separated by dry hiatuses. The duration of these dry intervals is determined based on the specific climatology of the region under consideration (Marra et al., 2020).

Here, a wet period is defined by a 1-h time interval that reports at least 0.2 mm (based on recording capacity of rain gauges) of precipitation. In contrast, dry hiatuses, which delineate different storms, last for 24 hours (Dallan et al., 2022). This criteria aids in ensuring the accuracy of the model's application while minimizing data loss.

Once the storms are separated, ordinary events are identified using moving windows that span the duration of interest. Within each storm, the maximum intensities observed define the ordinary events.

2.2.3. Derivation of DDF curves

By adhering to the procedures outlined in section 2.2.2, we can determine the desired quantiles for various return periods, such as 2, 10, 25, 50, 100, and 200 years, utilizing the MEVD's cumulative distribution function for rainfall of different durations of 1 h, 3 h, 6 h, 12 h, and 24 h. By plotting these quantiles against their durations for each return period and fitting the Montana type curve, we can generate the depth-duration-frequency curves.

The formula for the Montana DDF curves is:

$$h = aD^b \qquad (9)$$

In this equation, 'h' represents rainfall depth (in mm). 'a' is the Montana curve's coefficient, 'b' is its exponent, ranging between 0 and 1, and 'D' indicates the duration under consideration.

2.3. Study Area and Data

For this thesis a benchmark of continuous, quality-controlled, rainfall data is available from the Agenzia Regionale per la Prevenzione e Protezione Ambientale del Veneto (ARPAV dataset), which contains rain gauge stations with a temporal resolution of 5 minutes and data quantization of 0.2 mm. A total of 29 stations (Fig. 2-2) were selected with a minimum length of records of 17 years and a maximum length of 37 years. These rain gauges cover elevation in the range of -3 to 2090 m a.s.l. The data for all the stations were aggregated to 1, 3, 6, 12 and 24 h durations.

Convection-Permitting Model (CPM) simulation carried out by Zurich's Swiss Federal Institute of Technology (ETH Zurich), in collaboration with the Consortium for Small-Scale Modeling (COSMO-crCLIM) is utilized in this thesis. This particular simulation pertains to a broader geographical region encompassing the Alps, a scope defined under the Flagship Pilot Study on Convective Phenomena over Europe and the Mediterranean (FPS-Convection) as part of the Coordinated Regional Climate Downscaling Experiment (CORDEX) initiative (Coppola et al., 2020). These CPMs are available in decadal periods of 1996 – 2005 for historical period and 2040 – 2049 and 2090 – 2099 for near and far future.

In this vein, the transition to high-resolution CPMs is especially relevant for Northern Italy. In the context of this region, shifting from conventional Regional Climate Models (RCMs) to high-resolution CPMs could potentially address the gap in accurately predicting sub-daily extreme rainfall events (Maraun et al., 2010). This area, with its varied topography and diverse climate, is subject to extreme rainfall hazard, with large impacts both on urban and rural landscapes.

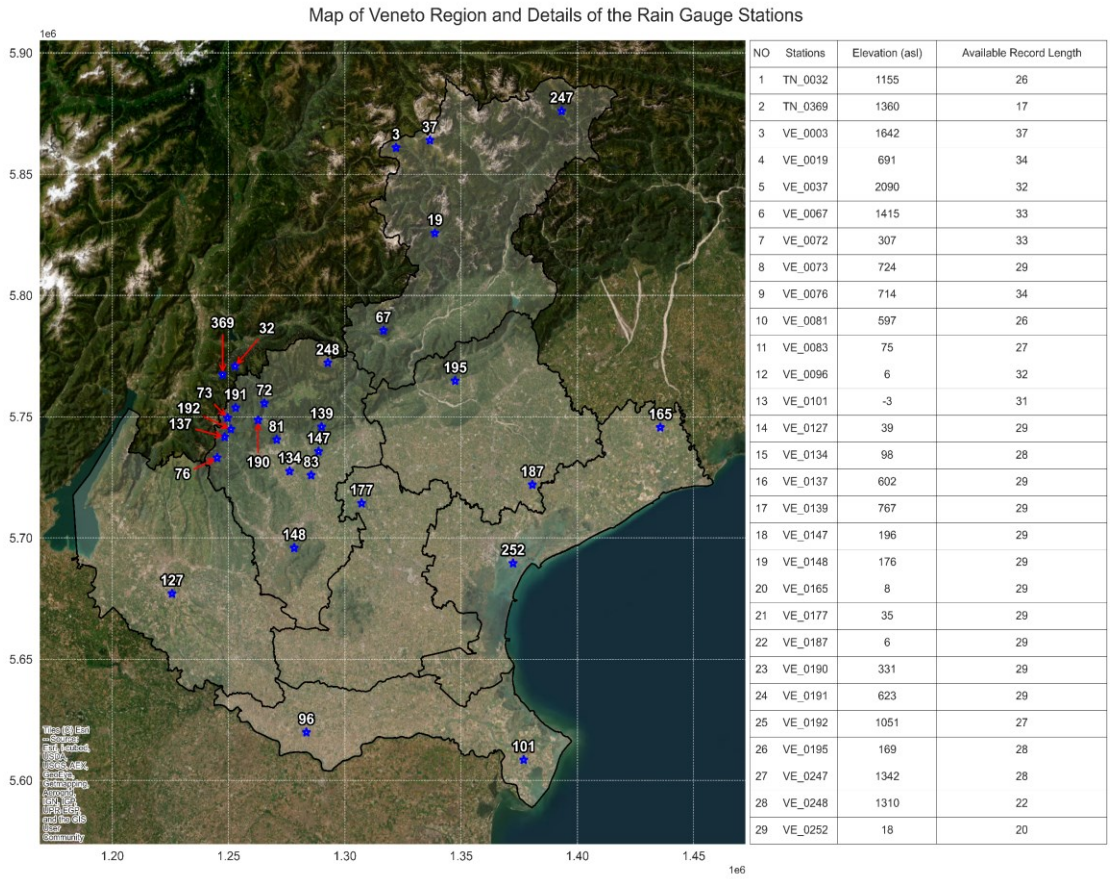

NO	Stations	Elevation (asl)	Available Record Length
1	TN_0032	1155	26
2	TN_0369	1360	17
3	VE_0003	1642	37
4	VE_0019	691	34
5	VE_0037	2090	32
6	VE_0067	1415	33
7	VE_0072	307	33
8	VE_0073	724	29
9	VE_0076	714	34
10	VE_0081	597	26
11	VE_0083	75	27
12	VE_0096	6	32
13	VE_0101	-3	31
14	VE_0127	39	29
15	VE_0134	98	28
16	VE_0137	602	29
17	VE_0139	767	29
18	VE_0147	196	29
19	VE_0148	176	29
20	VE_0165	8	29
21	VE_0177	35	29
22	VE_0187	6	29
23	VE_0190	331	29
24	VE_0191	623	29
25	VE_0192	1051	27
26	VE_0195	169	28
27	VE_0247	1342	28
28	VE_0248	1310	22
29	VE_0252	18	20

Figure 2-2: Map of Veneto Region and the details and locations of the rain gauge stations.

Chapter 3

3. Results

3.1. Statistics of the Rain Gauge Stations

In this study, 29 rain gauge stations were analyzed, as illustrated in Figure 2-2. The average rain intensity for these stations is presented in (Figure 3-1). Furthermore, Figure 3-2 showcases the mean annual maximum rain intensity for these stations.

To better understand these rain events, the Weibull distribution was applied to the data from ordinary events. Utilizing the criteria specified for selecting ordinary events in section 2.2.2.1, Figure 3-3 represents the map of values of parameter 'N' for the ordinary events of the stations. Figure 3-4 and Figure 3-5, illustrate the scale and shape parameters of the Weibull distribution for the ordinary events of the gauged data.

Building on a 10-year data record, 50-year return levels were estimated in alignment with the historical reference period used in the CPMs from 1996 to 2005. Map of 50-year return levels are presented in Figure 3-6.

Figure 3-7, 8, and 9 depict the parameters values of ordinary events distribution from the observational data across various durations. To differentiate among the 29 stations, 20 unique color iterations were employed in these figures. For clarity, the remaining nine stations, which share similar colors, are represented with a solid line to ensure easy distinction.

Figure 3-7 highlights the values of the 'N' parameter for ordinary events. Given that the same criteria were applied consistently across all durations for the selection of ordinary

events, the 'N' values remain consistent throughout the various durations for each station. Meanwhile, Figure 3-8 displays the scale parameter values against duration for each station's ordinary events. Lastly, Figure 3-9 showcases the shape parameter values of the ordinary events set against duration.

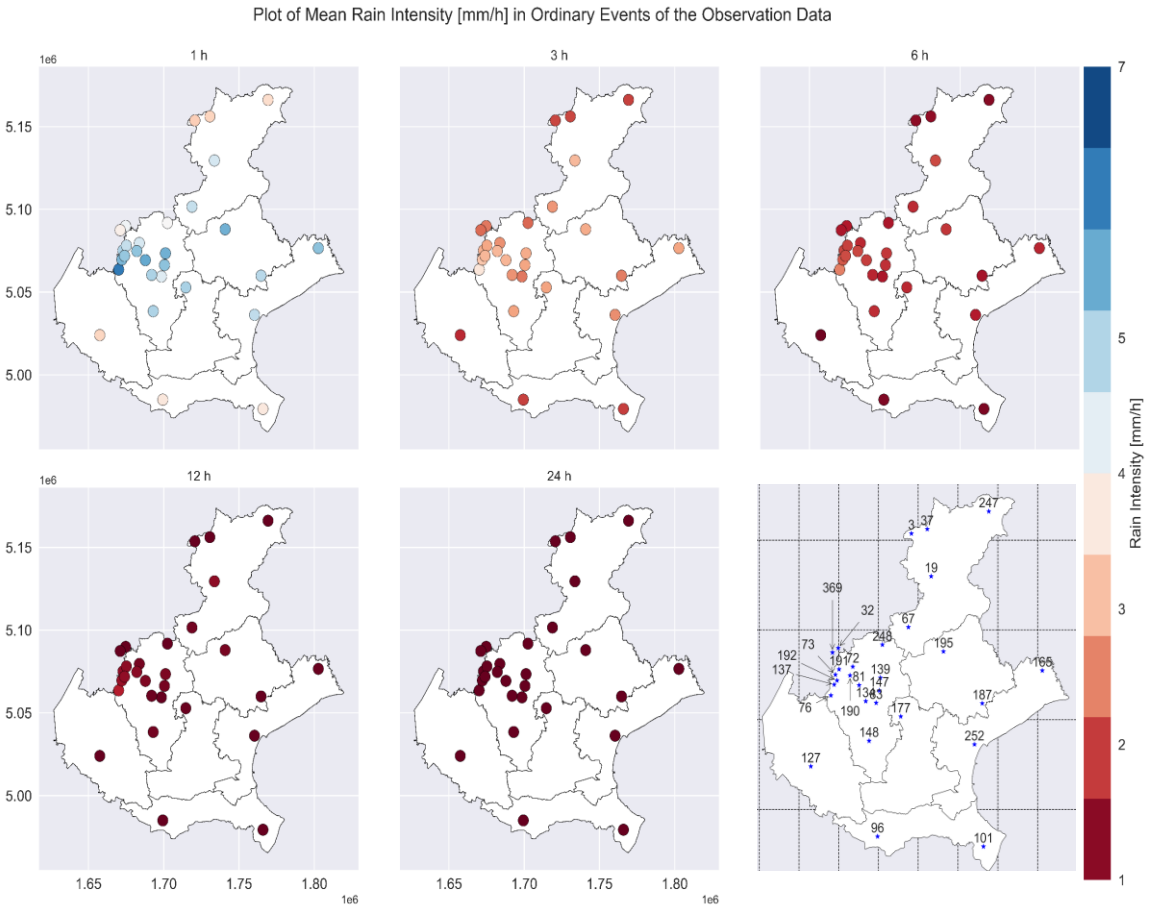

Figure 3-1: Map of mean rain intensity in ordinary events of the observation data for five different rainfall durations. The sixth map on the bottom right corner of the figure displays the locations of each of the rain gauge stations.

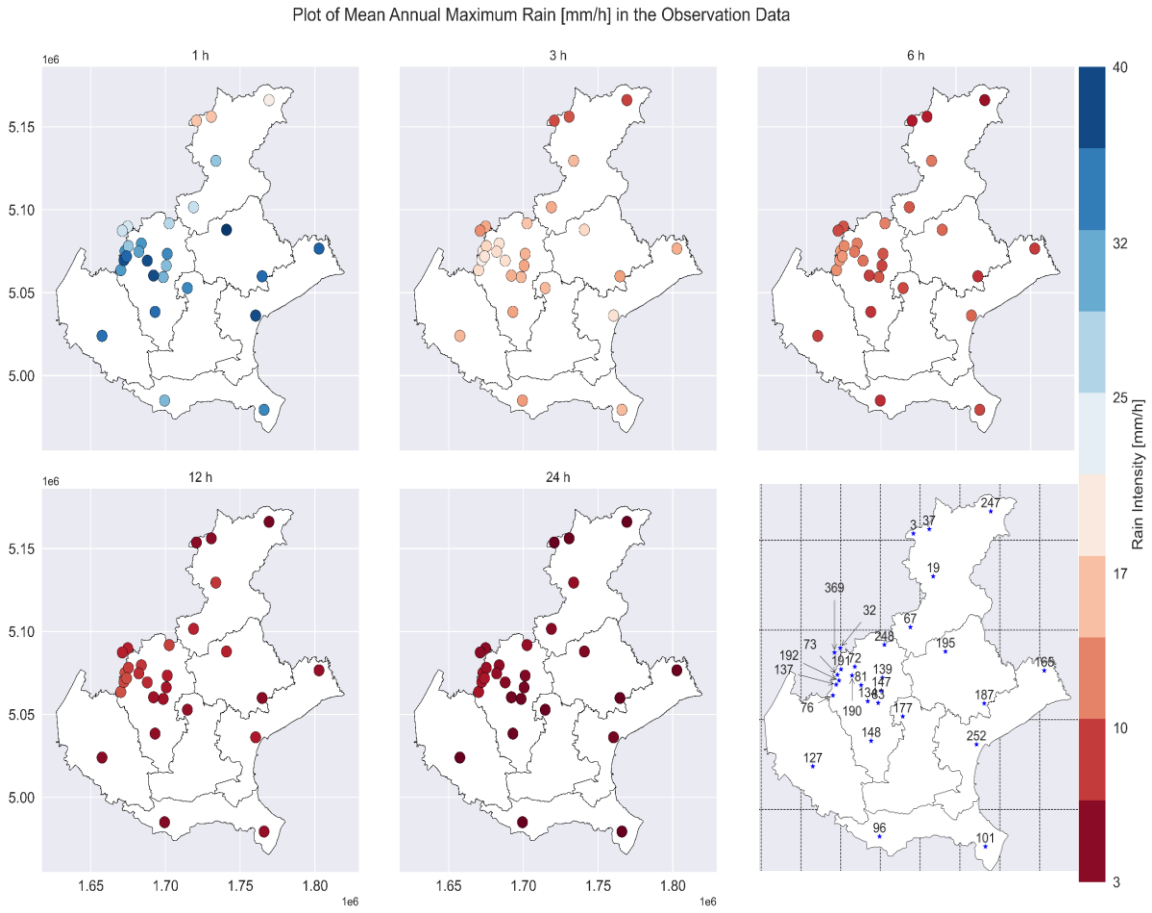

Figure 3-2: Map of mean annual maximum rain intensity in the observation data for five different rainfall durations. The sixth map on the bottom right corner of the figure displays the locations of each of the rain gauge stations.

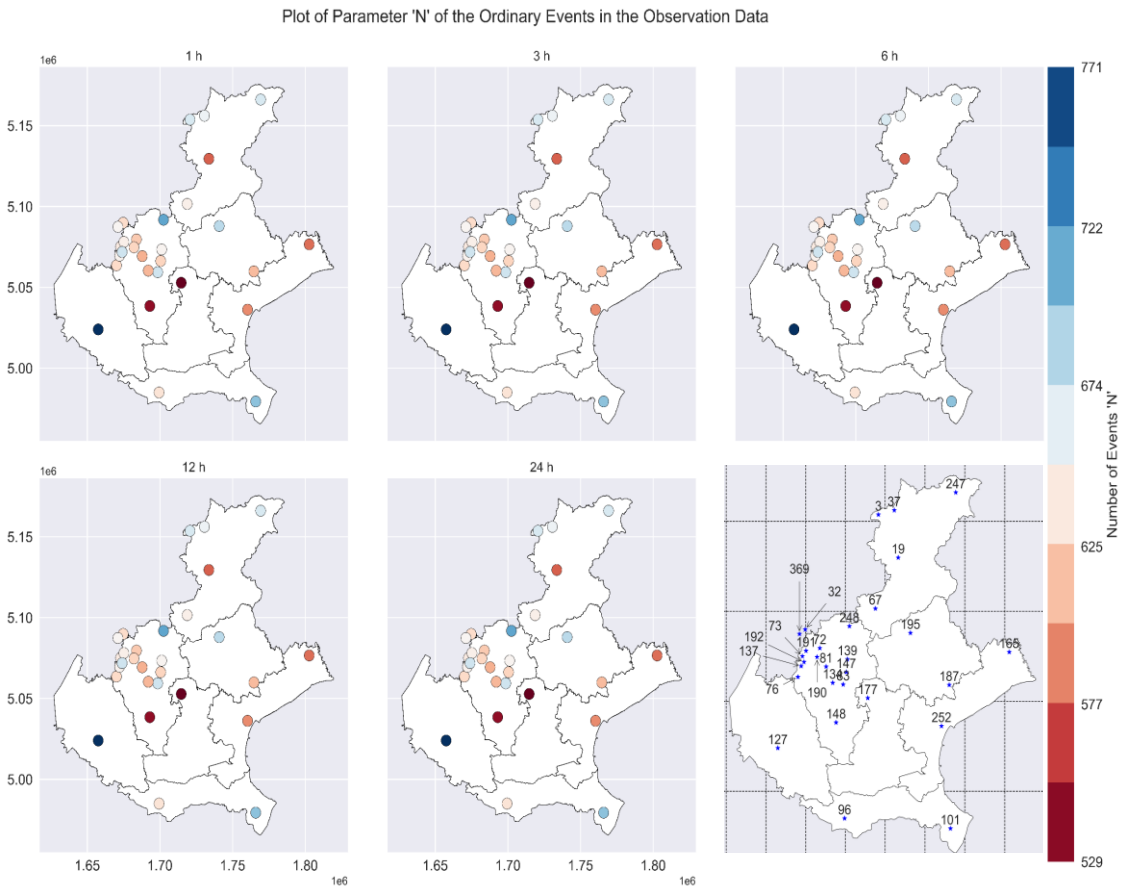

Figure 3-3: Map of values of parameter 'N' of the ordinary events in the observation data for five different rainfall durations. The sixth map on the bottom right corner of the figure displays the locations of each of the rain gauge stations.

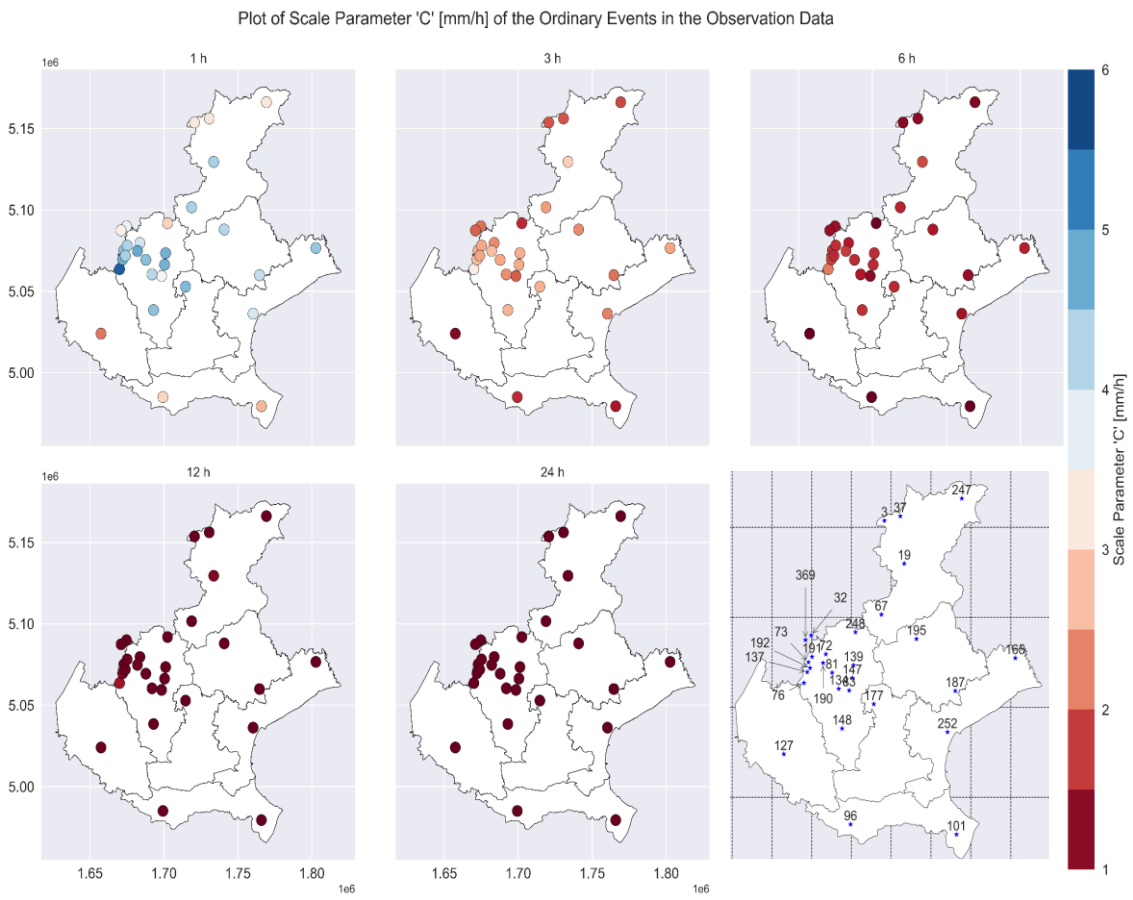

Figure 3-4: Map of values of scale parameter of the ordinary events in observation data for five different rainfall durations. The sixth map on the bottom right corner of the figure displays the locations of each of the rain gauge stations.

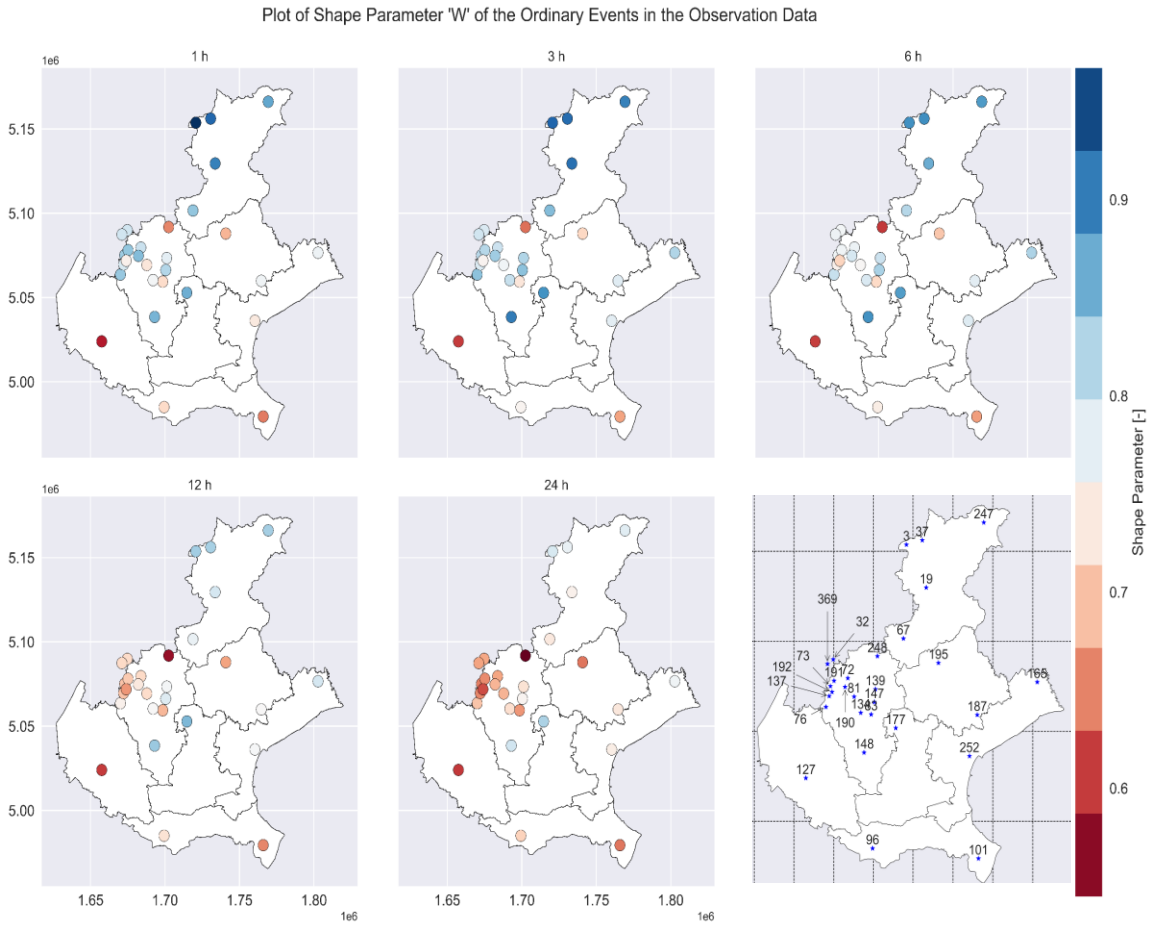

Figure 3-5: Map of values of shape parameter of the ordinary events in observation data for five different rainfall durations. The sixth map on the bottom right corner of the figure displays the locations of each of the rain gauge stations.

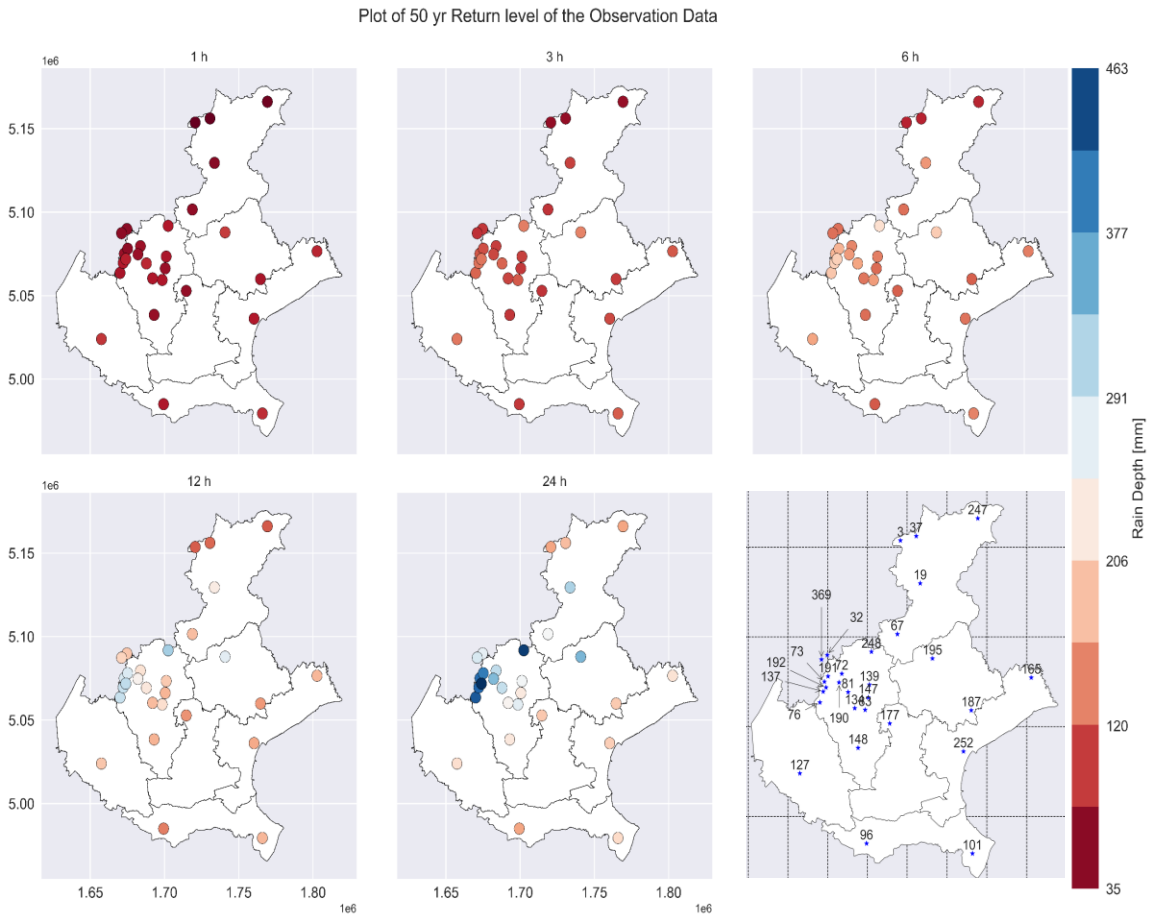

Figure 3-6: Map of 50-yr return levels of the observation data for five different rainfall durations. The sixth map on the bottom right corner of the figure displays the locations of each of the rain gauge stations.

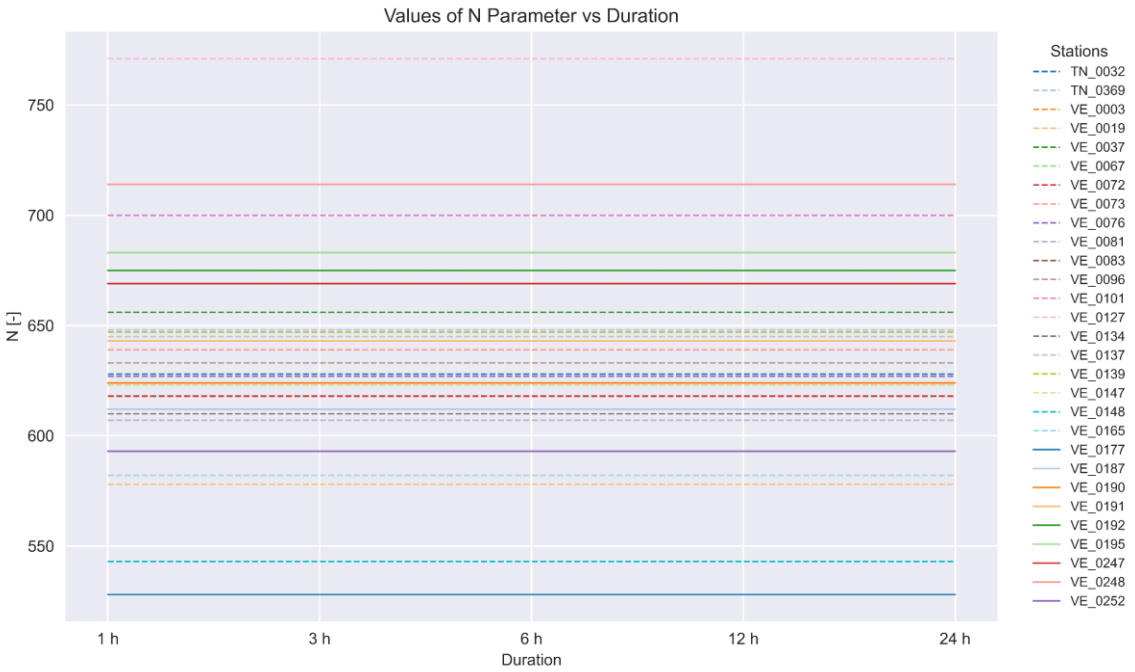

Figure 3-7: Plot of 'N' parameter versus duration for all rain gauge stations.

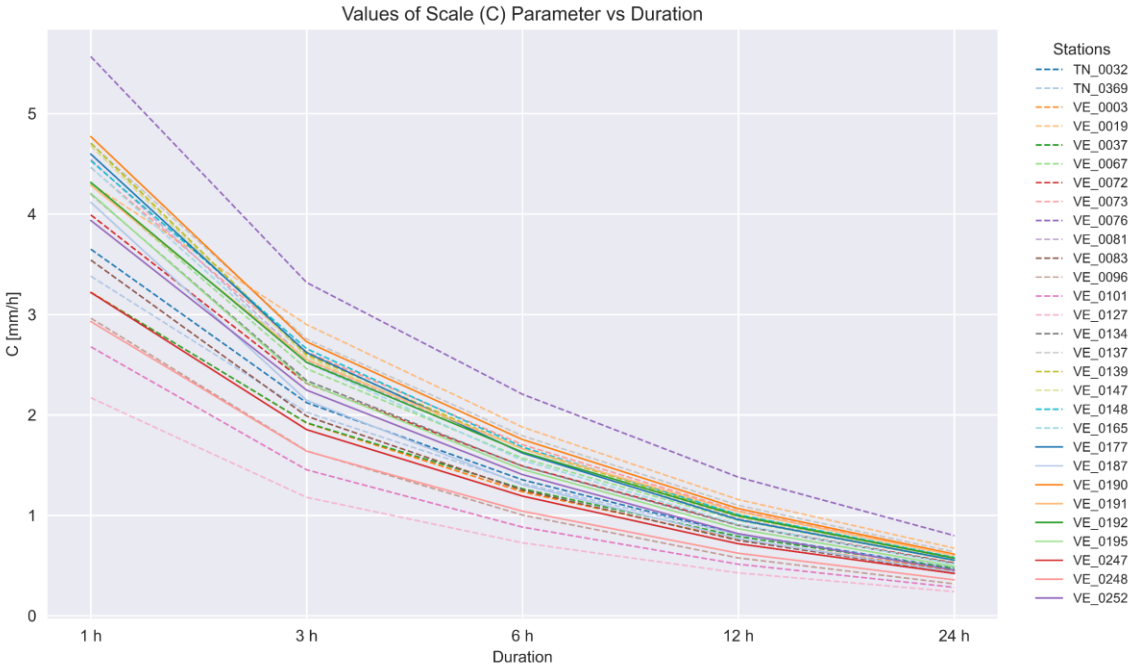

Figure 3-8: Plot of scale parameter versus duration for all the rain gauge stations.

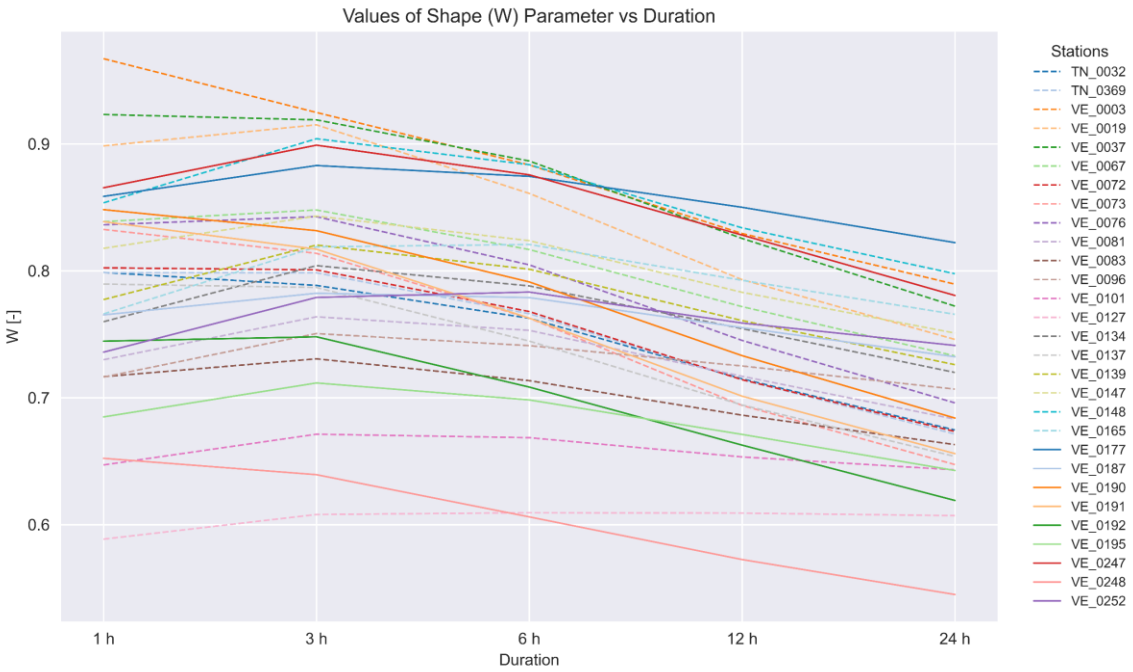

Figure 3-9: Plot of shape parameter versus duration for all the rain gauge stations.

3.2. Comparison of Observation Data with CPM Historical Run (1996 – 2005).

In this section, we will present the assessment of the biases of the CPM by comparing it to the statistics from the observation data presented in the previous section. The evaluation will present the ratio of CPM values to observational values for each aspect: mean rain intensity, mean annual maximum rain, and parameters of the ordinary events distribution.

Figure 3-10 displays the ratio of mean rain intensity values for ordinary events in both CPM and observations. Figure 3-11, on the other hand, visualizes these ratios across various durations for each station. A clear observation from the figures is the evident overestimation by the CPM. Furthermore, Figure 3-11, illustrates that this overestimation amplifies across the duration for all the stations.

Concerning the mean annual maximum rain intensity, Figure 3-12 and Figure 3-13 highlight the CPM's tendency to overestimate compared to the observational data for the

majority of the stations. While Figure 3-13 maps these ratios against durations and reveals an increasing trend in the ratio for most stations, however, certain stations display an unpredictable pattern across different durations.

When examining the parameters of the ordinary events distribution, the CPM overestimates all three parameters: ‘N’, ‘C’, and ‘W’. This overestimation is evident in Figure 3-14 and Figure 3-15, which depict the ratio of the number of events in the CPM compared to the observations for parameter ‘N’. Similarly, Figure 3-16 and Figure 3-17 display the ratio discrepancies in the scale parameters between the two datasets. Lastly, Figure 3-18 and Figure 3-19 highlight the overestimation in the shape parameters' ratios.

As for the 50-year return levels, Figure 3-20 and Figure 3-21 indicate that the CPM actually underestimates the observations for approximately half of the stations.

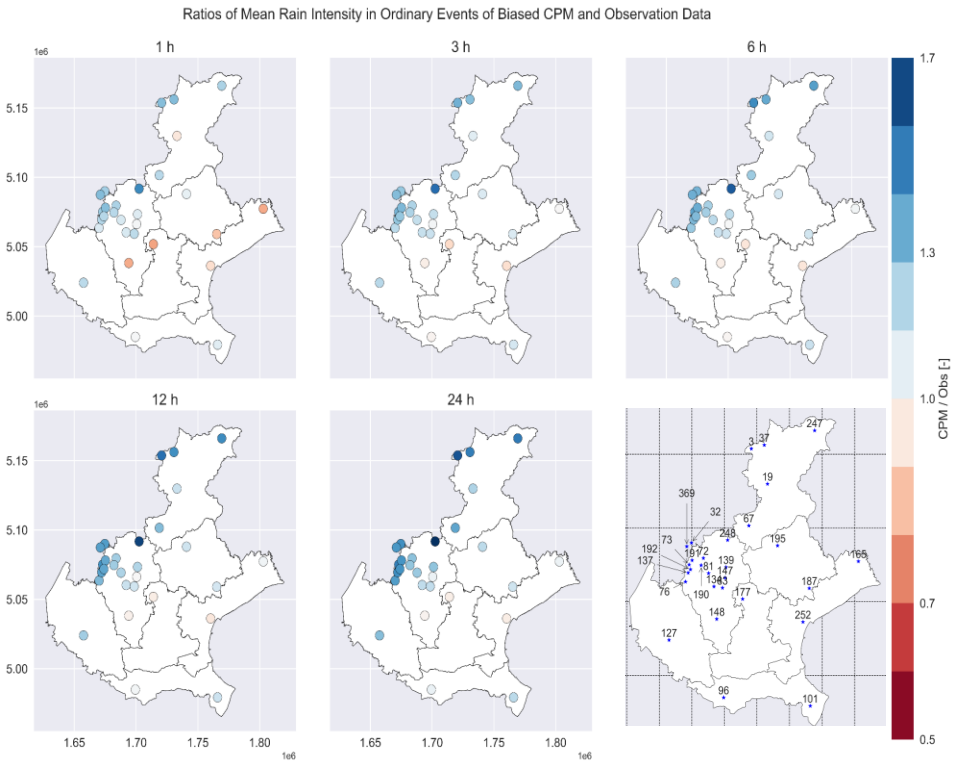

Figure 3-10: Map of ratios mean rain intensity for CPM and observation data.

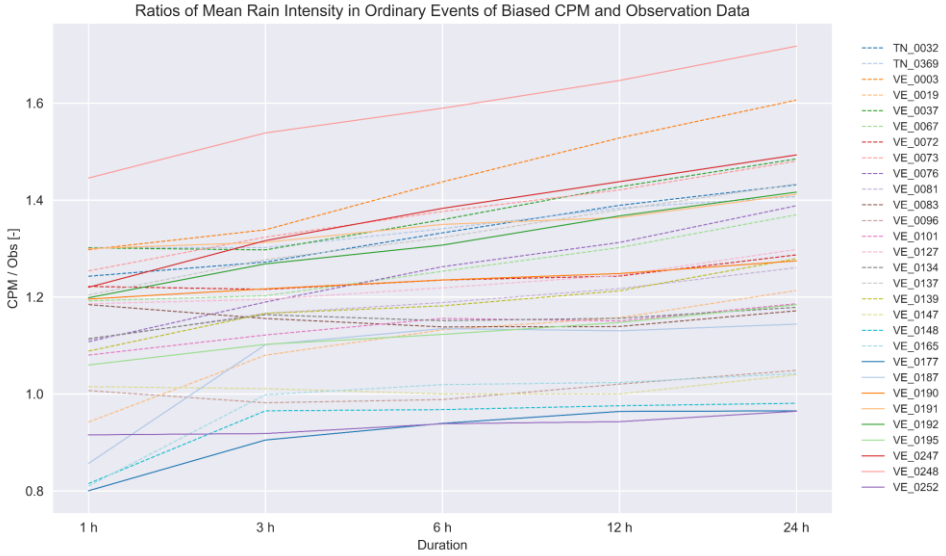

Figure 3-11: Ratios of mean rain intensity for CPM and observation data across all durations.

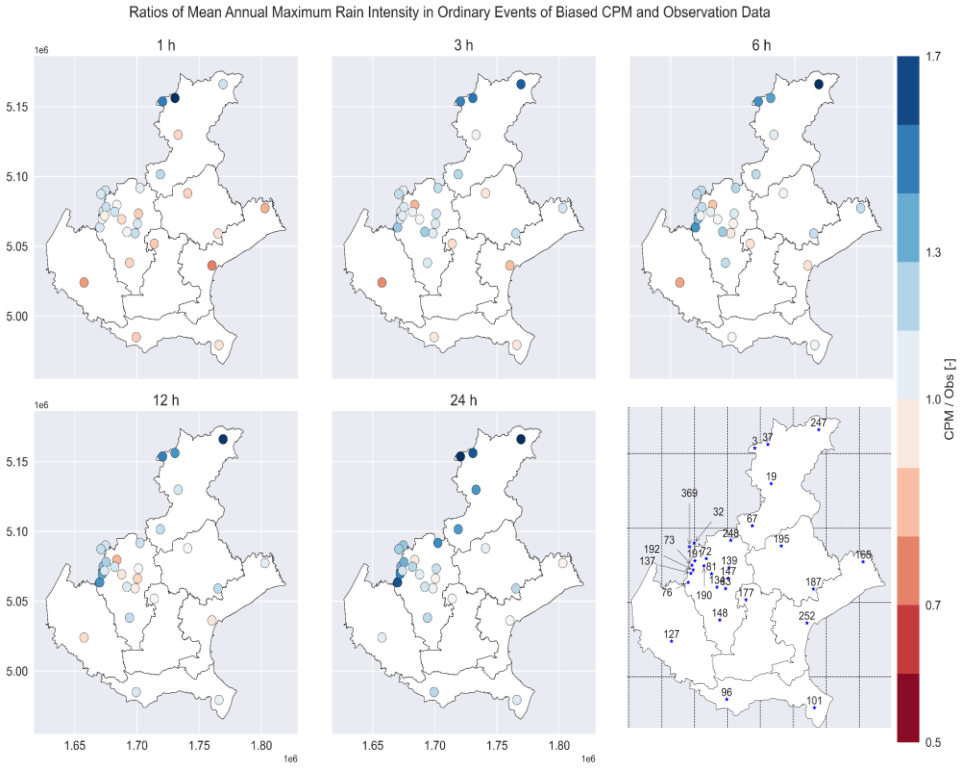

Figure 3-12: Map of ratios of mean annual maximum rain intensity for CPM and observation data.

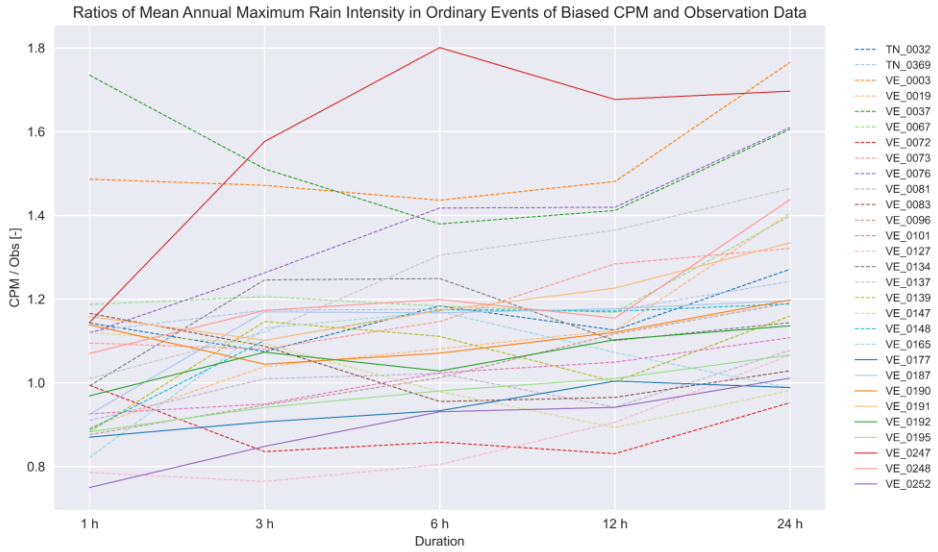

Figure 3-13: Ratios of mean annual maximum rain intensity for CPM and observation data across all durations.

Figure 3-14: Map of ratios of parameter 'N' for CPM and observation data.

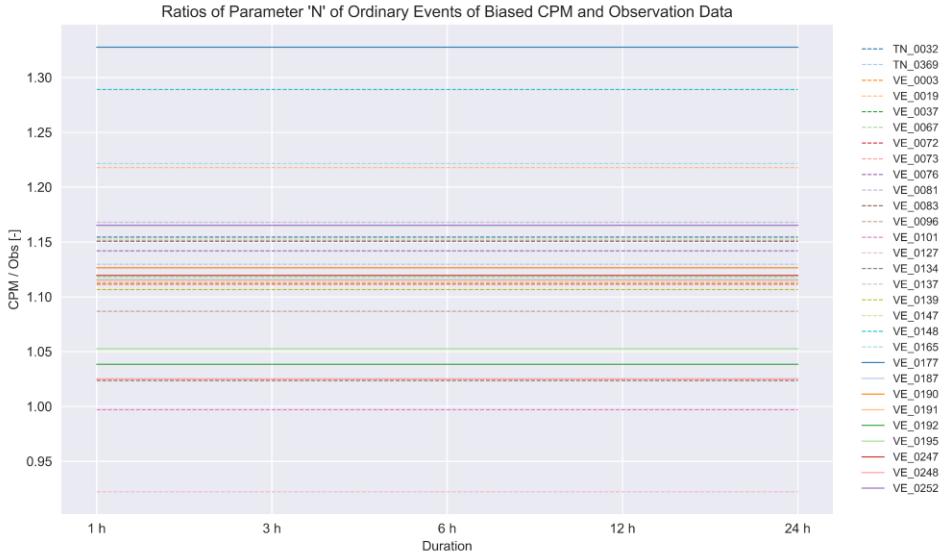

Figure 3-15: Ratios of parameter 'N' for CPM and observation data across all durations.

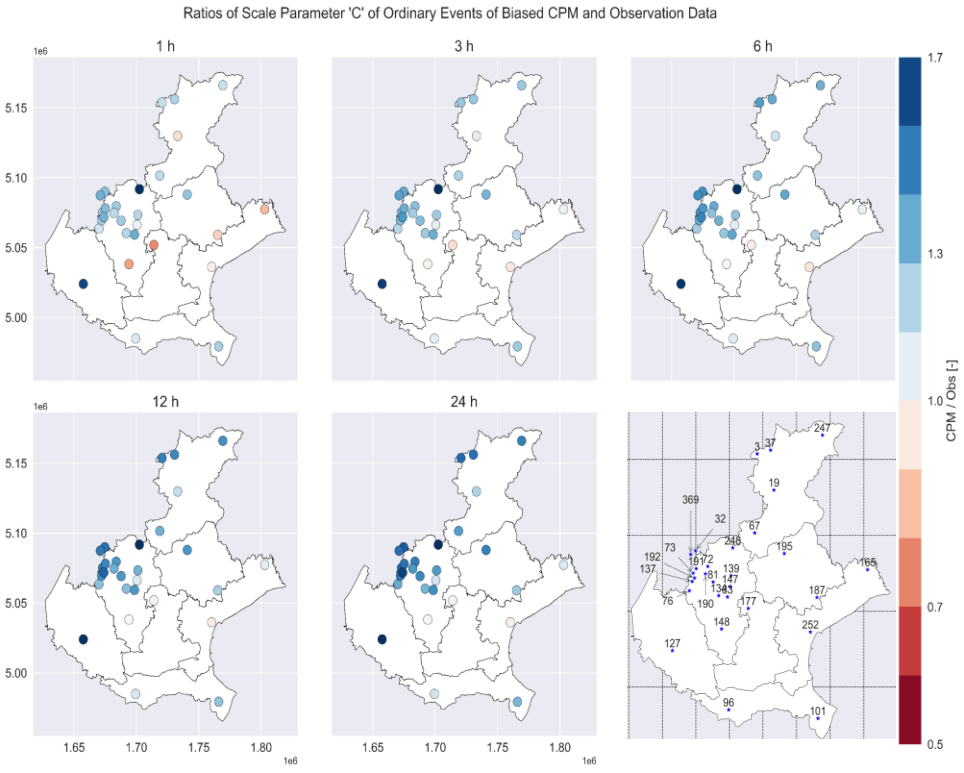

Figure 3-16: Map of ratios of scale parameter 'C' for CPM and observation data.

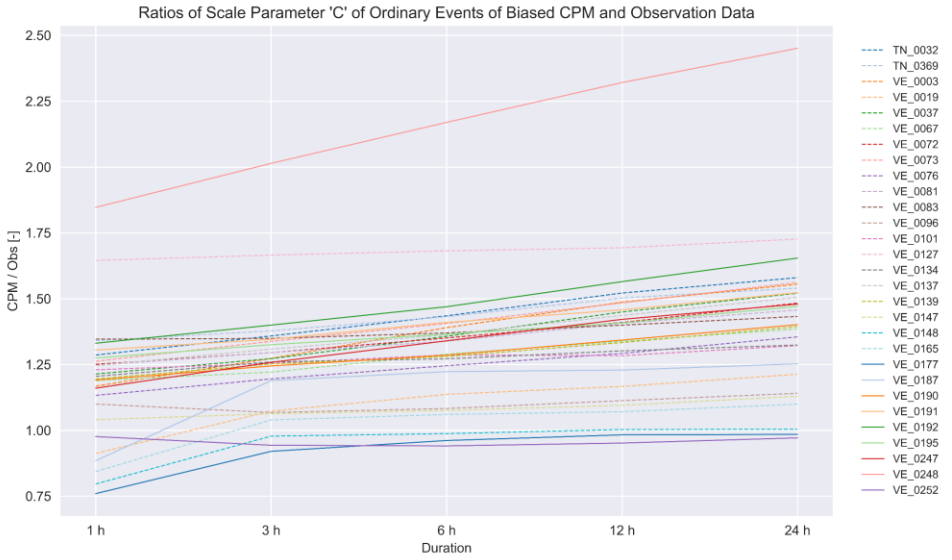

Figure 3-17: Ratios of scale parameter 'C' for CPM and observation data across all durations.

Figure 3-18: Map of ratios of shape parameter 'W' for CPM and observation data.

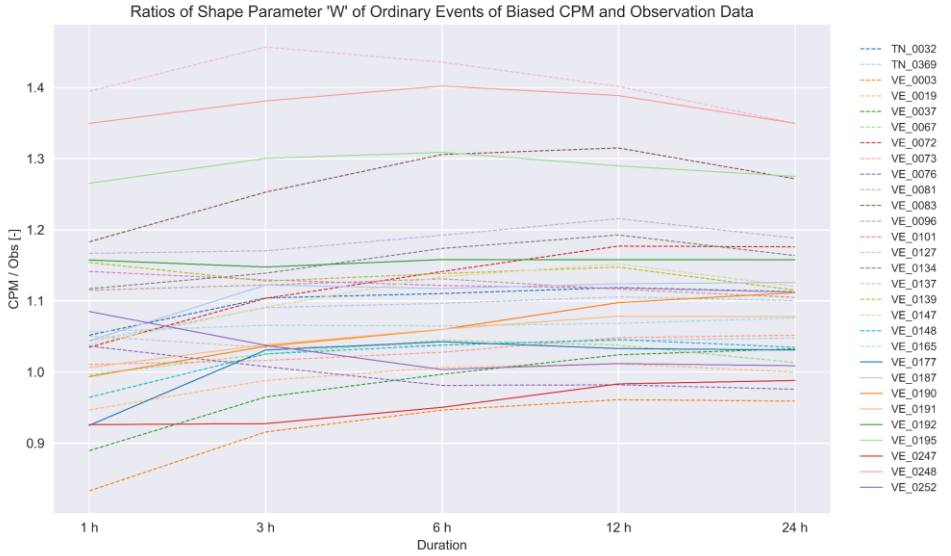

Figure 3-19: Ratios of shape parameter 'W' for CPM and observation data across all durations.

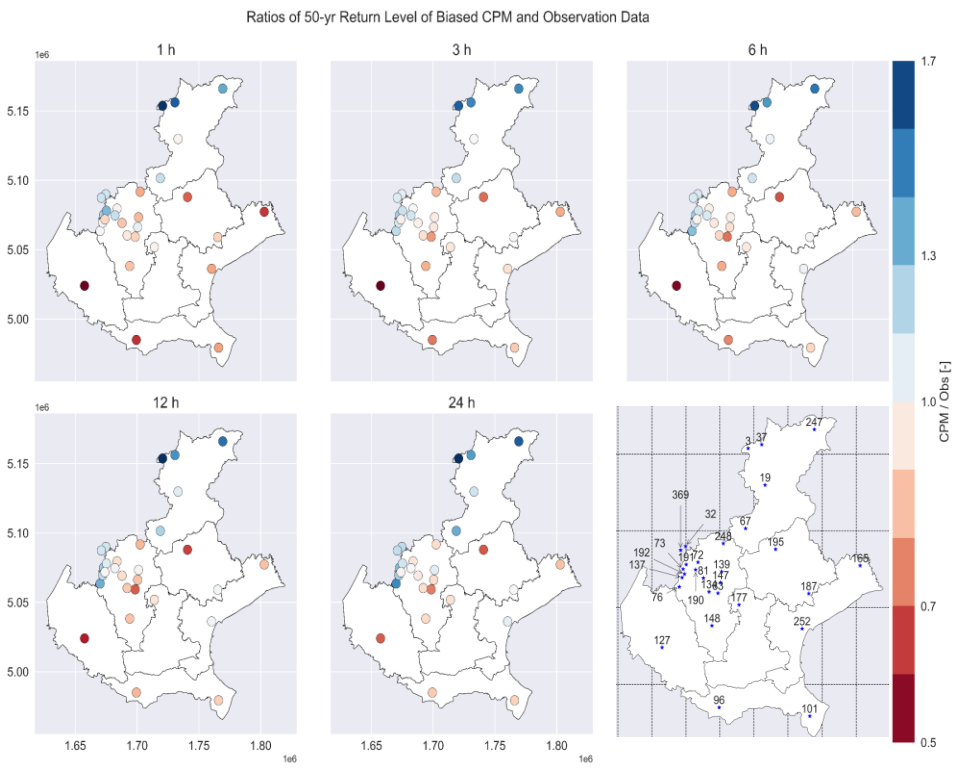

Figure 3-20: Map of ratios of 50-yr return levels of CPM and observation data.

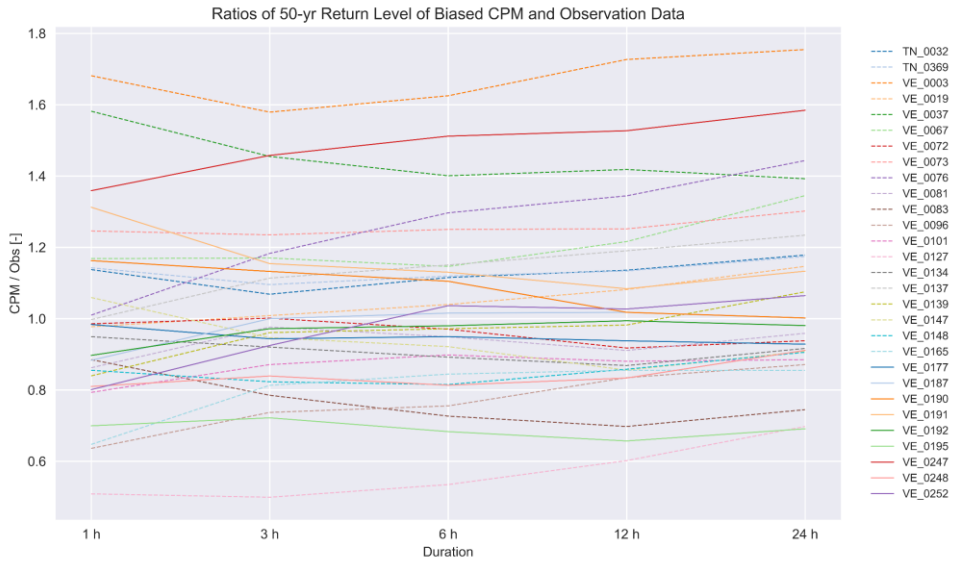

Figure 3-21: Ratios of 50-yr return levels of CPM and observation data across all durations.

3.3. Comparison of Observation Data with Corrected CPM Historical Run (1996 – 2005)

In this section, we will present the comparison between the bias-corrected CPM and the observed data. As outlined in section 2.1.3.1 (page 17), we employed the Quantile Mapping method for bias correction, which effectively aligned the CPM statistics with those of the observations.

Figure 3-22 illustrate the ratios of mean rain intensity considering corrected CPM to the observation data. The bias correction performance for the case of mean annual maximum rain in the CPM, is illustrated in Figure 3-23 and Figure 3-24.

In terms of the parameters for the ordinary events distribution, refer to Figure 3-25 for parameter ‘N’, Figure 3-26 for the scale parameter, and Figure 3-27 for the shape parameter.

Moreover, Figure 3-28 and Figure 3-29 examine the performance of bias correction for 50-year return levels for the CPM's and the observational data.

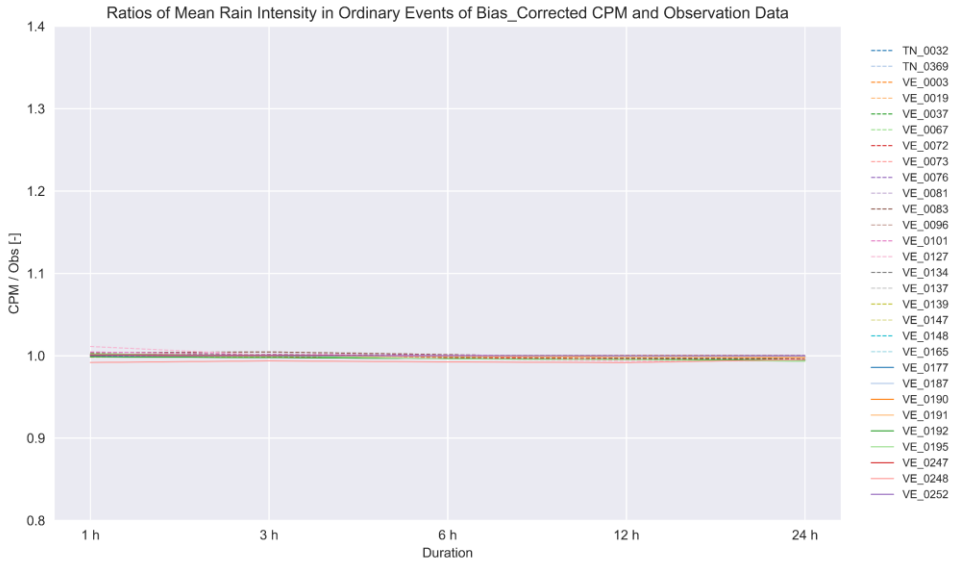

Figure 3-22: Ratios of mean rain intensity for Corrected_CPM and observation data across all durations.

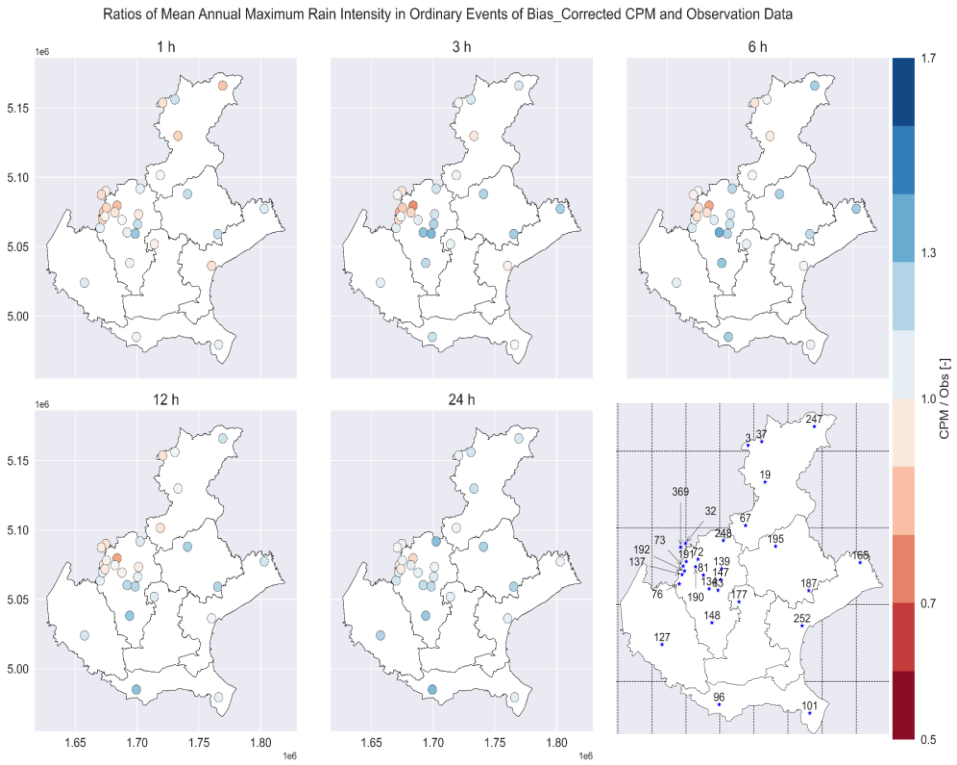

Figure 3-23: Map of ratios of mean annual maximum rain intensity for Corrected_CPM and observation data.

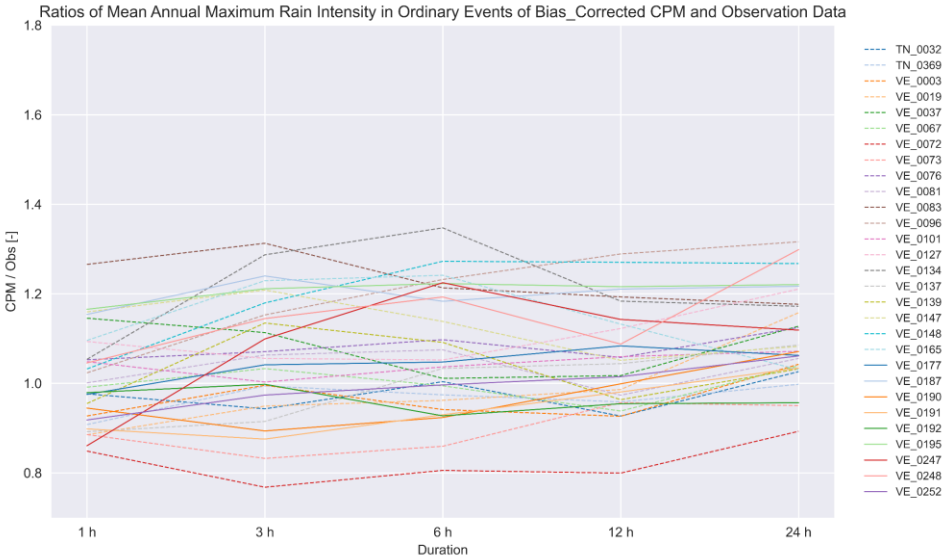

Figure 3-24: Ratios of mean annual maximum rain intensity for Corrected_CPM and observation data across all durations.

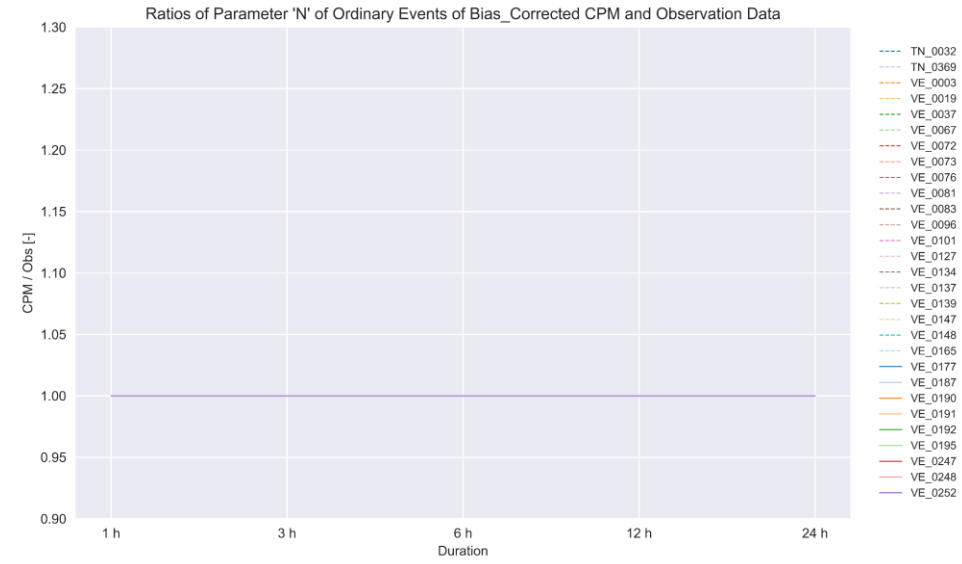

Figure 3-25: Ratios of parameter 'N' for Corrected_CPM and observation data across all durations.

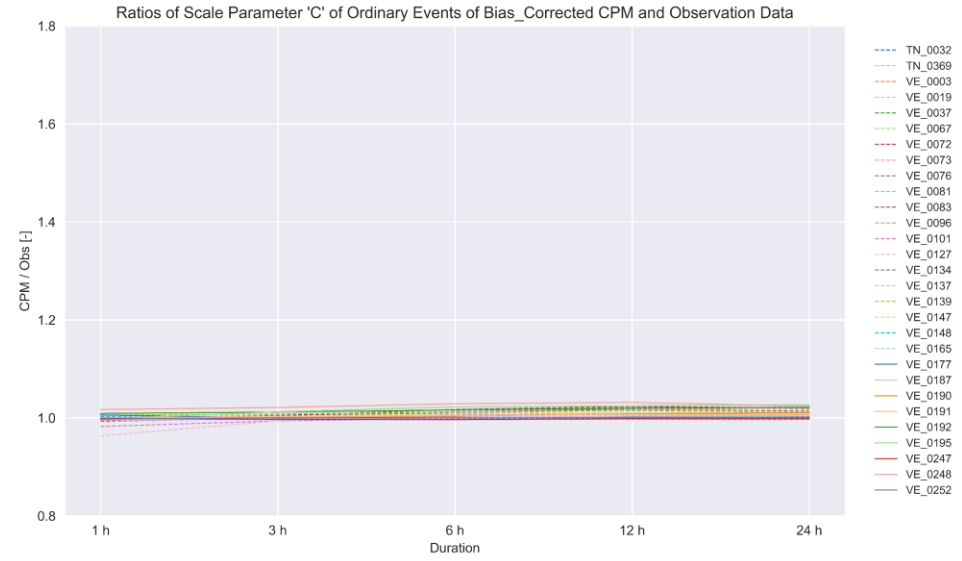

Figure 3-26: Ratios of scale parameter 'C' for Corrected_CPM and observation data across all durations.

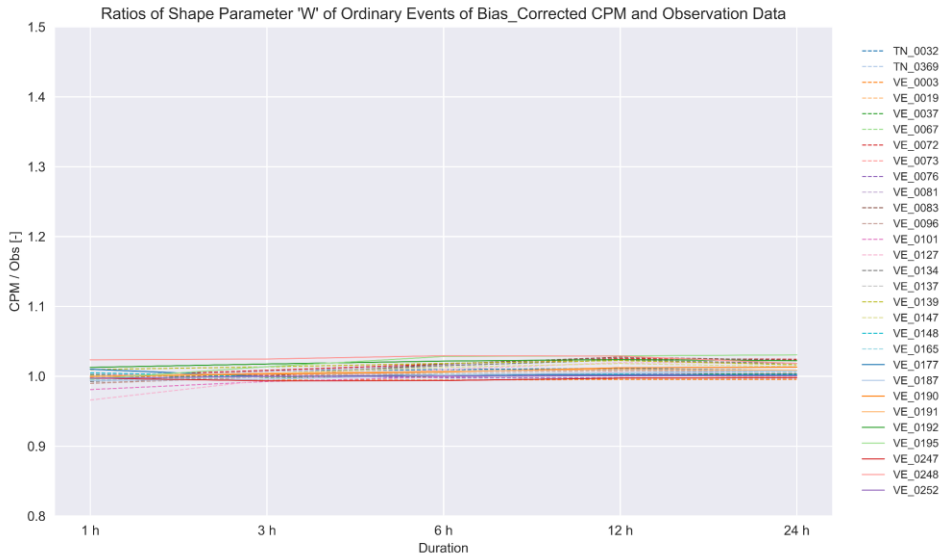

Figure 3-27: Ratios of shape parameter 'W' for Corrected_CPM and observation data across all durations.

Figure 3-28: Map of ratios of 50-yr return levels of Corrected_CPM and observation data.

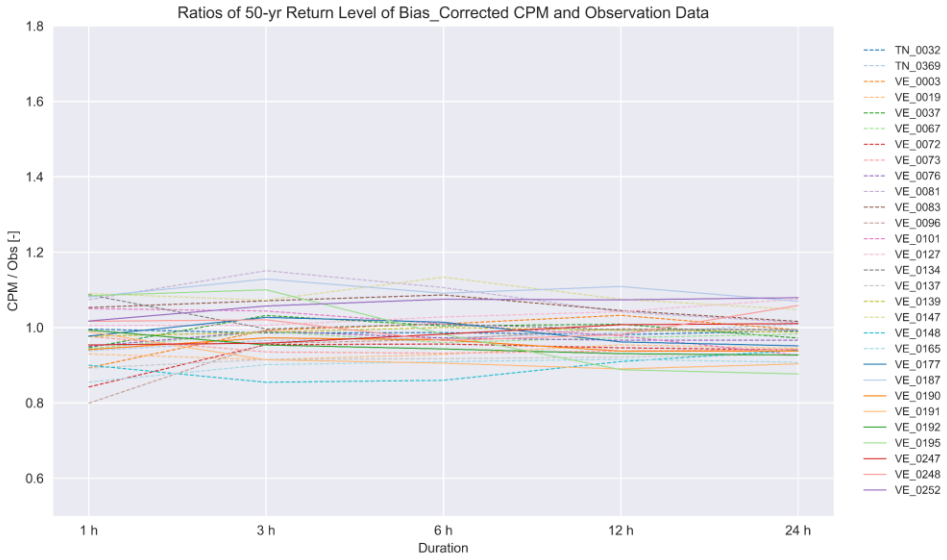

Figure 3-29: Ratios of 50-yr return levels of Corrected_CPM and observation data across all durations.

3.4. Evaluation of Parameters of Depth-Duration-Frequency Curves

In section 2.2.3, we discussed the analysis framed around the parameters of the depth-duration-frequency (DDF) curves as illustrated by equation 10. These parameters will be presented in this section which is organized into dedicated subsections for each dataset:

a) Observation data

b) Uncorrected CPM historical run (1996-2005)

c) Bias-corrected CPM historical run (1996-2005)

d) Uncorrected CPM near future run (2040-2049)

e) Bias-corrected CPM near future run (2040-2049)

f) Uncorrected CPM far future run (2090-2099)

g) Bias-corrected CPM far future run (2090-2099).

For each dataset, we display the values of parameters ‘a’ and ‘b’ of the DDF curves on maps across various return periods, culminating in comprehensive boxplots for all datasets.

Figure 3-30 and Figure 3-31 highlight these parameter values for observational data. The parameters for uncorrected and bias-corrected CPM historical run are depicted in Figure 3-32 through 39. Figure 3-36 to 43 showcase the coefficients and exponents of the DDF curve for the near-future CPM run, while Figure 3-40 to 47 illuminate these aspects for the far-future CPM run. The encompassing boxplots, contrasting the uncorrected and bias-corrected parameters across different return periods, are presented in Figure 3-44 to 51.

3.4.1. Observation data

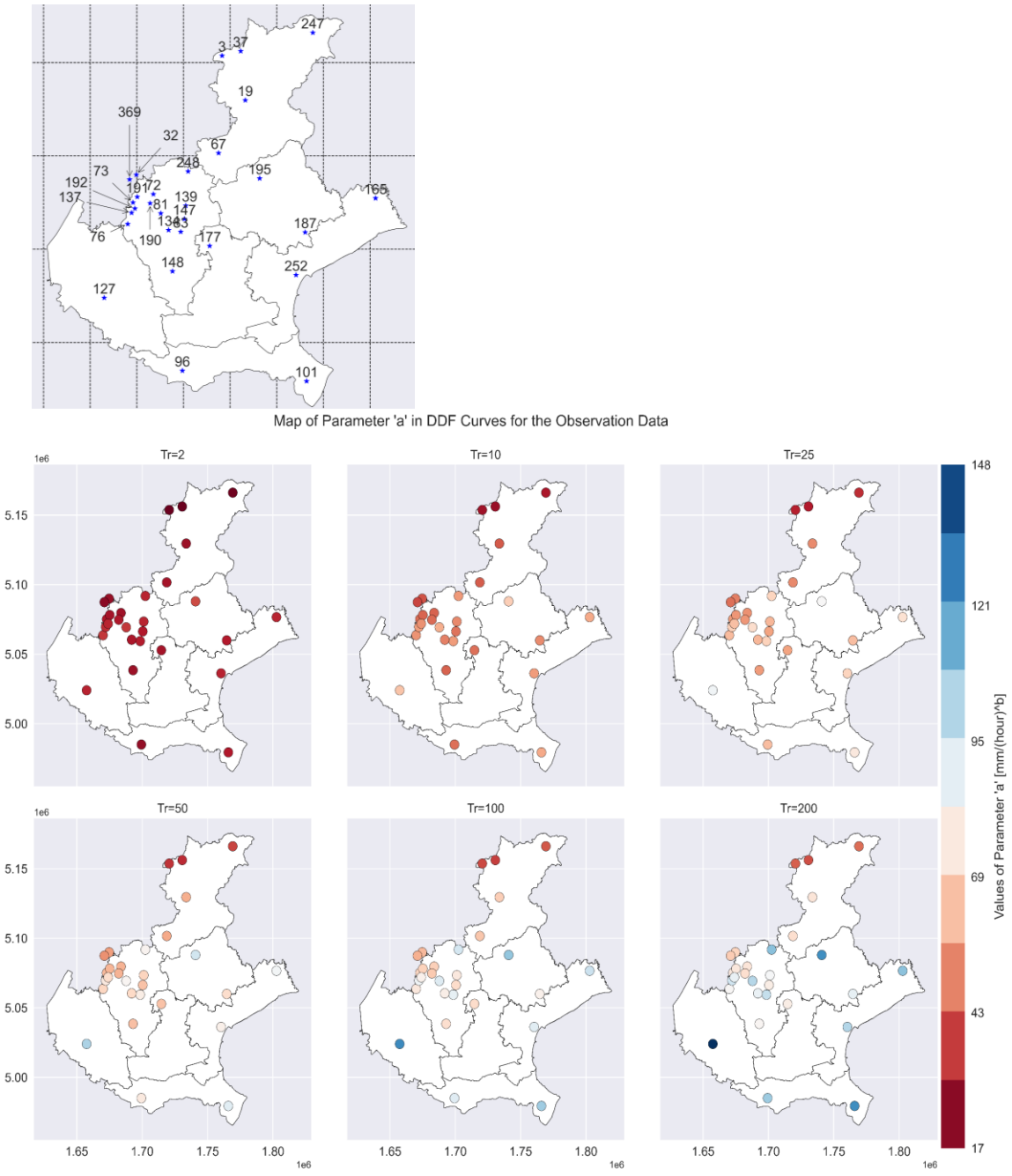

Figure 3-30: Map of coefficient 'a' of DDF curves of observation data for various return periods.

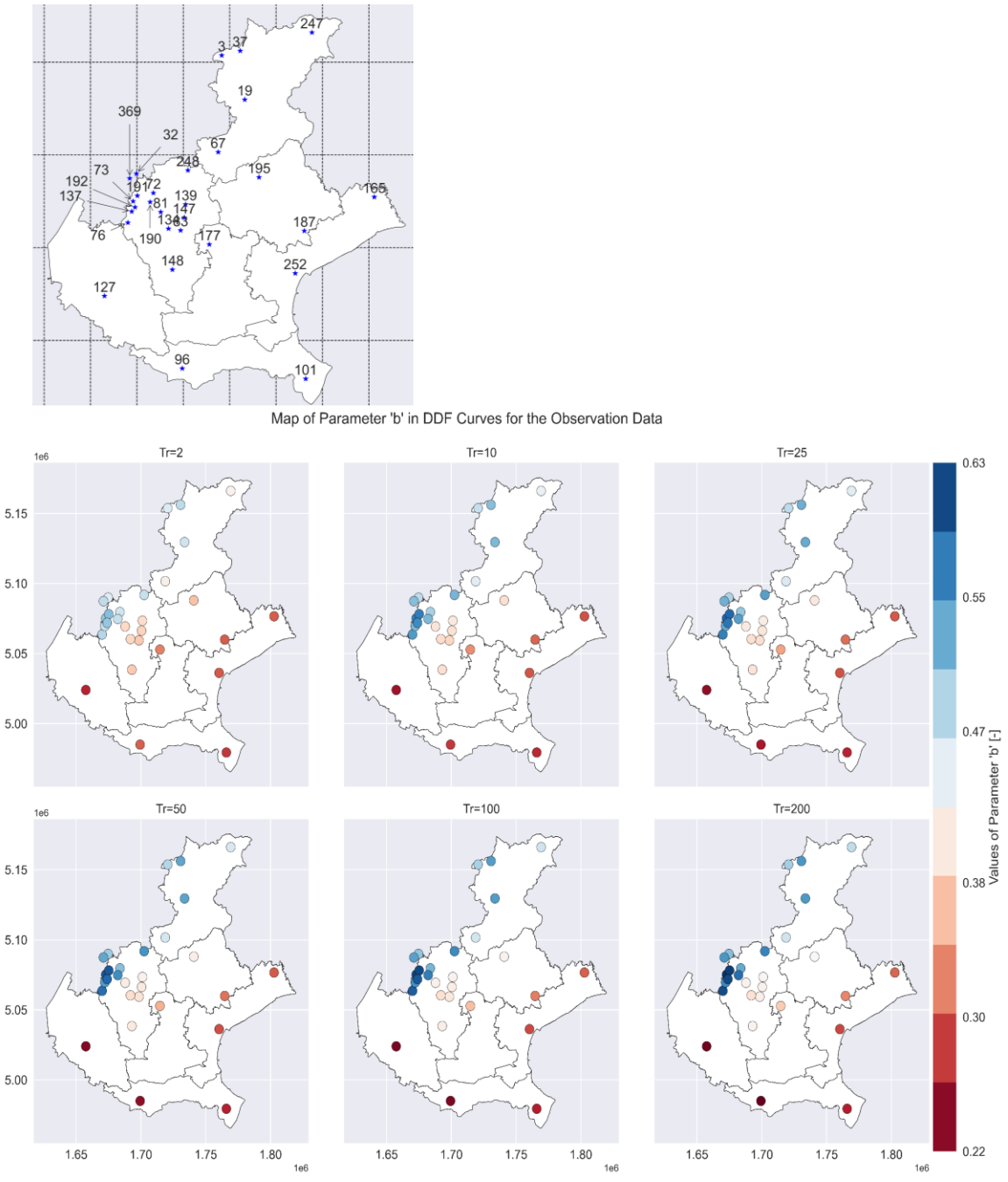

Figure 3-31: Map of exponent 'b' of the DDF curves of observation data for various return periods.

3.4.2. CPM historical (1996-2005) without correction

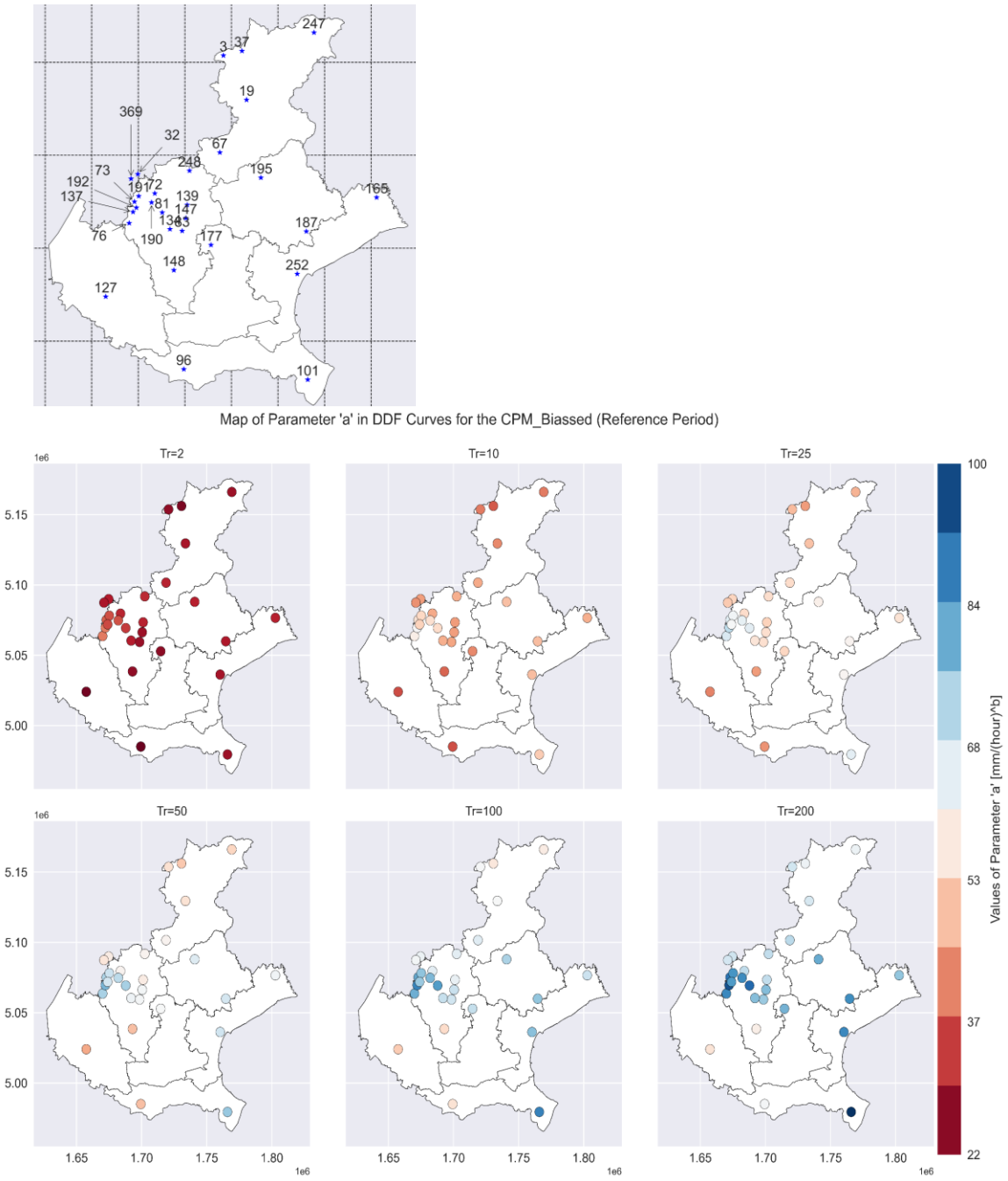

Figure 3-32: Map of coefficient 'a' of DDF curves for biased CPM historical (1996-2005) for various return periods.

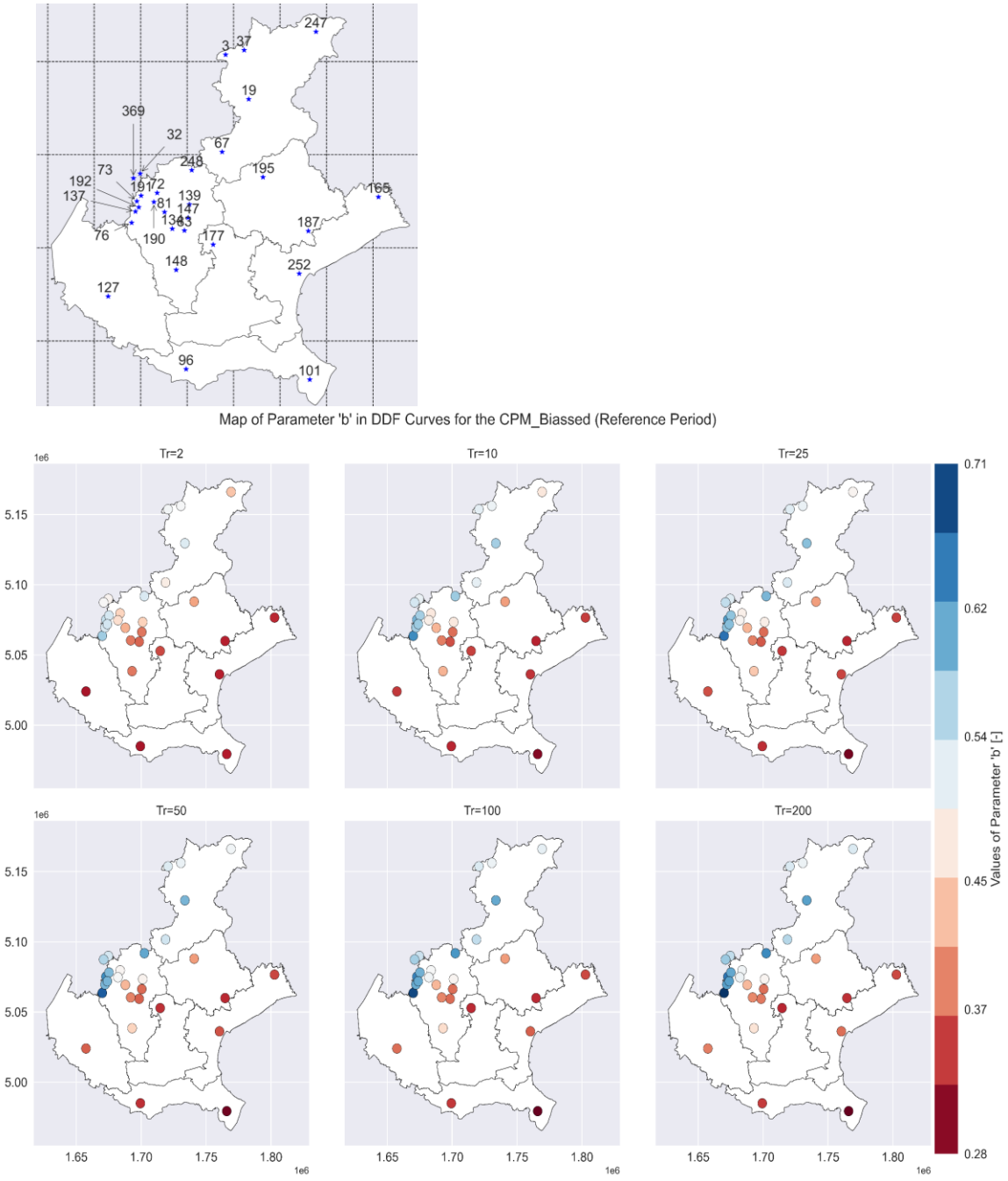

Figure 3-33: Map of exponent 'b' of DDF curves for biased CPM historical (1996-2005) for various return periods.

3.4.3. CPM historical (1996-2005) bias corrected

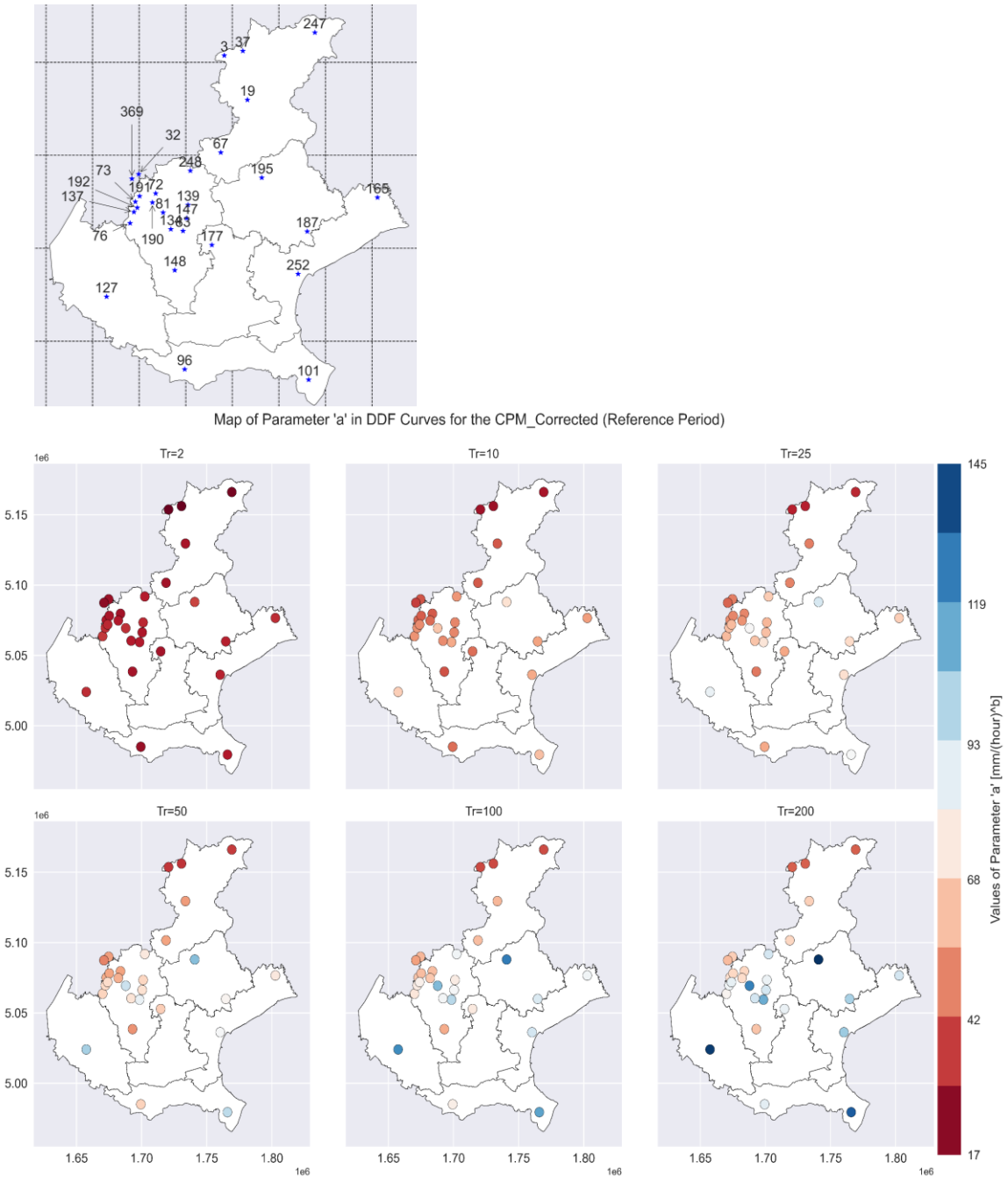

Figure 3-34: Map of coefficient 'a' of DDF curves for bias corrected CPM historical (1996-2005) for various return periods.

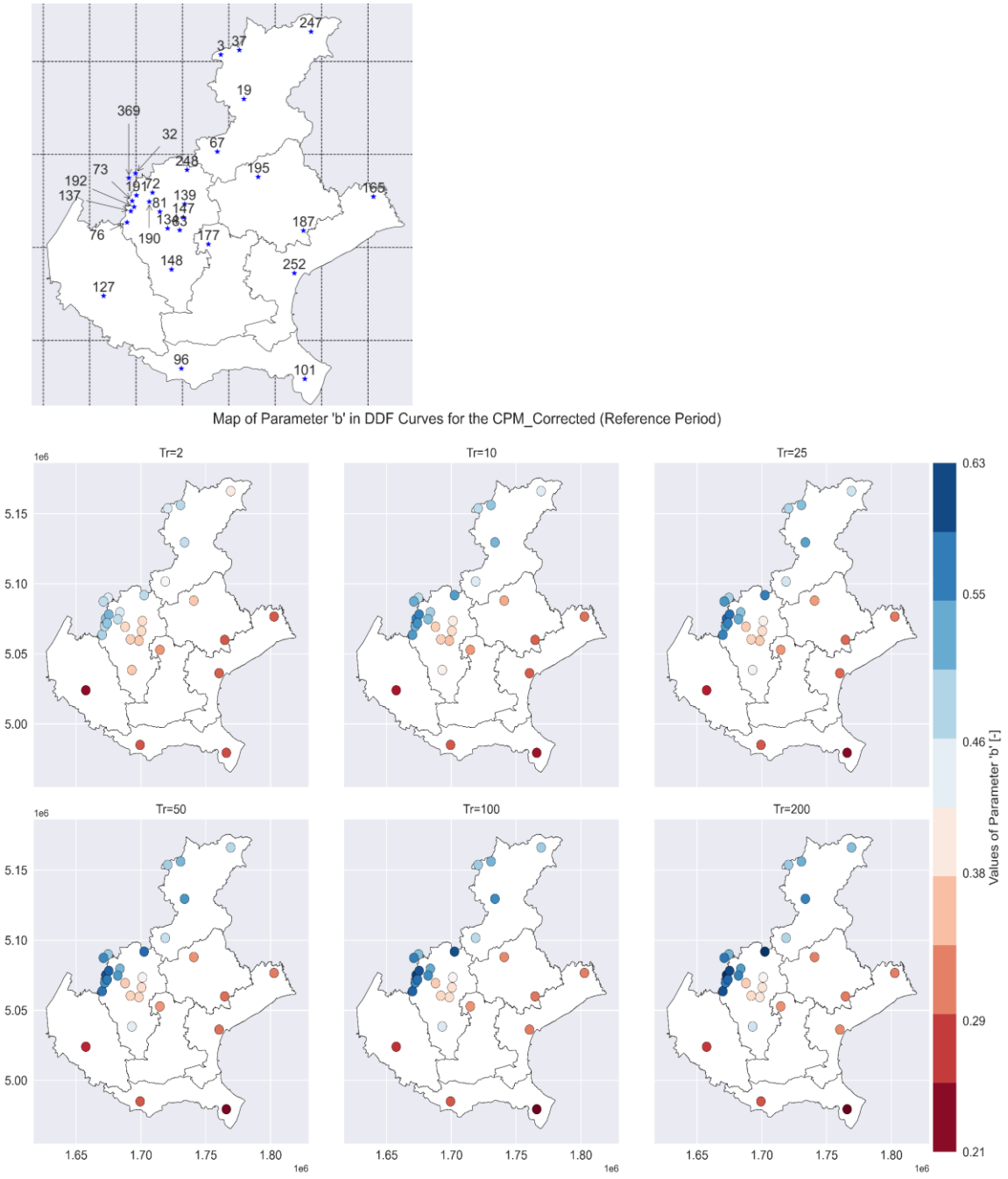

Figure 3-35: Map of exponent 'b' of DDF curves for bias corrected CPM historical (1996-2005) for various return periods.

3.4.4. CPM near future (2040-2049) without correction

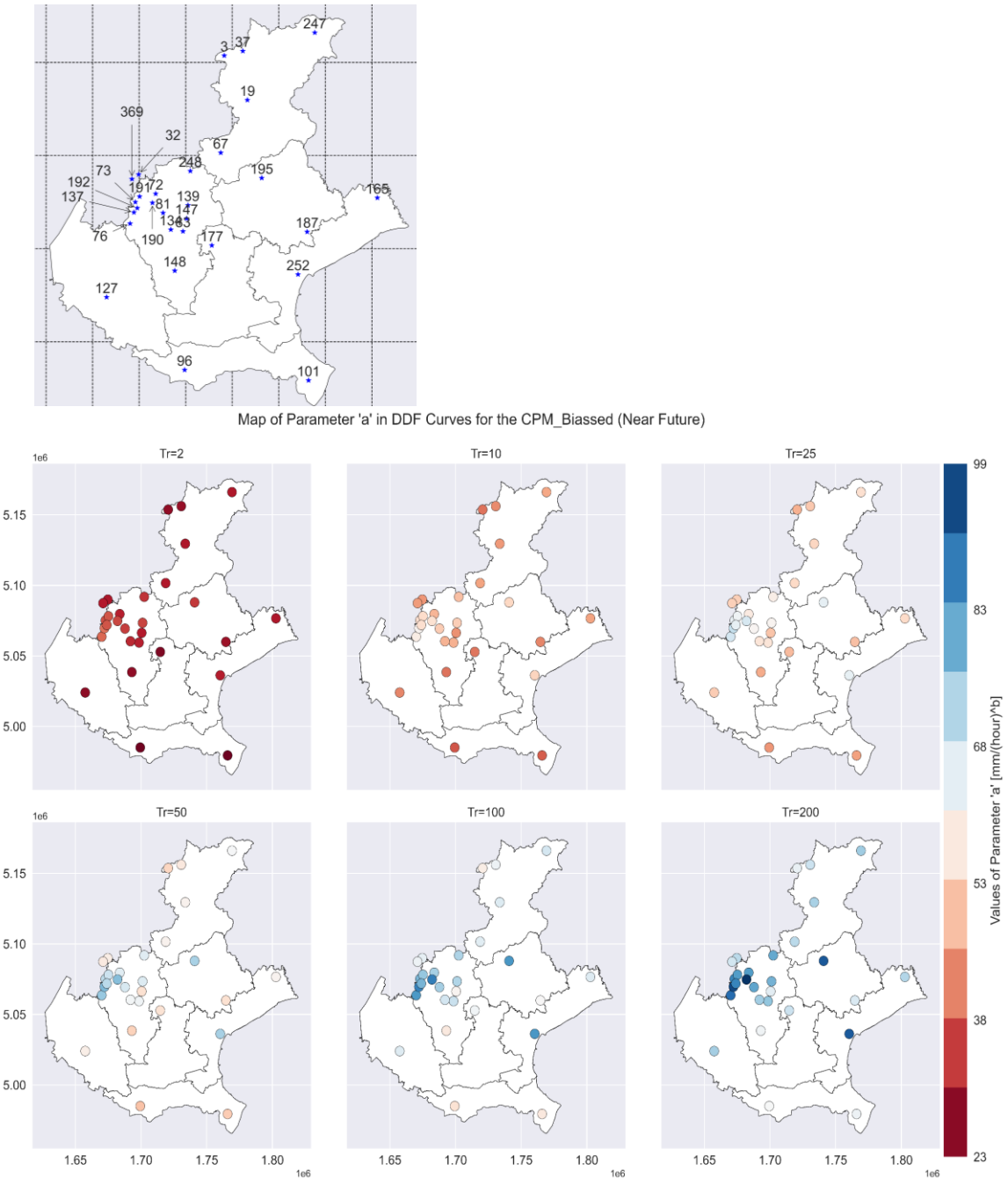

Figure 3-36: Map of coefficient 'a' of DDF curves for biased CPM near future (2040-2049) for various return periods.

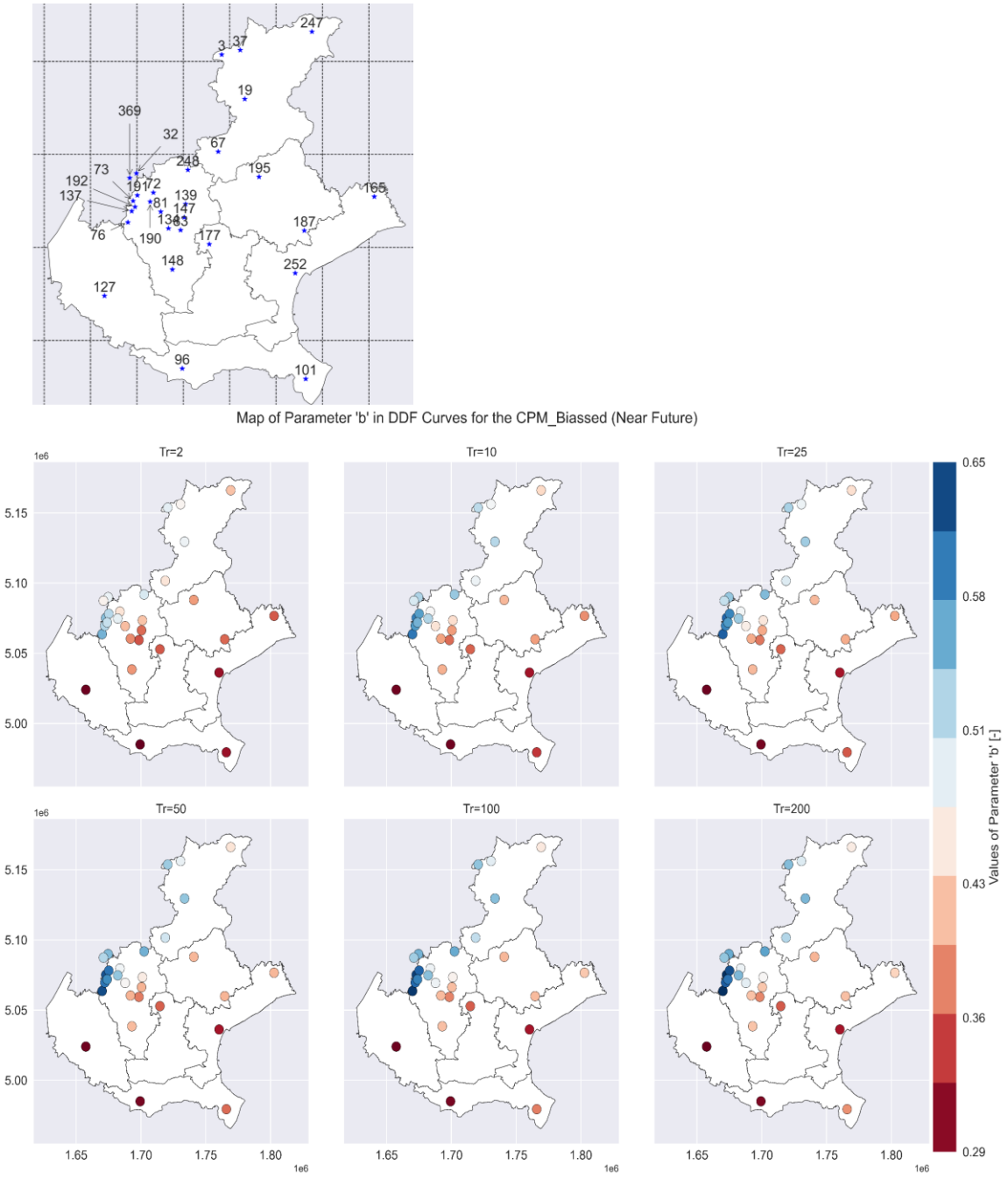

Figure 3-37: Map of exponent 'b' of DDF curves for biased CPM near future (2040-2049) for various return periods.

3.4.5. CPM near future (2040-2049) bias corrected

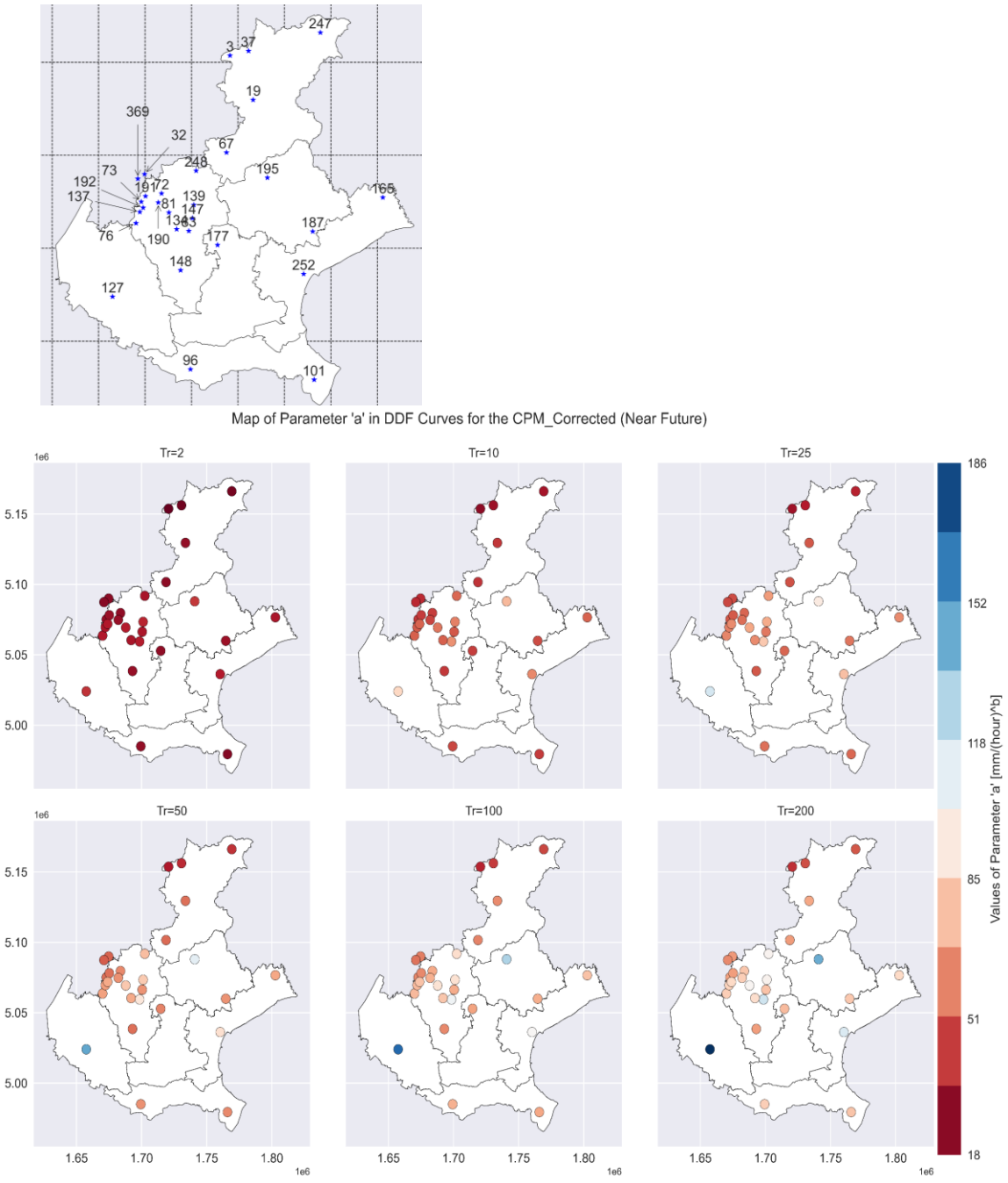

Figure 3-38: Map of coefficient 'a' of DDF curves for bias corrected CPM near future (2040-2049) for various return periods.

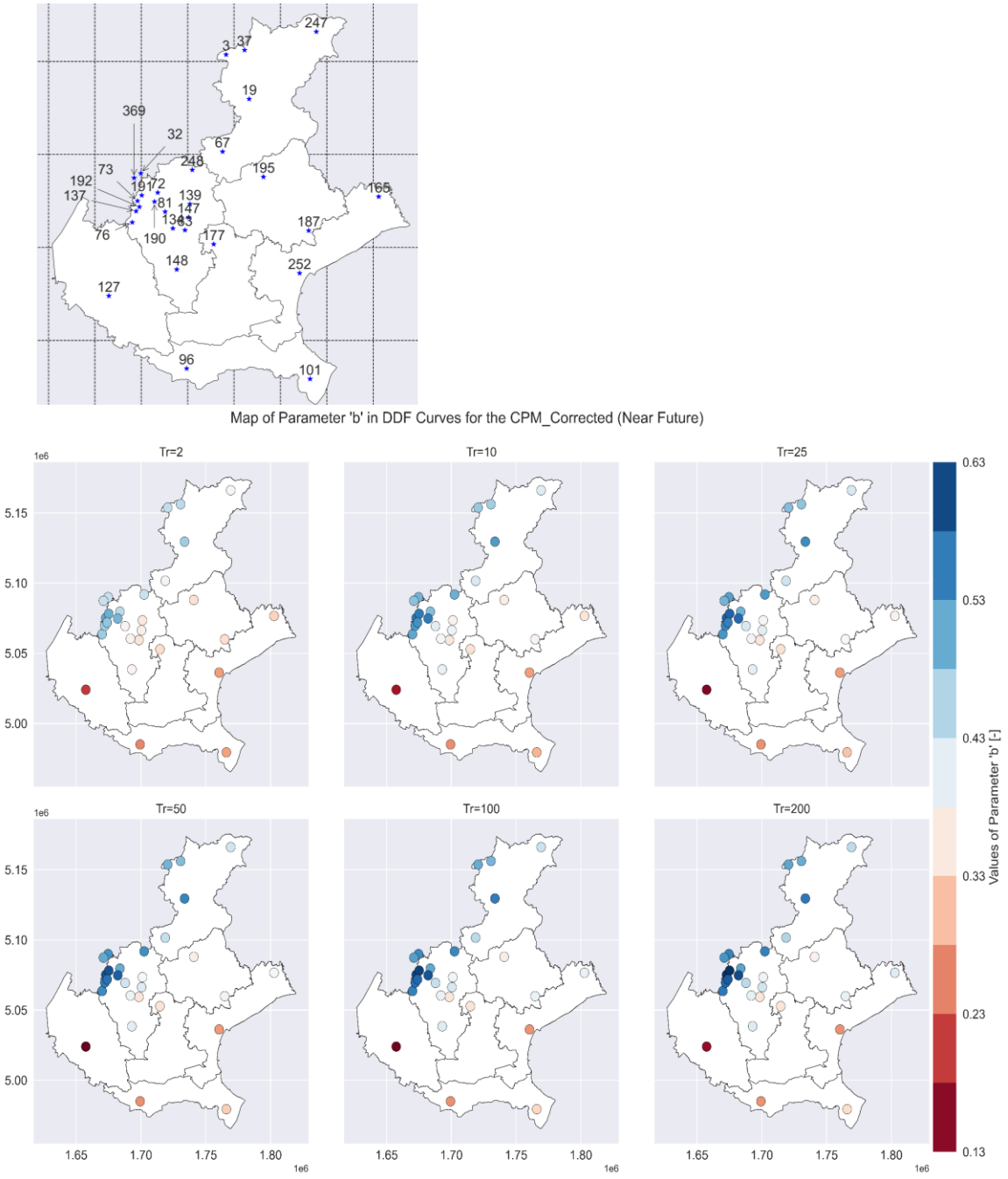

Figure 3-39: Map of exponent 'b' of DDF curves for bias corrected CPM near future (2040-2049) for various return periods.

3.4.6. CPM far future (2090-2099) without correction

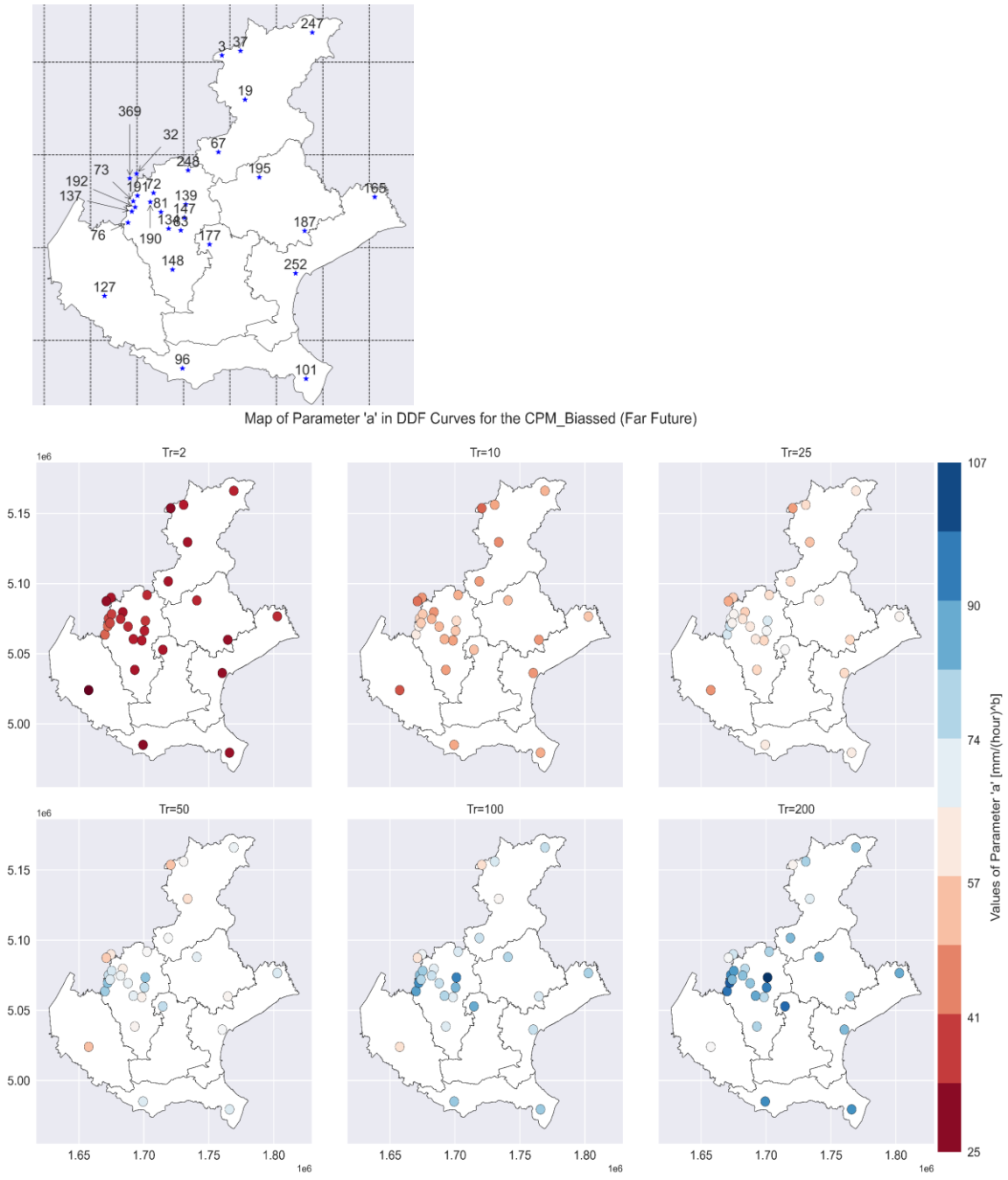

Figure 3-40: Map of coefficient 'a' of DDF curves for biased CPM far future (2090-2099) for various return periods.

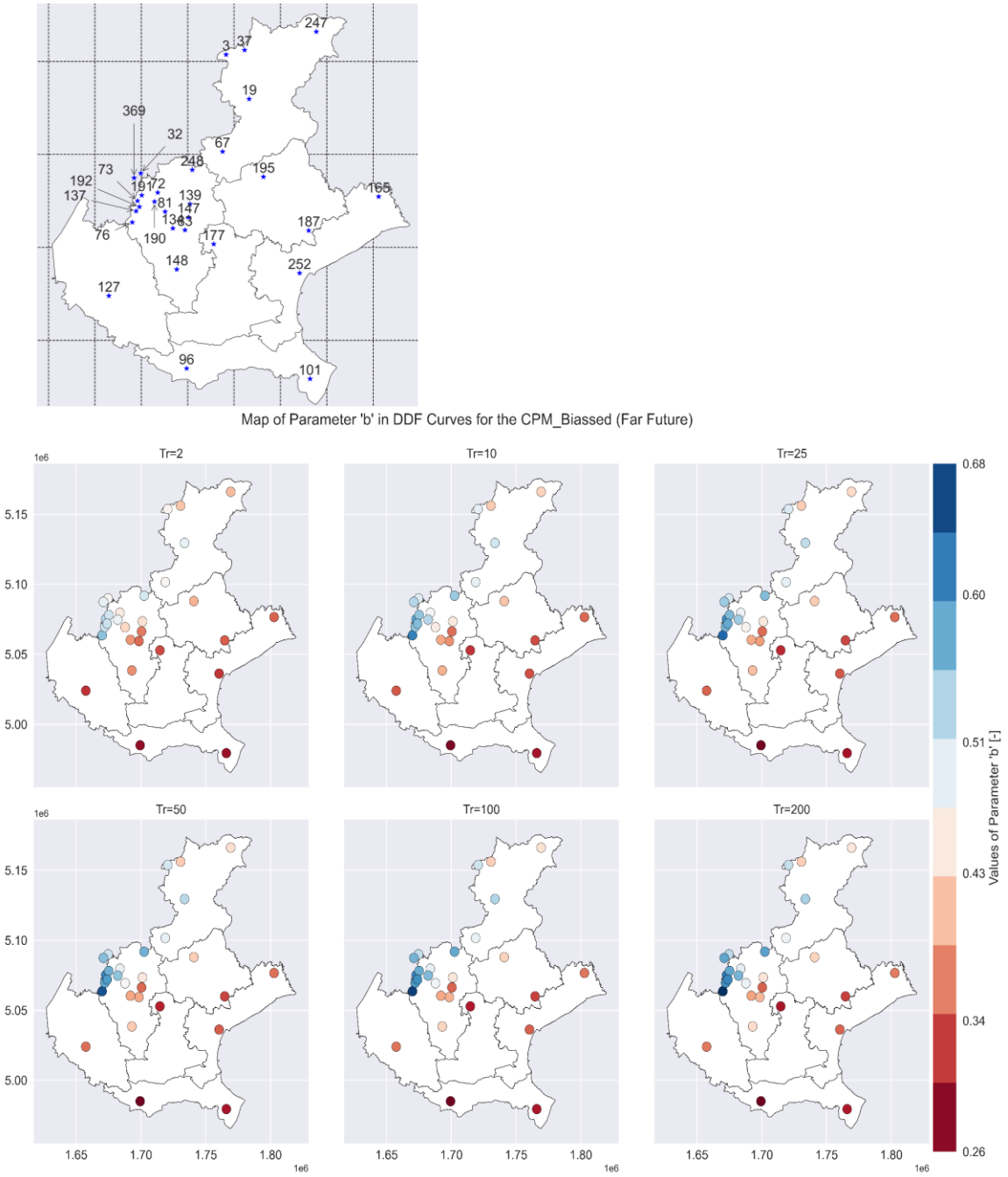

Figure 3-41: Map of exponent 'b' of DDF curves for biased CPM far future (2090-2099) for various return periods.

3.4.7. CPM far future (2090-2099) bias corrected

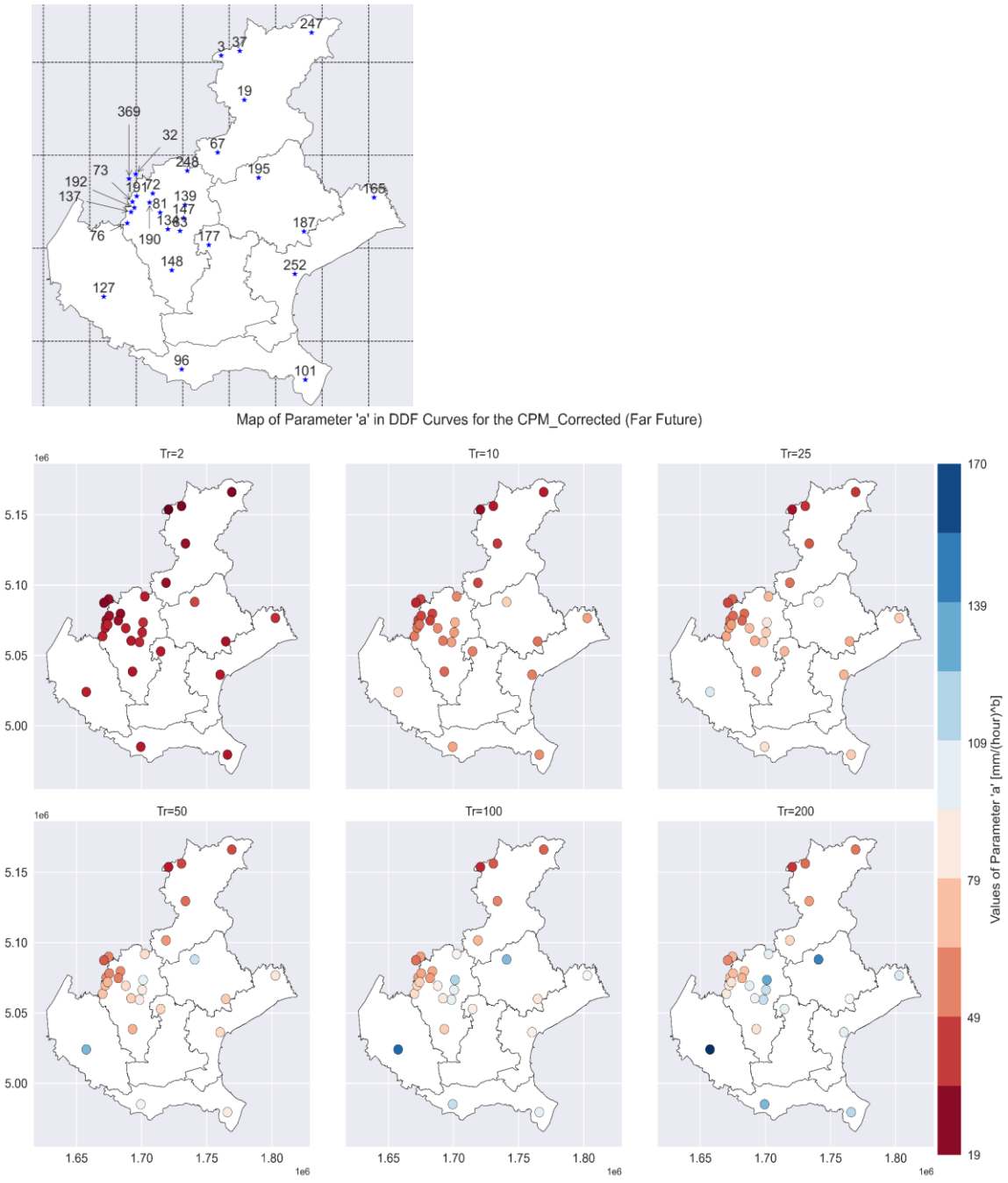

Figure 3-42: Map of coefficient 'a' of DDF curves for bias corrected CPM far future (2090-2099) for various return periods.

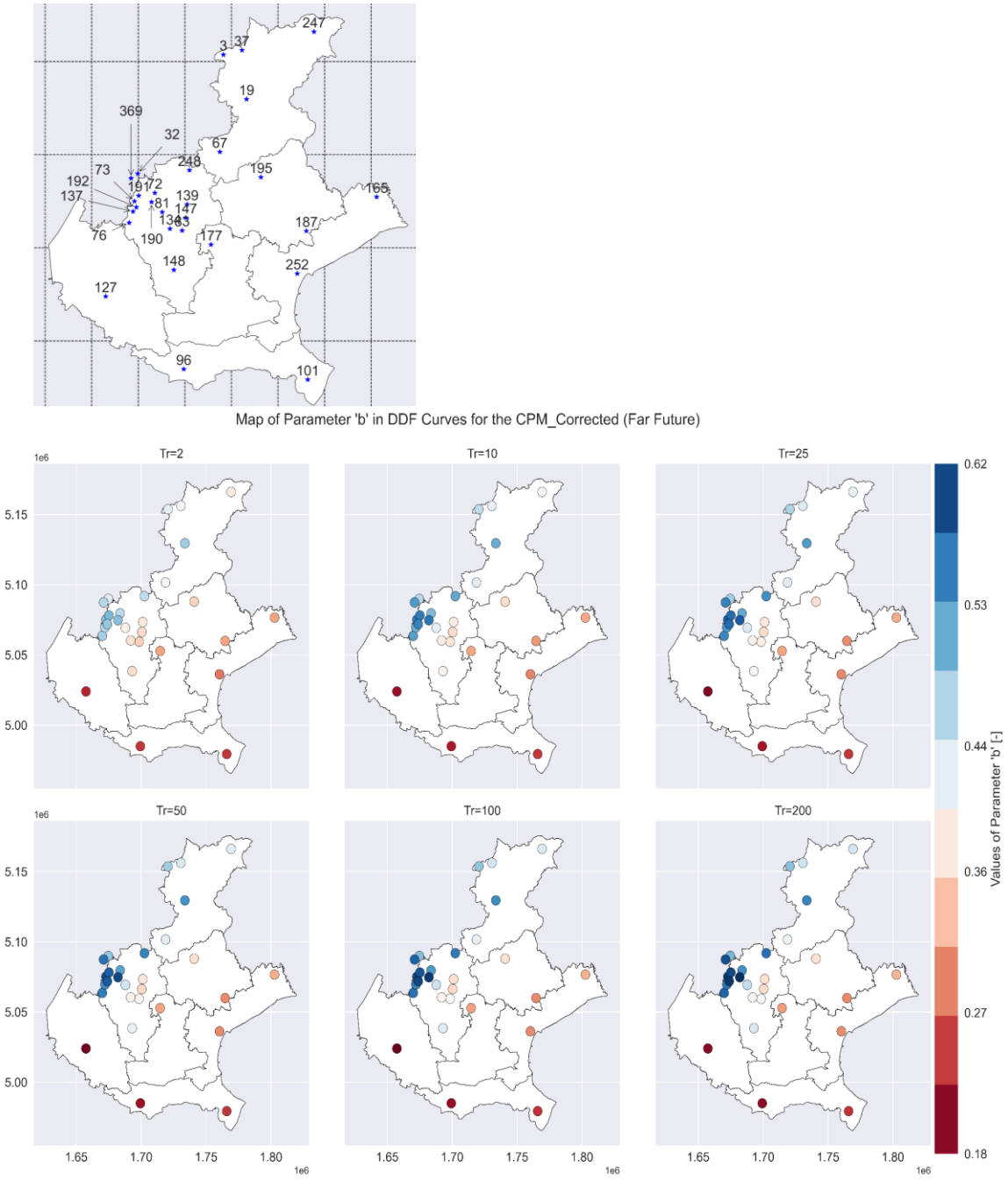

Figure 3-43: Map of exponent 'b' of DDF curves for bias corrected CPM far future (2090-2099) for various return periods.

3.4.8. Boxplot of parameters of DDF curve for all datasets

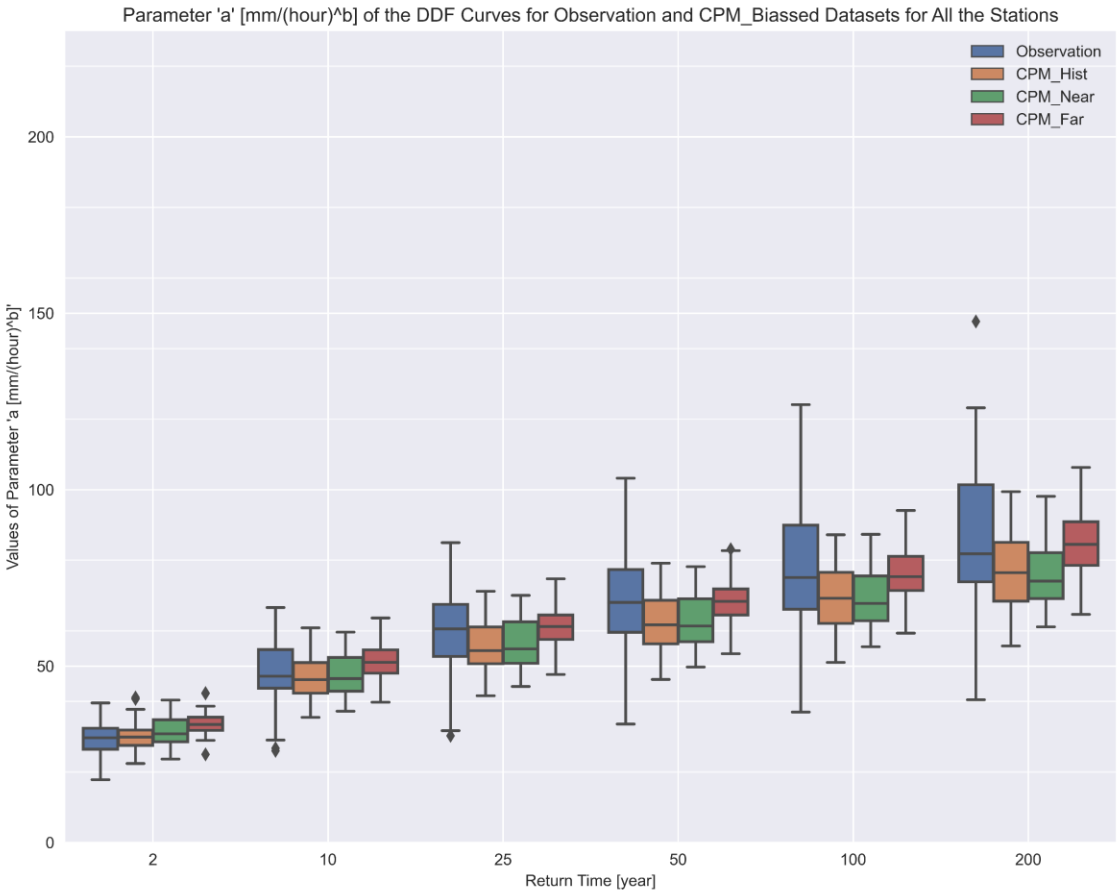

Figure 3-44: Boxplot of coefficient 'a' of DDF curves for all the datasets, CPM_Hist refers to the CPM run in reference period (1996-2005) and CPM_Near and CPM_Far refer to CPM projection for (2040-2049) and (2090-2099) respectively. This boxplot is based on biased CPMs.

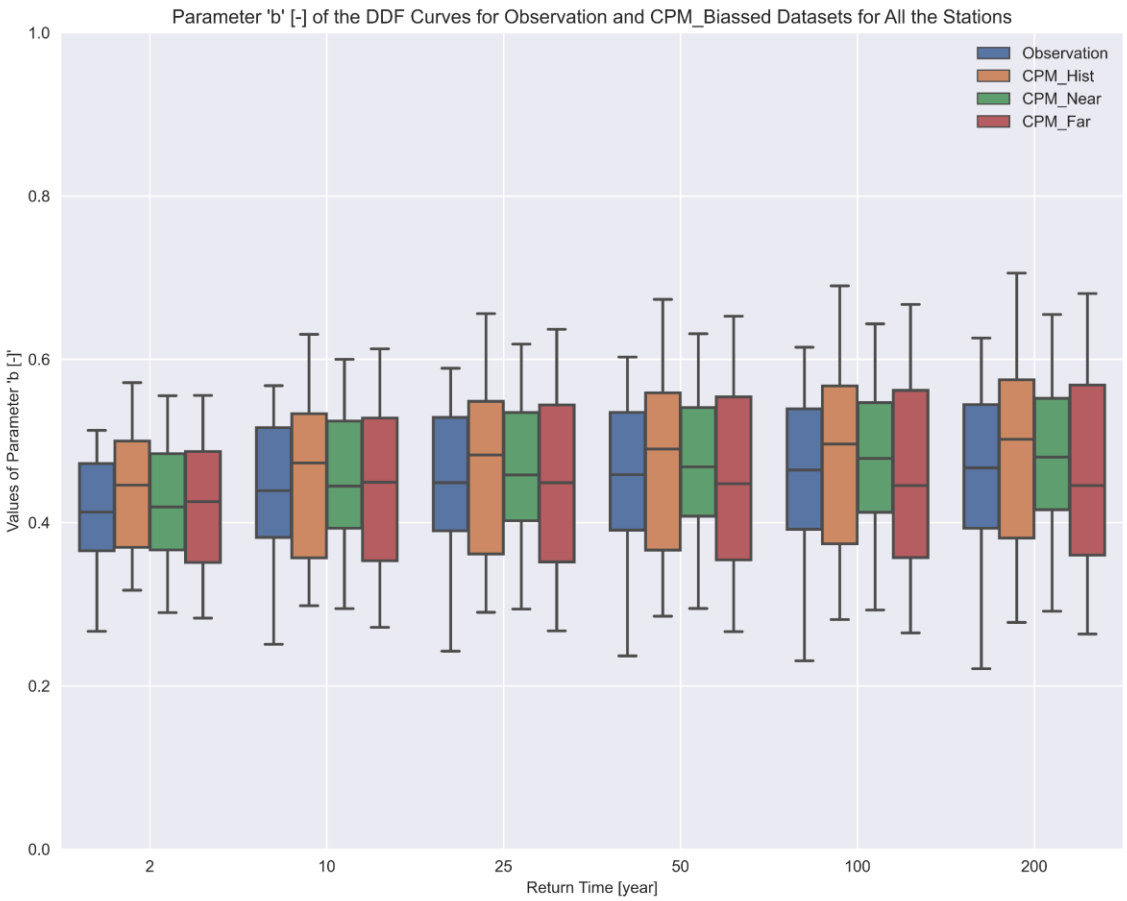

Figure 3-45: Boxplot of exponent 'b' of DDF curves for all the datasets, CPM_Hist refers to the CPM run in reference period (1996-2005) and CPM_Near and CPM_Far refer to CPM projection for (2040-2049) and (2090-2099) respectively. This boxplot is based on biased CPMs.

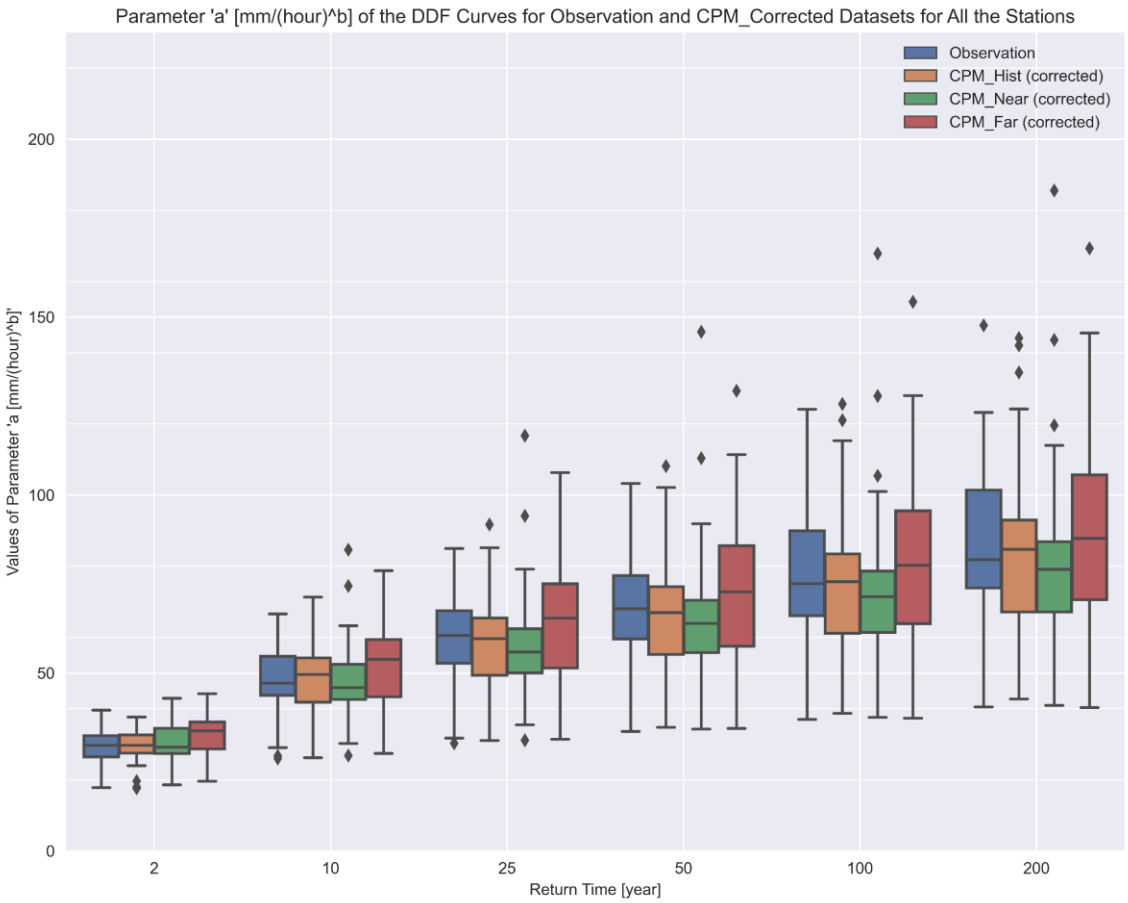

Figure 3-46: Boxplot of coefficient 'a' of DDF curves for all the datasets, CPM_Hist refers to the CPM run in reference period (1996-2005) and CPM_Near and CPM_Far refer to CPM projection for (2040-2049) and (2090-2099) respectively. This boxplot is based on corrected CPMs.

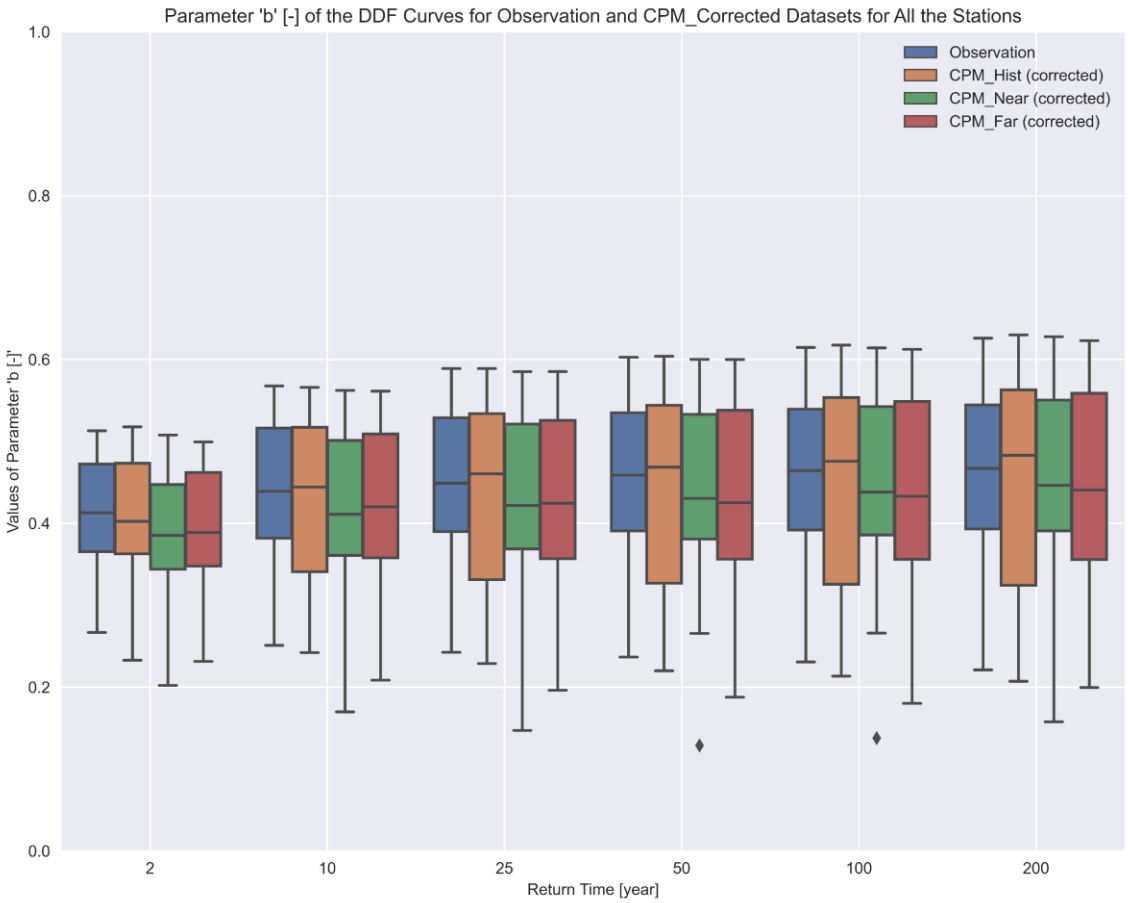

Figure 3-47: Boxplot of exponent 'b' of DDF curves for all the datasets, CPM_Hist refers to the CPM run in reference period (1996-2005) and CPM_Near and CPM_Far refer to CPM projection for (2040-2049) and (2090-2099) respectively. This boxplot is based on corrected CPMs.

3.5. Evaluation of CC scaling

Here the mean temperature difference between the reference period (1996 – 2005) and the projected period (2090 – 2099) will be presented along with the corresponding percent difference in mean rain intensity and mean annual maximum rain for each of the stations. Then based on the projected increase in warming and the CC relationship future rain intensities were computed and incorporated into the DDFs to estimate quantiles with different return time.

Figure 3-48 illustrates the mean temperature difference between CPM historical and CPM far future. Figure 3-49 shows the percent difference in mean rain intensity between the CPM of reference period and the 2090 – 2099 period across all the durations. Figure 3-50 represents the percent difference in mean annual maximum rain intensity between periods (1996 – 2005) and (2090 – 2099).

Figure 3-51 and Figure 3-52 show the percent difference per degree Celsius for the cases of mean rain intensity and mean annual maximum rain between the reference period and the far future.

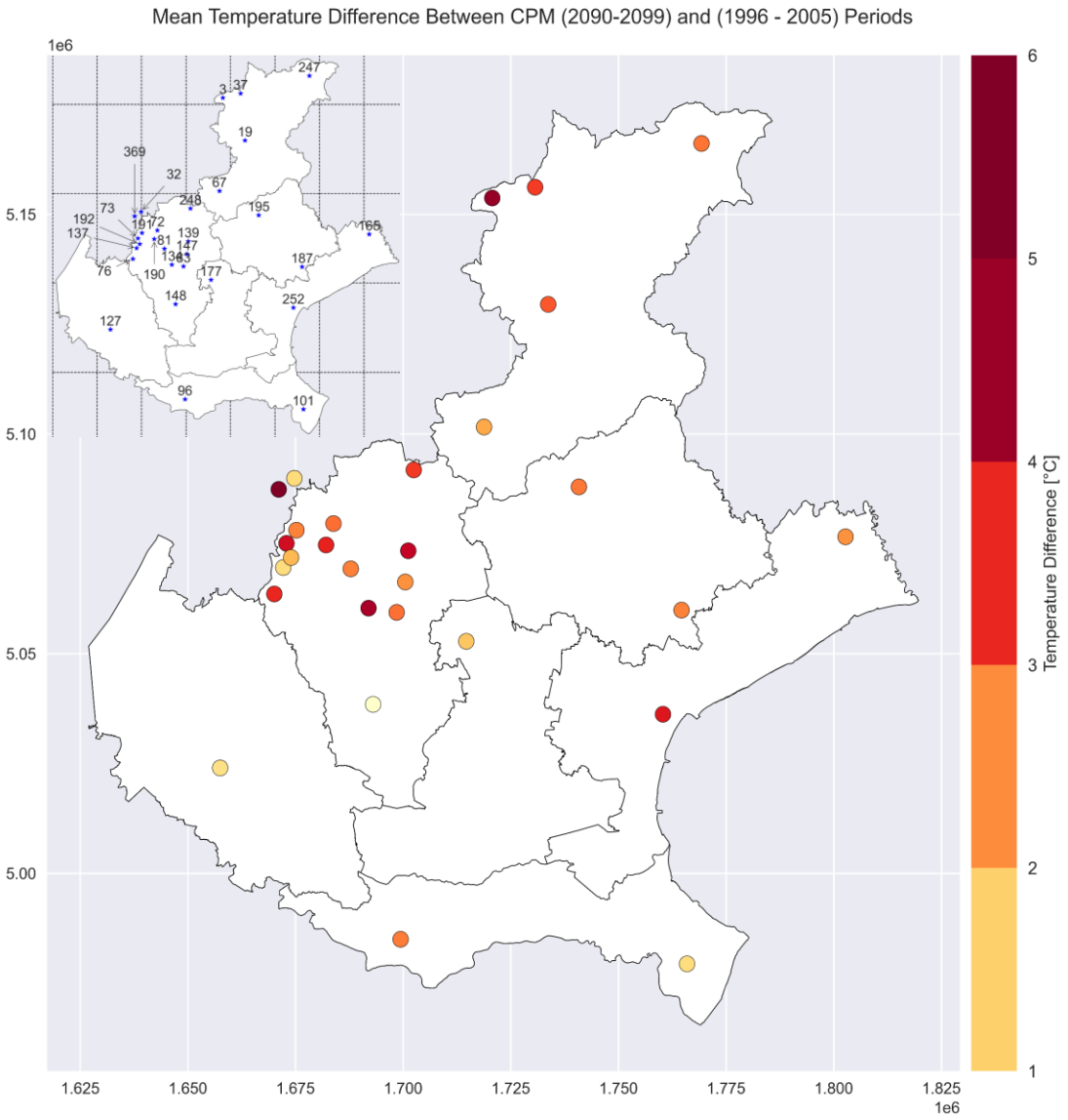

Figure 3-48: Map of mean temperature difference between CPM historical (1996-2005) and CPM far future run (2090-2099).

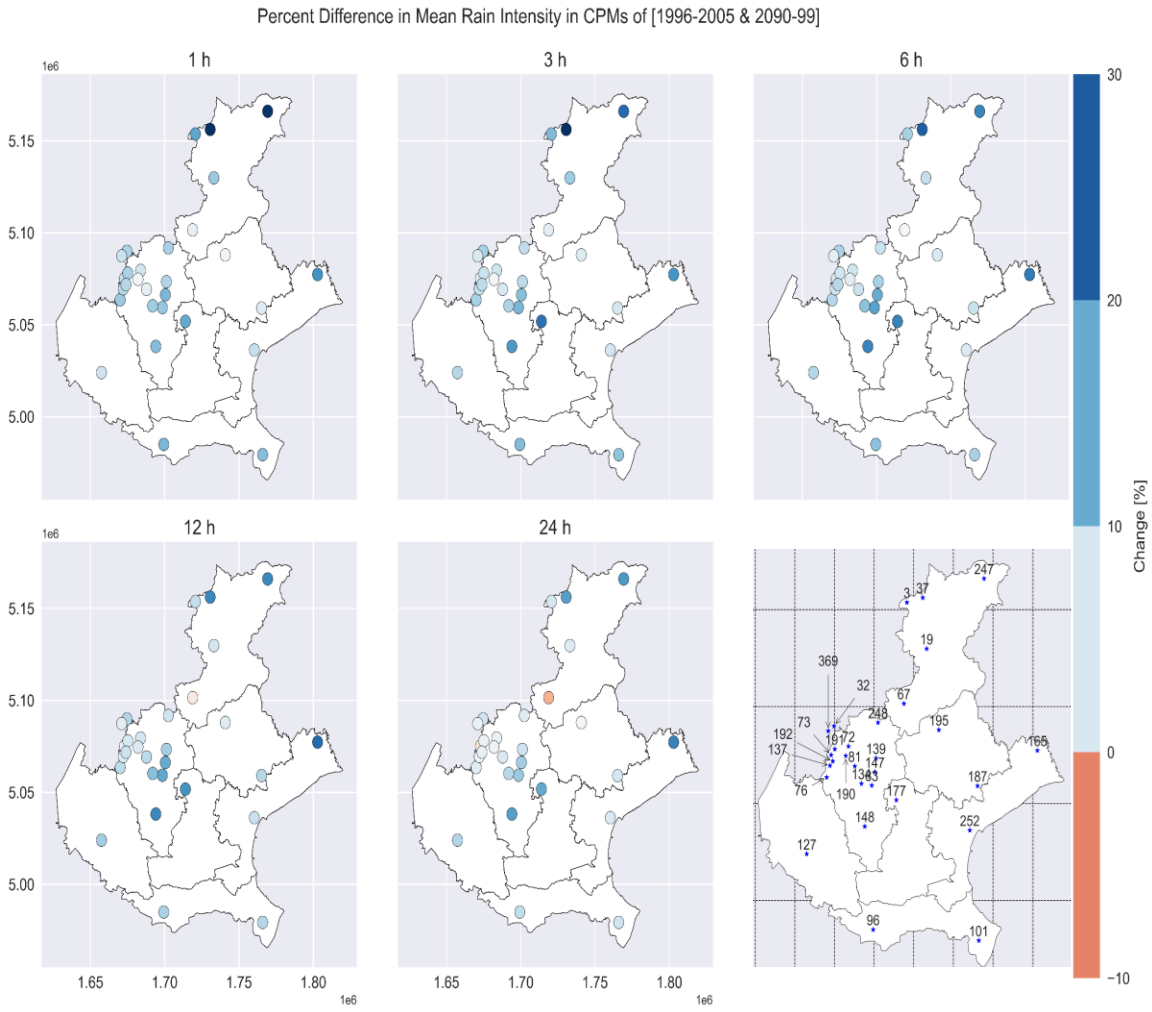

Figure 3-49: Map of percent change in mean rain intensity between CPMs (1996-2005) and (2090-2099).

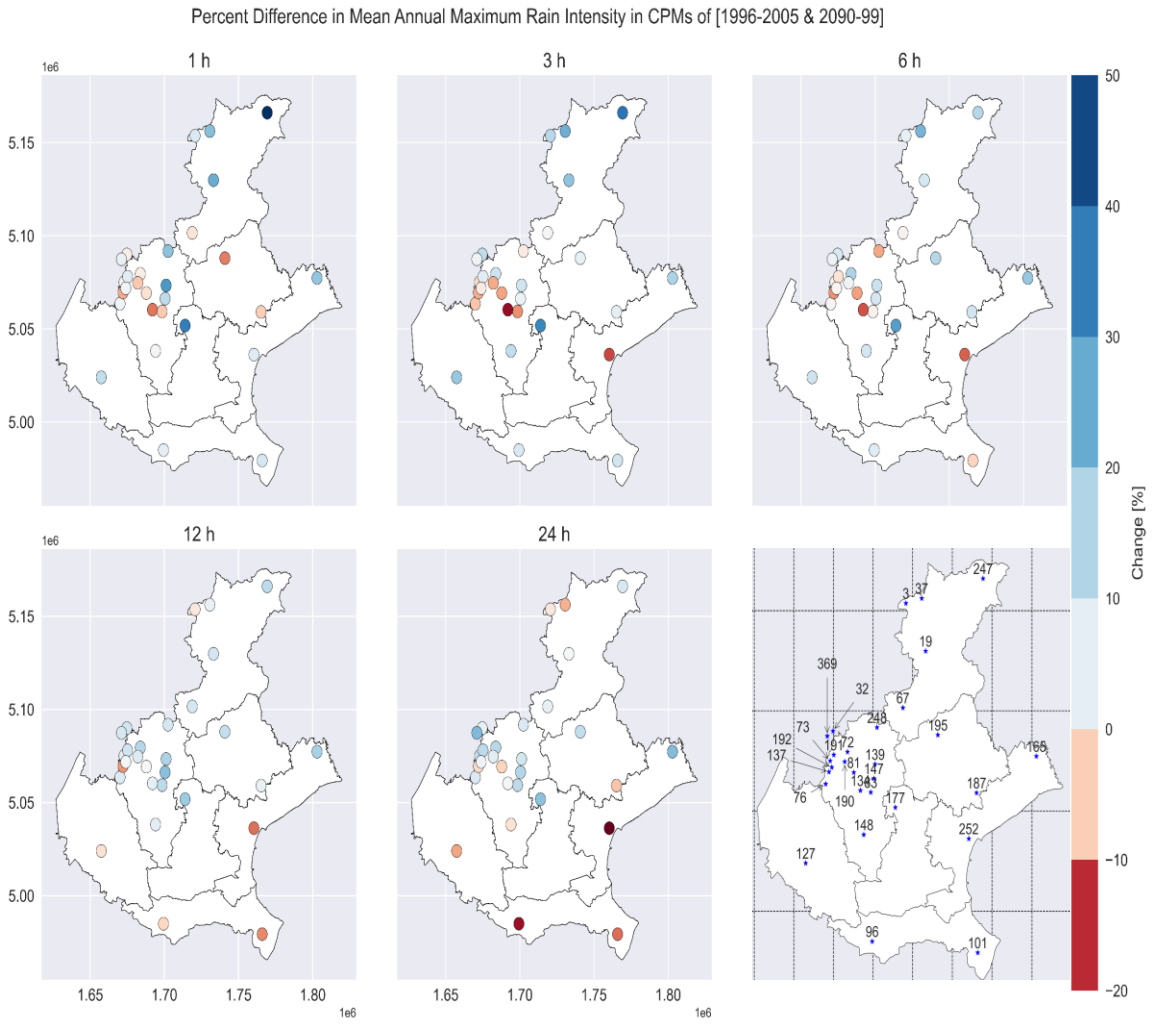

Figure 3-50: Map of percent change in mean annual maximum rain intensity between CPMs (1996-2005) and (2090-2099).

Figure 3-51: Map of percent change in mean rain intensity per ℃ change in warming between CPMs (1996-2005) and (2090-2099).

Figure 3-52: Map of percent change in mean annual maximum rain intensity per ℃ change in warming between CPMs (1996-2005) and (2090-2099).

3.5.1. Derivation of DDF curves based on CC scaling

Based on the rationale behind the CC relationship discussed in section 2.1, we can compute the future rain intensities according to most likely local increase in temperatures utilizing formula 2 in page 13.

Figure 3-53 and Figure 3-54 show the parameters of DDF curves based on CC scaling. In Figure 3-55 and Figure 3-56 the boxplots for these parameters are represented. One can see that projected quantiles using CC scaling are overestimated with respect to those obtained from corrected CPM projections across all return periods.

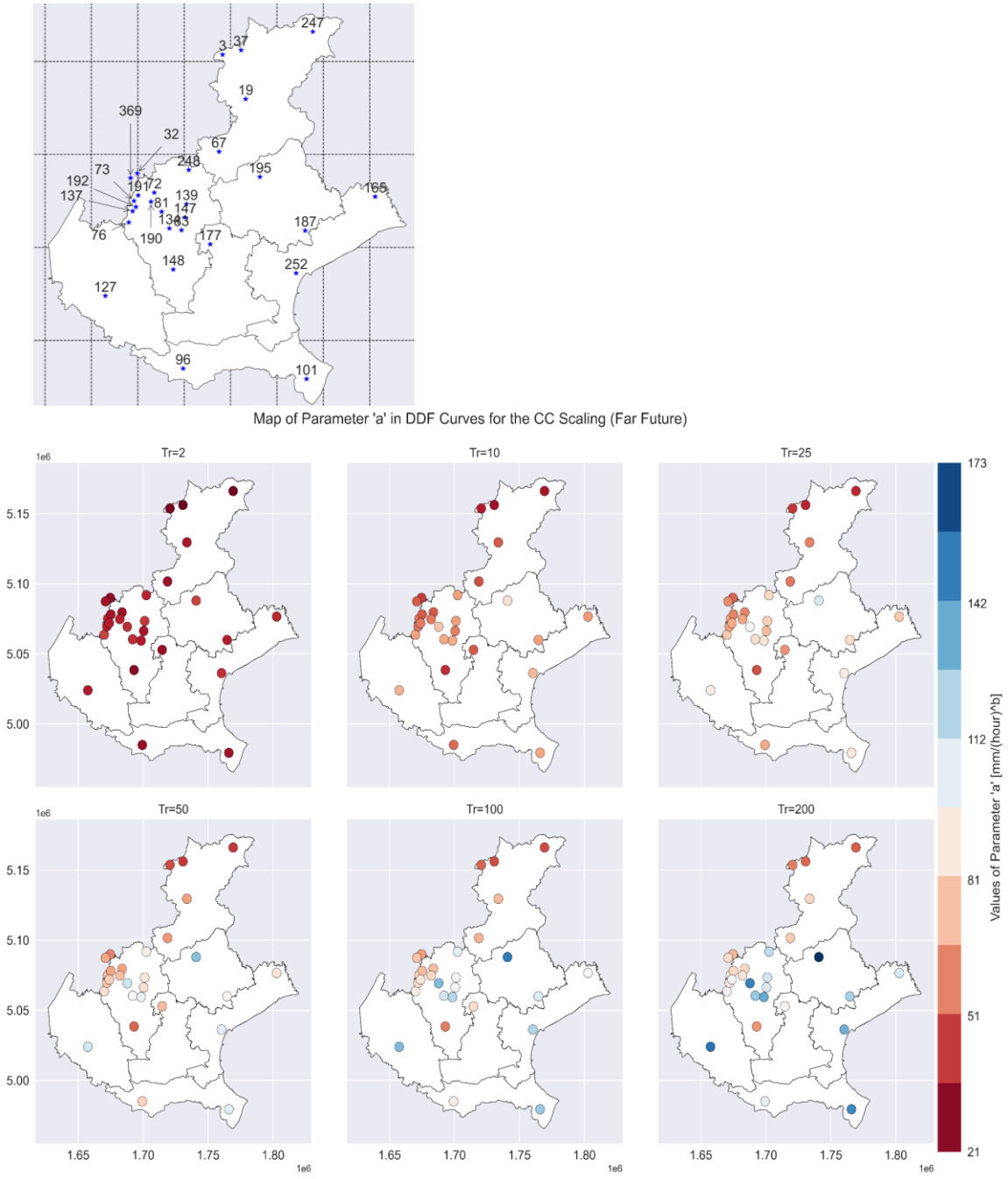

Figure 3-53: Map of coefficient 'a' of DDF curves for CC projection based on temperature projected according to far future scenario (2090-2099) for various return periods.

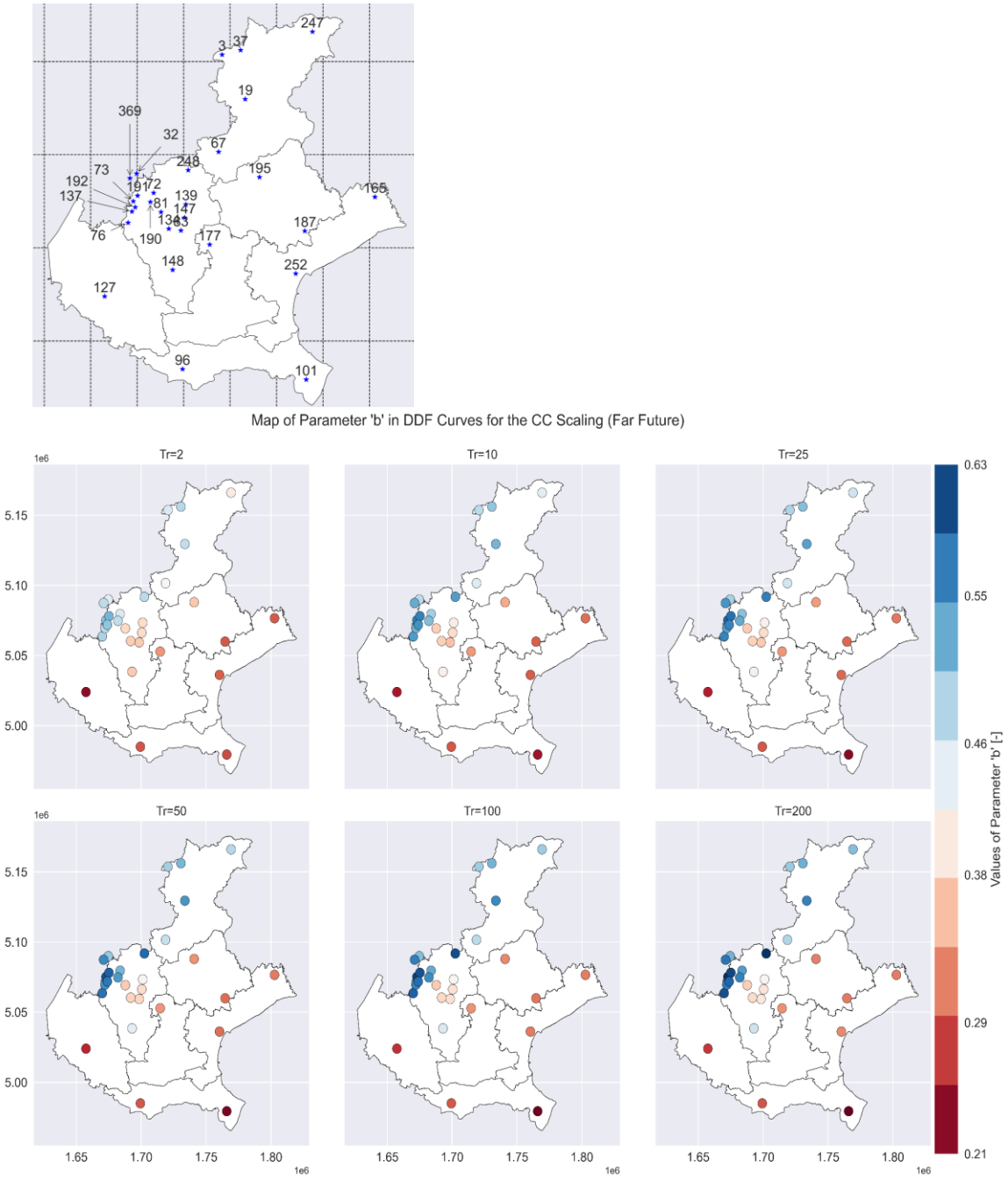

Figure 3-54: Map of exponent 'b' of DDF curves for CC projection based on temperature projected according to far future scenario (2090-2099) for various return periods.

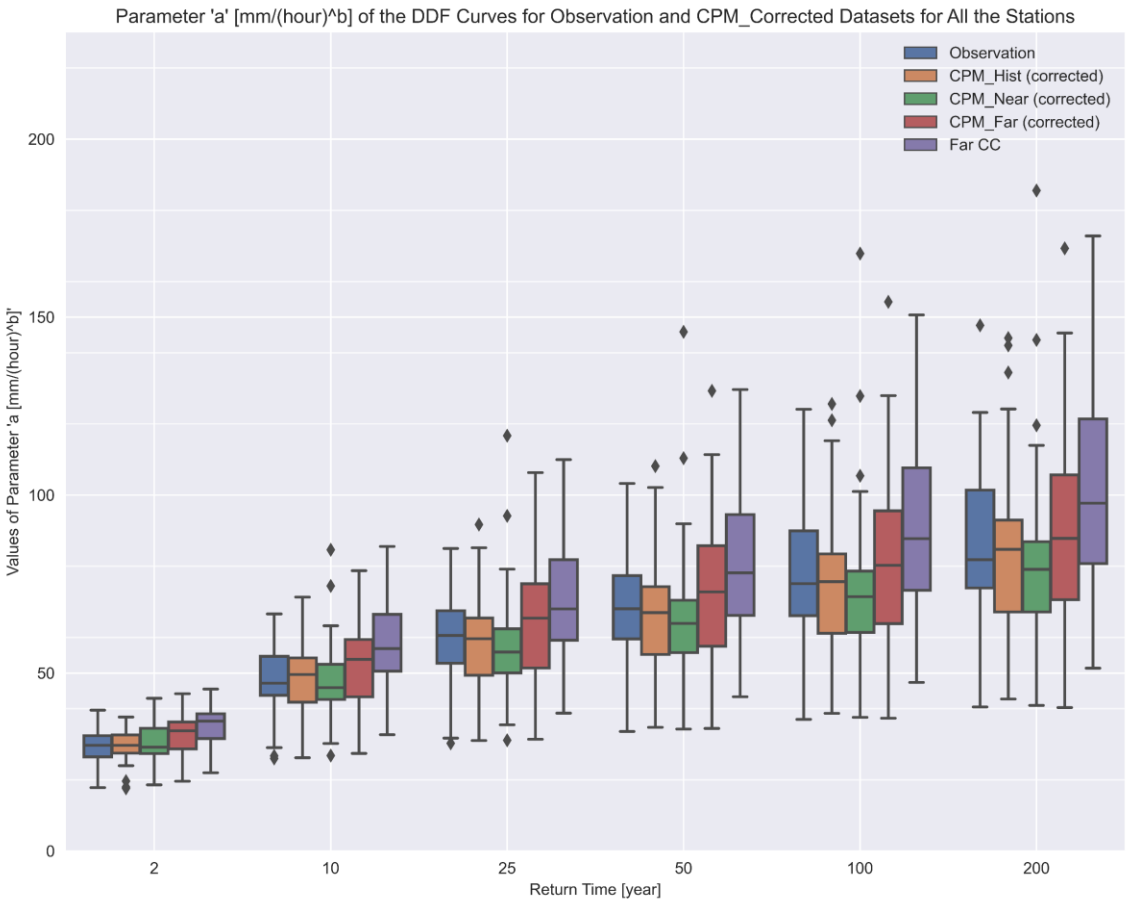

Figure 3-55: Boxplot of coefficient 'a' of DDF curves for all the datasets, CPM_Hist refers to the CPM run in reference period (1996-2005) and CPM_Near and CPM_Far refer to CPM projection for (2040-2049) and (2090-2099) respectively. And Far CC refers to CC projection based on temperature projected according to far future. This boxplot is based on corrected CPMs.

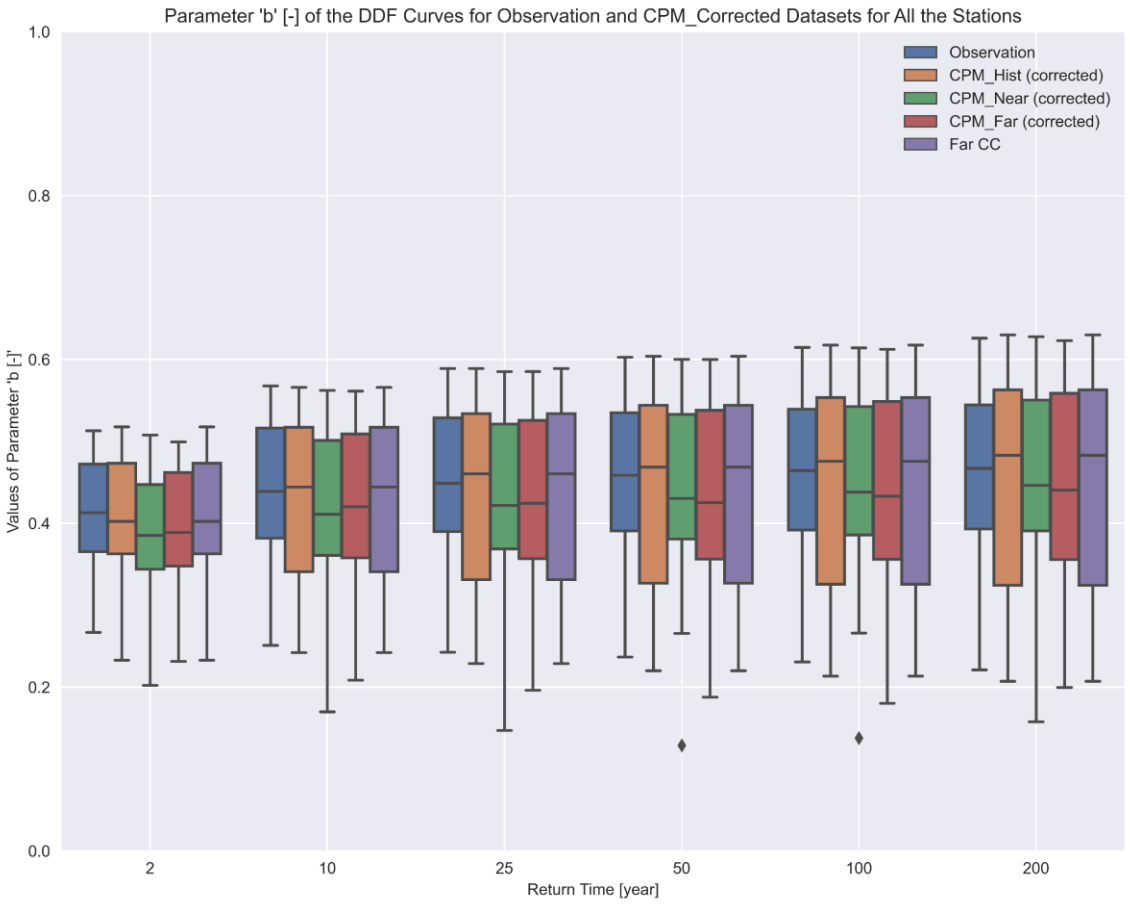

Figure 3-56: Boxplot of exponent 'b' of DDF curves for all the datasets, CPM_Hist refers to the CPM run in reference period (1996-2005) and CPM_Near and CPM_Far refer to CPM projection for (2040-2049) and (2090-2099) respectively. And Far CC refers to CC projection based on temperature projected according to far future. This boxplot is based on corrected CPMs.

3.6. Comparison of DDFs Curves for Few Examples Stations

In this section, we will present a comparison of the DDFs at specific station locations. This comparison encompasses both corrected and uncorrected CPM projections, as well as the CC scaled projections. Four station locations were chosen at random for this illustrative purpose, focusing on DDF curve comparisons for return periods of 10, 100, and 200 years. Specifically:

- Figure 3-57 and Figure 3-58 display the DDF curves for station 'TN_0032' located at Lavarone (Chiesa).
- Figure 3-59 and Figure 3-60 provide insights into the curves for station 'VE_0037' situated at Passo Falzarego.
- For station 'VE_0139' at Lusiana, the curves are presented in Figure 3-61 and Figure 3-62.
- Lastly, Figure 3-63 and Figure 3-64 present the DDF curves for station ‘VE_0247’ located at Casamazzagno.

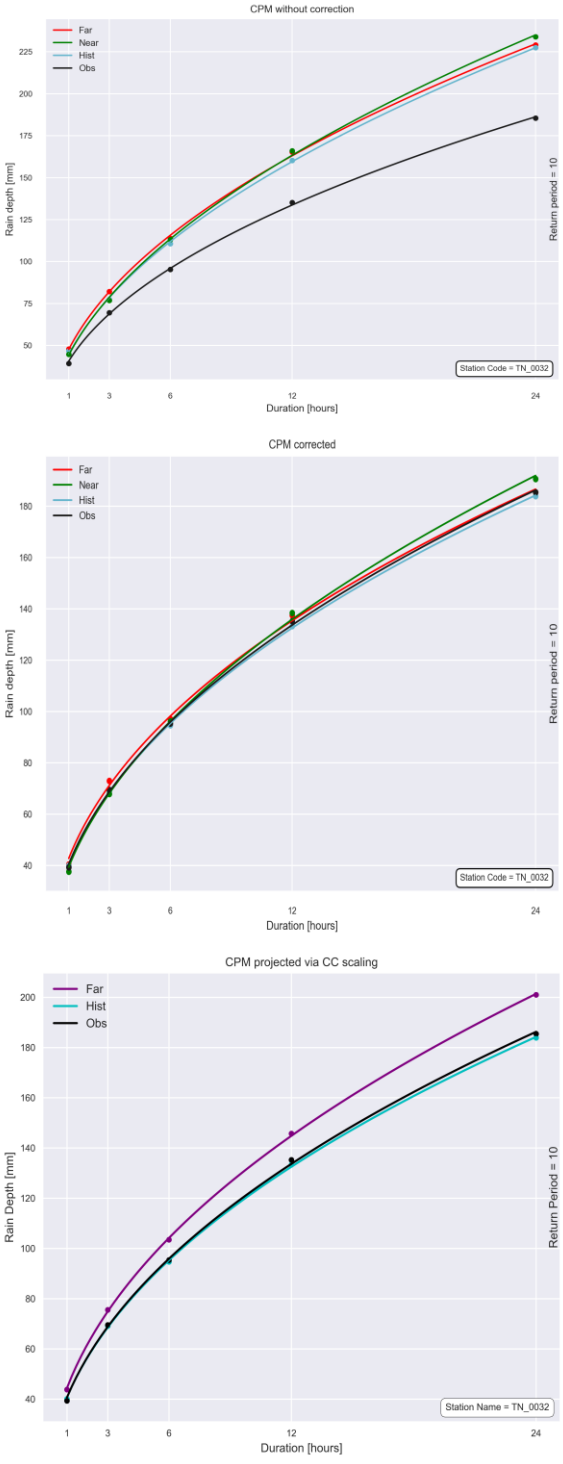

TN_0032: Lavarone (Chiesa)

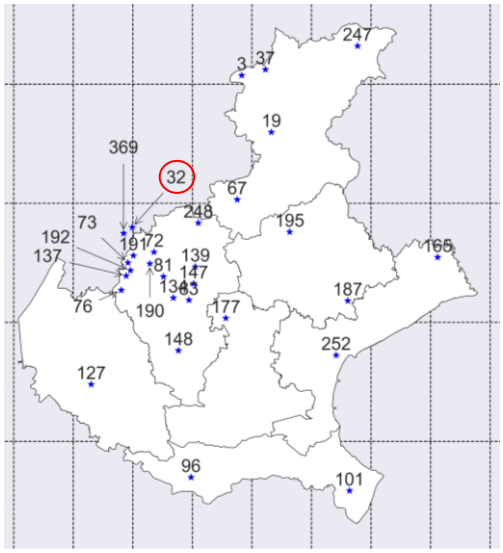

Figure 3-57: DDF curves for station 'TN_0032' for 10-yr return period. In the legend 'Far', 'Near', 'Hist' and 'Obs' refers to (2090-2099), (2040-2049), (1996-2005) CPM datasets and observation data respectively. The plots from top to bottom indicate projected DDF curves based on CPMs, CPM biased corrected, and CC scaled respectively.

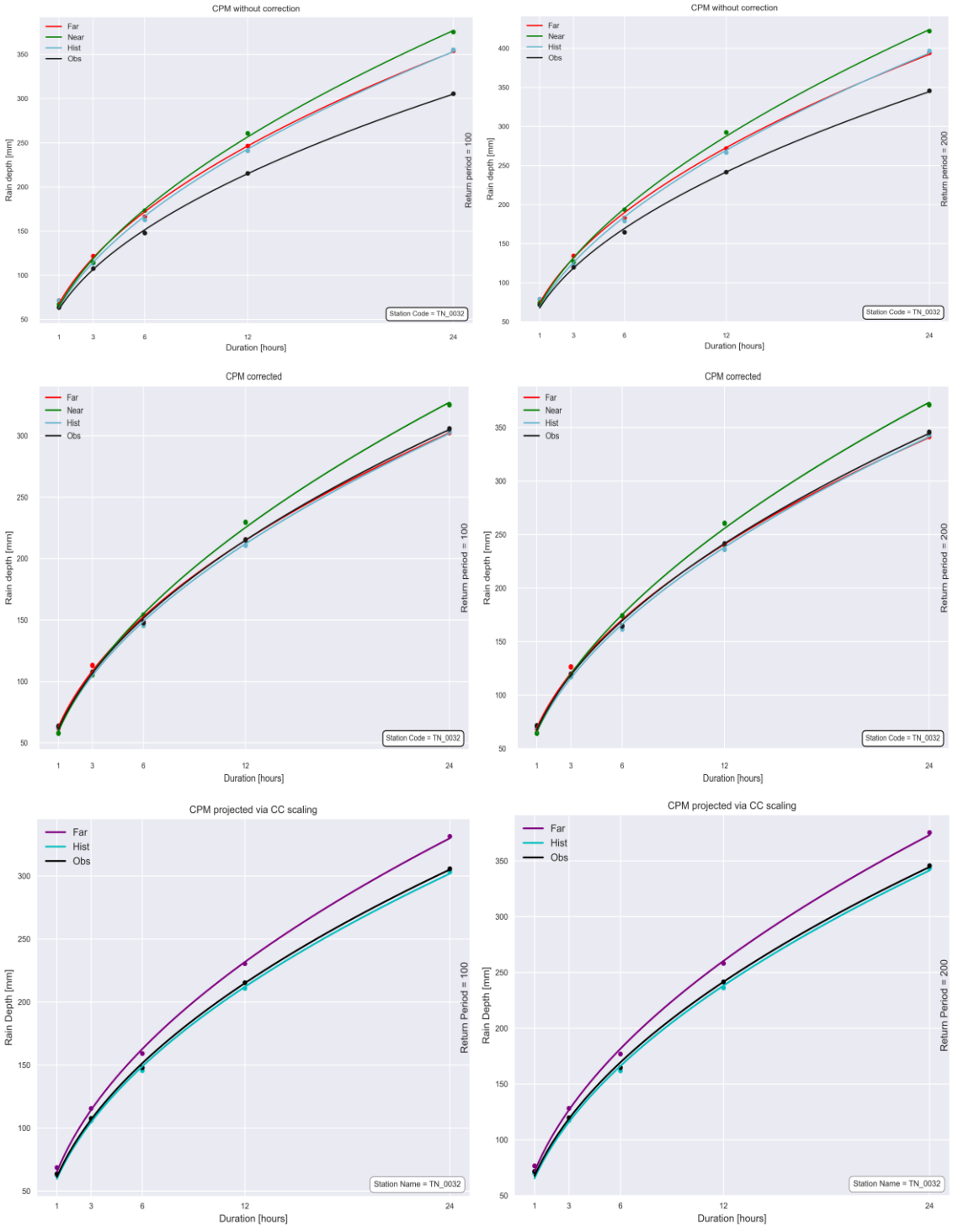

Figure 3-58: DDF curves for station 'TN_0032' for 100 and 200-yr return periods. In the legend 'Far', 'Near', 'Hist' and 'Obs' refers to (2090-2099), (2040-2049), (1996-2005) CPM datasets and observation data respectively. The plots from top to bottom indicate projected DDF curves based on CPMs, CPM biased corrected, and CC scaled respectively.

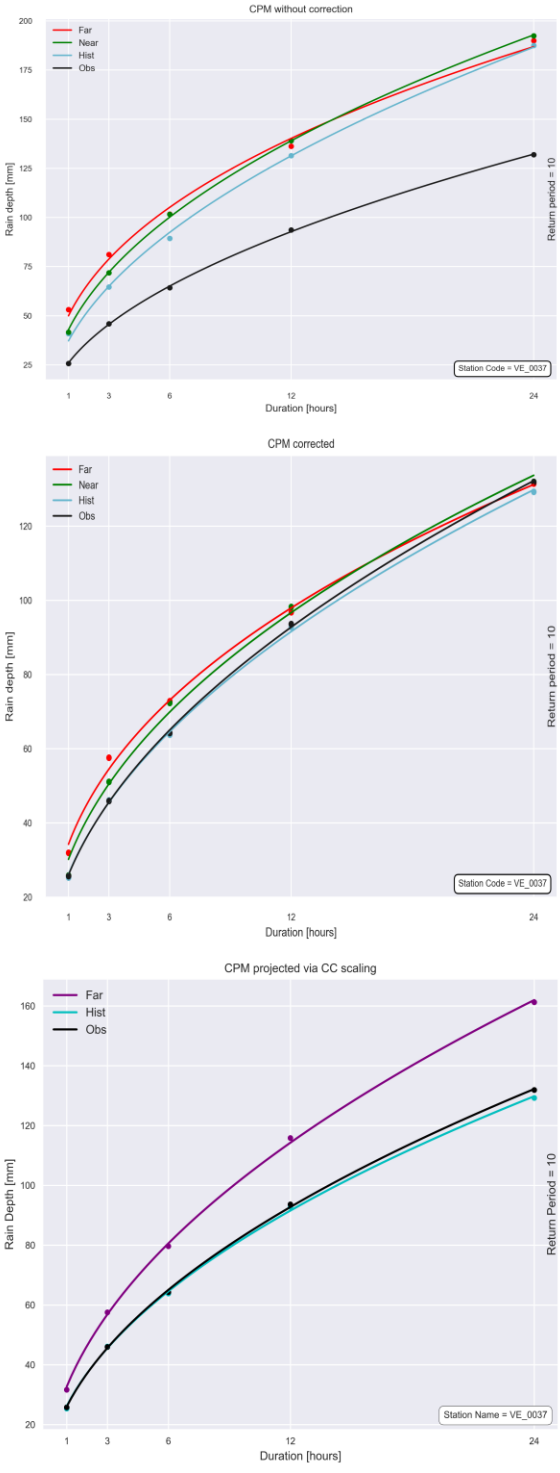

VE_0037: Passo Falzarego

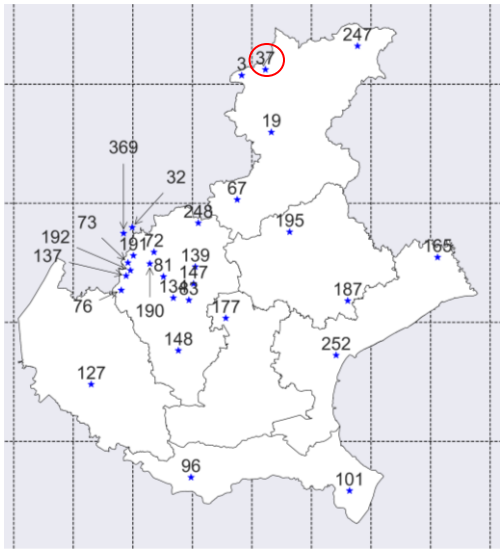

Figure 3-59: DDF curves for station 'VE_0037' for 10-yr return period. In the legend 'Far', 'Near', 'Hist' and 'Obs' refers to (2090-2099), (2040-2049), (1996-2005) CPM datasets and observation data respectively. The plots from top to bottom indicate projected DDF curves based on CPMs, CPM biased corrected, and CC scaled respectively.

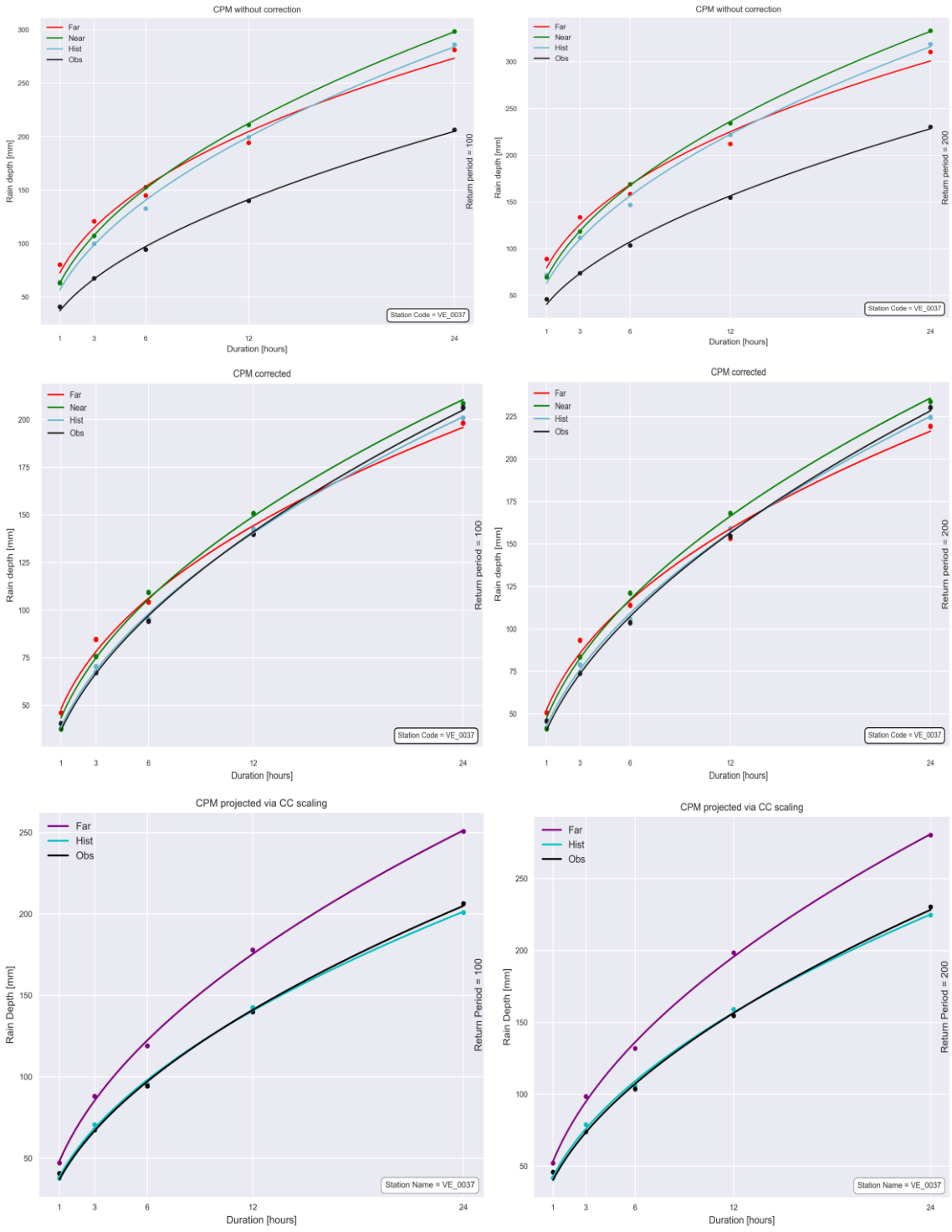

Figure 3-60: DDF curves for station 'VE_0037' for 100 and 200-yr return periods. In the legend 'Far', 'Near', 'Hist' and 'Obs' refers to (2090-2099), (2040-2049), (1996-2005) CPM datasets and observation data respectively. The plots from top to bottom indicate projected DDF curves based on CPMs, CPM biased corrected, and CC scaled respectively.

VE_0139: Lusiana

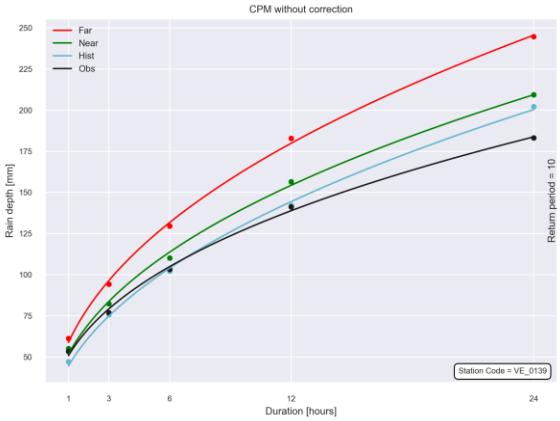

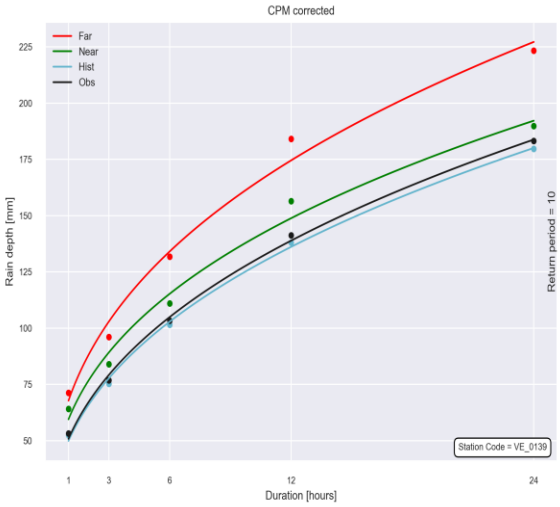

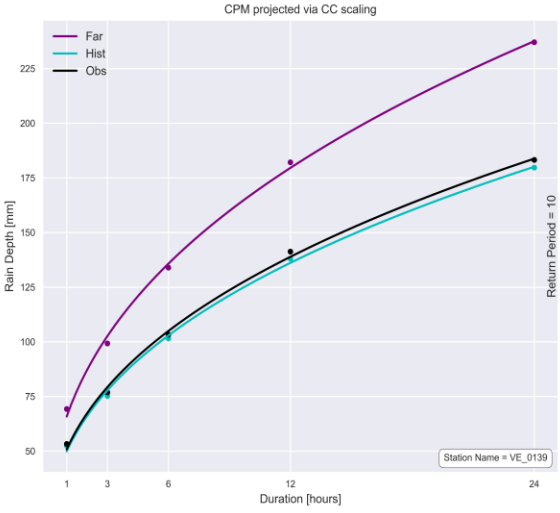

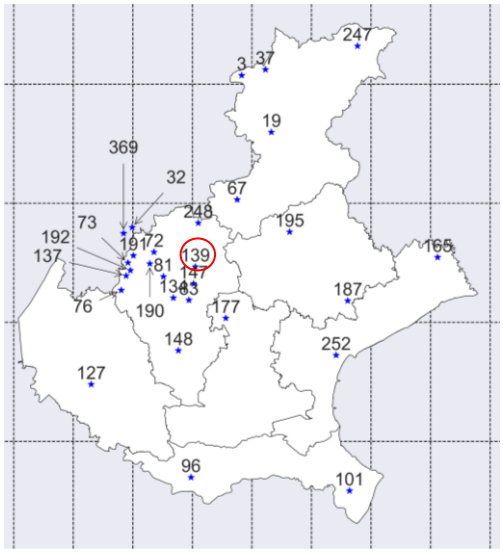

Figure 3-61: DDF curves for station 'VE_0139' for 10-yr return period. In the legend 'Far', 'Near', 'Hist' and 'Obs' refers to (2090-2099), (2040-2049), (1996-2005) CPM datasets and observation data respectively. The plots from top to bottom indicate projected DDF curves based on CPMs, CPM biased corrected, and CC scaled respectively.

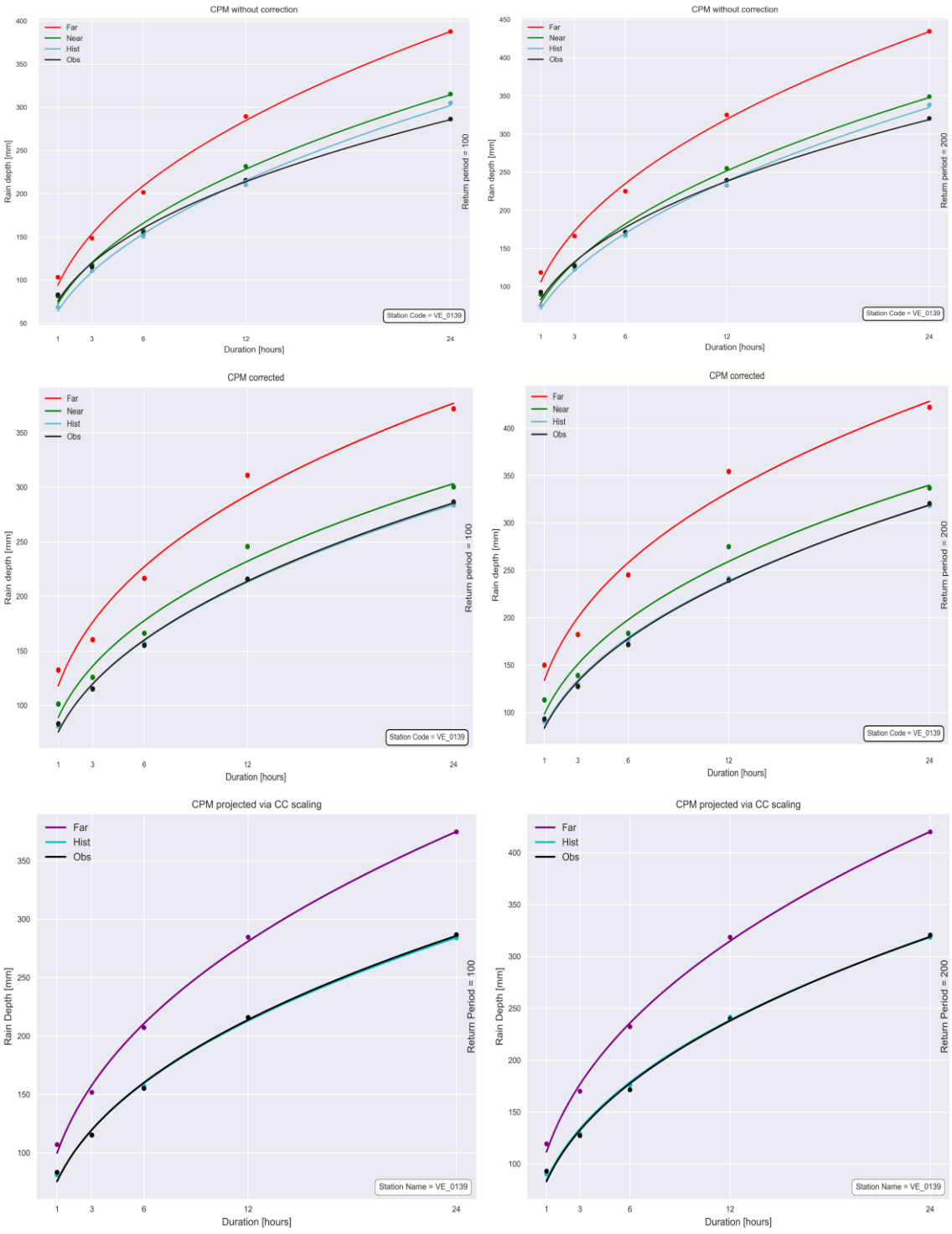

Figure 3-62: DDF curves for station 'VE_0139' for 100 and 200-yr return periods. In the legend 'Far', 'Near', 'Hist' and 'Obs' refers to (2090-2099), (2040-2049), (1996-2005) CPM datasets and observation data respectively. The plots from top to bottom indicate projected DDF curves based on CPMs, CPM biased corrected, and CC scaled respectively.

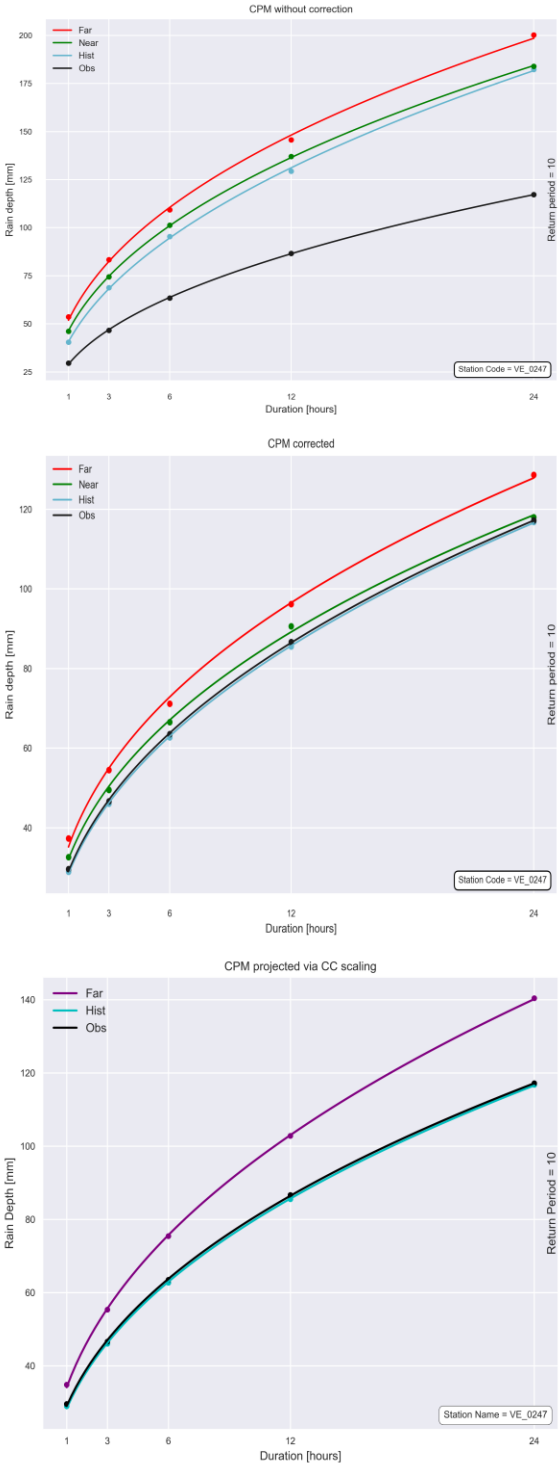

VE_0247: Casamazzagno

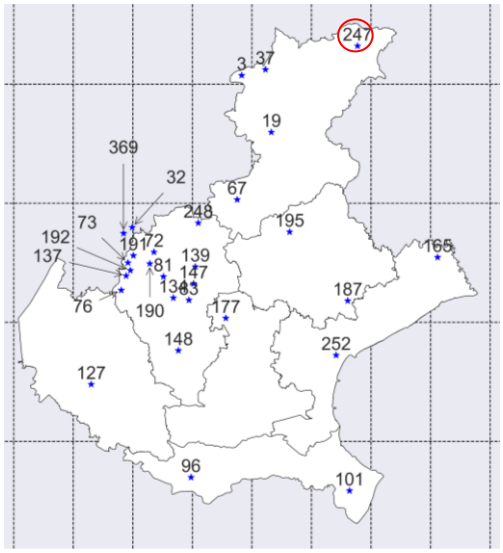

Figure 3-63: DDF curves for station 'VE_0247' for 10-yr return period. In the legend 'Far', 'Near', 'Hist' and 'Obs' refers to (2090-2099), (2040-2049), (1996-2005) CPM datasets and observation data respectively. The plots from top to bottom indicate projected DDF curves based on CPMs, CPM biased corrected, and CC scaled respectively.

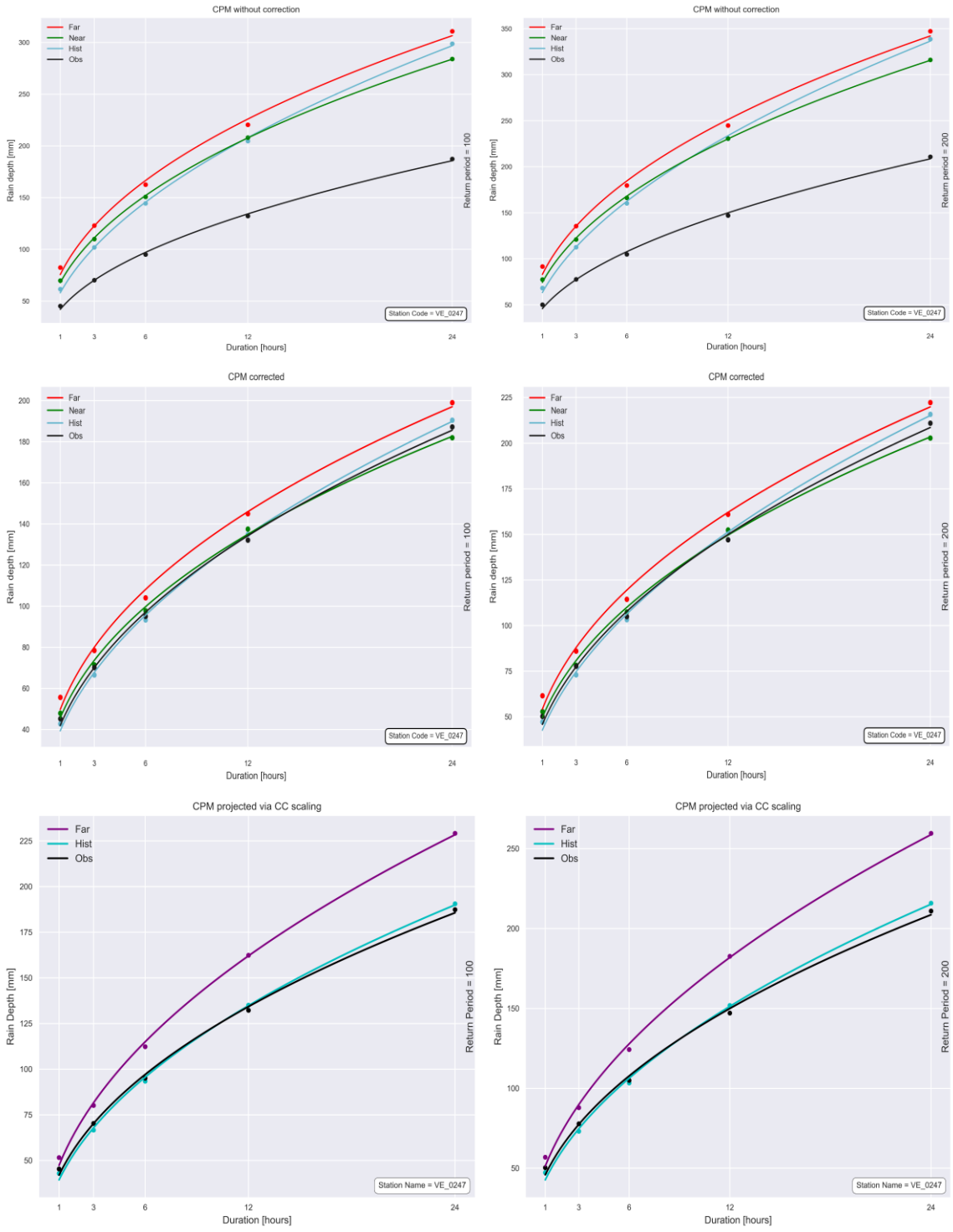

Figure 3-64: DDF curves for station 'VE_0247' for 100 and 200-yr return periods. In the legend 'Far', 'Near', 'Hist' and 'Obs' refers to (2090-2099), (2040-2049), (1996-2005) CPM datasets and observation data respectively. The plots from top to bottom indicate projected DDF curves based on CPMs, CPM biased corrected, and CC scaled respectively.

Chapter 4

4. Discussion and Conclusions

The comprehensive study on rainfall events and their implications, across a plethora of stations and data ranges, offers valuable insights into the characteristics and future trajectories of rainfall. Drawing from the extensive analyses and findings presented in the prior sections, we now discuss the broader implications and conclude the study.

4.1. Observational Insights

Upon examining 29 rain gauge stations, visualized in Figure 2-2, it becomes evident that rainfall patterns exhibit variability across different regions. The data gleaned from these stations underscores the range in average rain intensities: for a 1-hour event, the intensity varies between 3.3 to 6.1 mm/h, and for a 24-hour duration, it lies between 0.4 to 1.0 mm (as shown in Figure 3-1). Moreover, the annual maximum average rain intensities for these stations are between 16.2 to 39.4 mm/h over 1 hour and 2.5 to 6.5 mm over 24 hours (refer to Figure 3-2).

To systematically analyze these rain events, we utilized the Weibull distribution. Following the criteria detailed in section 2.2.2.1 for ordinary events, the data exhibits a variation with the stations recording between 528 to 771 such events (see Figure 3-3). The Probability Weighted Moments (PWM) method was instrumental in estimating the distribution parameters. The scale parameter, essential in determining the intensities, varied from 2.2 to 5.6 mm/h for the 1-hour duration and 0.2 to 0.8 mm/h for 24 hours (referenced in Figure

3-4). In practical terms, a station with a higher scale parameter for its ordinary event distribution implies that it tends to experience higher return levels and vice versa.

The shape parameter of the Weibull distribution is pivotal in understanding the distribution's tail. When the shape parameter is lower, it indicates a heavier tail, suggesting that high-intensity rainfalls might not decrease in probability as quickly as expected. Intriguingly, for all stations and durations considered, the shape parameter was always below 1 (Figure 3-5).

Using a decade-long data record, we estimated the 50-year return levels, aligning with the historical period from 1996 to 2005. For a 1-hour duration, rain intensities varied from 35 to 100 mm/h, and for the 24-hour period, they spanned between 7 to 20 mm/h. A cross-comparison between Figure 3-5 and Figure 3-6 demonstrates a discernible link between return levels and shape parameters. For instance, stations with higher 50-year return levels for the 1-hour duration, such as 127 and 195, exhibited lower shape parameters. In contrast, stations like 3 and 37 which displayed lowest 50-yr return levels had the highest shape parameters.

Figure 3-7 through 9 offer a detailed perspective on the parameter values derived from observational data across varied durations. Concerning the 'N' parameter as depicted in Figure 3-7, its consistency across durations is attributed to the uniform criteria employed for selecting ordinary events. As depicted in Figure 3-8, the scale parameter tends to diminish as durations increase, yet this decline is not uniform for every incremental duration. Still, a consistent trend is observable among all stations. In contrast, the shape parameter manifests a more erratic trend across durations and among different stations. Notably, a majority of stations display lower shape parameters at 1 h and 24 h durations, while indicating elevated values at intervals of 3 and 6 hours as highlighted in Figure 3-9.

4.2. Model Evaluations

4.2.1. Comparison with CPM

The Convection Permitting Model initially showcased a tendency to overestimate in several key areas compared to the observational data. Whether it is the mean rain intensity, annual maximum rain, or parameters of ordinary events distribution, this consistent overestimation highlights the challenges in direct model deployment without bias correction.

In terms of mean rain intensity, Figure 3-10 reveals that the CPM overestimated observations by a significant margin—up to 70% for certain stations like VE_0248. Figure 3-11 further expands on this, suggesting that these biases amplify with duration, leading to greater discrepancies in the CPM's 24-hour predictions compared to its 1-hour forecasts.

Diving into the CPM's biases concerning the mean annual maximum rain intensity, Figure 3-12 elucidates that the model underestimates for half of the stations at a 1-hour duration. This trend, intriguingly, inverts as the duration extends. By the 24-hour mark, the CPM overestimates for every station, as highlighted in Figure 3-13.

Addressing the ordinary event distribution parameters, the CPM consistently overestimates across the three parameters: 'N', scale 'C', and shape 'W'. Figure 3-17 shows an ascending trend of overestimation for the scale parameter 'C' with increasing duration across all stations. The shape parameter 'W' also sees a conspicuous overestimation for most stations, as evidenced by Figure 3-18. Furthermore, Figure 3-19 maps out this overestimation across durations, revealing a non-uniform increase with marked peaks appearing intermittently between 1-hour and 24-hour durations.

When analyzing the 50-year return levels, Figure 3-20 and Figure 3-21 demonstrate the CPM's inclination to underestimate these quantiles. The magnitude of this underestimation, however, fluctuates across durations. A compelling observation arises when aligning the 50-year return levels with the shape parameters: station 'VE_0003', displaying the most pronounced underestimation in the shape parameter (Figure 3-19), presents the most

considerable overestimation in the 50-year return levels. In contrast, station 'VE_0127', with its marked overestimation in the shape parameter, shows the highest underestimation for the 50-year return levels.

4.2.2. Bias Correction

Fortunately, the bias correction using the Quantile Mapping method has notably improved the CPM's alignment with observational data. This correction, applied across multiple parameters, underscores the importance of refining models.

When considering the mean rain intensity, Figure 3-22 illustrated how closely the CPM now matches the observed data. The ratios for every duration and at all stations hover around 1. The bias correction also improved the representation of the mean annual maximum rain in the CPM, effectively diminishing its prior overestimation, as seen in Figure 3-23 and Figure 3-24.

Regarding the parameters for the ordinary events distribution, post-correction findings suggest that the CPM now more faithfully mirrors the reference observational data across all parameters. Figure 3-26 illustrated the improved alignment of the scale parameter with observational data, converging around a value of 1. Similarly, Figure 3-27 underscored the refined correspondence of the shape parameter with observational data when compared with pre-bias correction scenarios.

Moreover, when examining the 50-year return level, the bias correction has significantly bridged the gap between the CPM's overestimation and the observational data, as demonstrated in Figure 3-28 and Figure 3-29.

4.2.3. Temperature and Rainfall

The link between temperature rises and the corresponding change in rain intensities is noteworthy. The majority of the stations indicate an increase in rain intensity in line with increasing temperatures.

Figure 3-48 illustrated the mean temperature difference between CPM historical and CPM far future. The location at Brendola (VE_0148) exhibits the slightest increase in temperature at 0.2℃. Conversely, station location at Passo Sommo (TN_0369) shows the most significant surge, with a 4.8℃ rise. Notably, most locations show temperature rise between 2 to 4℃.

In Figure 3-49 we showed the percent difference in mean rain intensity between the CPM of reference period and the 2090 – 2099 period across all the durations. Location corresponding to VE_0037 indicates the maximum percent difference in mean rain intensity of 31.3 % increase in 1 h duration. While the minimum percentage difference was for station location VE_0067 at 24 h by 3.5 % decrease in the far future scenario. For most of the locations the percent increase in mean rain intensity during the 1 h duration decreases as duration increases toward 24 h. See Figure 5-1 and Figure 5-2 in the Appendix for better visualization of percent difference in mean rain intensity with respect to temperature change.

Regarding mean annual maximum rain intensity, Figure 3-50 represented that station location VE_0247 exhibits the maxim intensity by 50.8% in far future and location VE_0252 has the maximum decrease for the far future scenario by 20.5%. The majority of the locations experience an increase in their mean annual maximum rain by about 20%. For more details see Figure 5-3 and Figure 5-4 in the Appendix.

Figure 3-51 and Figure 3-52 showed the percent difference per degree Celsius for the cases of mean rain intensity and mean annual maximum rain between the reference period and the far future scenario. Regarding the mean rain intensity, model projections suggest that the majority of the station locations will encounter an increase in the range of 2.5 to 10 % per each degree Celsius of warming in the future. With respect to mean annual maximum rain intensity a notable number of locations exhibit a decrease of up to 5% in the future

scenario per degree of warming. While the majority of them have an increase of up to 7% per degree of Celsius warming.

4.3. DDF curves

In the evaluation between the CPMs for the reference period and the far-future scenario, the alterations in projected rainfall quantiles emerge clearly. Based on the projections derived from the CPM, it is anticipated that 1-hour rainfall will see a substantial increase by 2100. Specifically, increases of 33%, 36%, 41%, 44%, 51%, and 57% are projected for return periods of 2, 10, 25, 50, 100, and 200 years, respectively. These findings are detailed further in the Appendix, Figure 5-5 and Figure 5-6 . When considering the bias-corrected CPM, the projected changes are slightly different, expecting to be 29%, 41%, 46%, 54%, 63%, and 66% for the respective return periods, see Figure 5-7 and Figure 5-8 in the Appendix. On the other hand, the projections determined from CC scaling are consistently uniform across all durations and return periods. This is primarily because the same temperature difference and percentage increase in rainfall affect uniformly the future projection for different durations in the method of CC scaling, as referenced in section 2.1.1. Based on this CC scaling methodology, it is predicted that there will be a uniform increase in rainfall of up to 38% across all return periods and durations. The Figure 5-9 and Figure 5-10 in the Appendix offers more detailed visual representations of these percentage changes across various durations and return periods.

Turning to Figure 3-44, the box plots present the coefficients of the Depth-Duration-Frequency (DDF) curves, specifically for the case of biased CPMs. Here, it is evident that in the far-future scenario there is a notable rise in this coefficient when juxtaposed against observations spanning all return periods. Conversely, projections for the near-future scenario denote a decrease. For the CPM of the reference period, the coefficient 'a' seems to be consistently underestimated in comparison to the observational data, across all the return periods. Moving on to Figure 3-45, which focuses on the exponent of the DDF curves, the data suggests that this exponent remains relatively constant, on average, across all return periods when visualizing the far-future scenario. Yet, there is a discrepancy when

comparing the exponents between the CPM of the reference period and observational data: the exponent in the CPM tends to be consistently overestimated for all return periods.

Shifting the focus to bias-corrected CPMs, Figure 3-46 and Figure 3-47 showcase box plots representing the coefficients 'a' and 'b' of the DDF curves for these datasets. Observing the coefficient 'a', it is clear that the bias correction has had a favorable impact. It has enhanced the representation of this coefficient in the CPM for the reference period, more closely aligning it with the outcome of observation when compared to the uncorrected CPM dataset. Further, Figure 3-46 also captures an upward trend of the coefficient 'a' value for the far-future scenario across all return periods. This enhanced alignment between the results derived from observational data and the bias-corrected CPM is further corroborated by Figure 3-47 which represents the exponents of the DDF curves. Additionally, Appendix Figure 5-11 and Figure 5-12 provide a detailed overview of the 'a' and 'b' parameters for the curves derived across all considered return periods for each of the durations. These figures unambiguously show a decline in the 'a' values as duration increases. Moreover, a marked uptick in the 'a' values is evident for future scenarios compared to the reference period. Conversely, the 'b' values indicate that observational data consistently overestimate these parameters when compared to CPMs across all durations. However, the variation in 'b' values across all datasets and durations is relatively minor.

Further insights emerge when considering the DDF curves constructed based on CC scaling. Figure 3-55 underscores that the DDF curve coefficient exhibits its highest values in the far-future projections based on this CC scaling method. This is in contrast to the CPM projections for the same far-future scenario. Moreover, the CC scaling method seems to considerably overestimate the value of the exponent of the DDF curve in comparison to other datasets.

Concluding with the overarching observations from the Depth-Duration-Frequency curves: when these are formulated on the basis of CC scaling, it suggests a potential trend of the future projections erring on the side of overestimation in terms of rain intensities, specifically across different return periods. This is a clear indication that while the trend suggesting an increase in future rainfalls is probably on the mark, there is a definite need to refine the exact magnitudes through further nuanced adjustments.

4.4. Conclusions

The challenges posed by climate change have been underscored in this study. The wide-ranging changes projected in rainfall patterns, particularly in Northern Italy, signify the need for a shift in our infrastructural and preparedness strategies.

From our in-depth observational analysis, the pronounced variability in rainfall patterns across different regions became evident. This realization serves as a clear testament to the inadequacy of one-size-fits-all policies. Instead, there is a pressing need to tailor strategies that cater to the distinct weather extremities of individual regions.

Our use of the MEVD approach to examine rainfall events has been particularly enlightening. Its ability to maximize data utility, especially when grappling with limited dataset values, underscores its suitability in analyzing rainfall events in intricate scenarios. The identification of the shape and scale parameters provides a crucial understanding of the expected rain intensities, which is essential for designing flood mitigation strategies.

The CPMs, even though advanced, still showcased biases when compared to observational data. This emphasizes the need for continuous refinement of modeling strategies to ensure their relevance and accuracy. The bias correction using the Quantile Mapping method has notably bridged the gap between CPM predictions and observed data, underlining its importance in climate studies.

Moreover, CPMs provide compelling evidence of significant alterations in rainfall patterns by the year 2100. The projections indicate a substantial increase in 1-hour rainfall across a range of return periods, with bias-corrected CPMs forecasting even greater changes. While the coefficient 'a' tends to be underestimated in the reference period CPM, bias correction improves its alignment with observational data. Concerning the parameters of DDF curves, the coefficient 'a' shows a rising trend with increasing return periods but exhibits a decline with increasing durations. In contrast, the exponent 'b' demonstrates only minor variations across both return periods and durations for all the datsets.

The clear association between temperature rises and changing rain intensities is alarming. With temperature rises being a global concern, the findings from Northern Italy could be

reflective of larger, worldwide patterns. This potentially indicates more intense and frequent rainfall events in many regions as global warming progresses.

Furthermore, the DDF curves constructed based on CC scaling and CPMs present varying outcomes. As discussed in previous section the DDF curves based on CC scaling anticipate an increase of 38% across all return periods for future scenario. On the other hand, the DDFs based on CPMs exhibit an increasing trend in quantiles with return periods, marking an increase of 66% for 1 h rainfall with 200 return time. This signifies that while the Clausius-Clapeyron relation might provide a fundamental understanding of temperature and precipitation relationships, its direct application might lead to discrepancies when assessing rainfall extremes. In light of this, CPMs emerge as central tools, aiding in refining the CC scaling method, especially considering the shorter and less frequent rainfall events.

In conclusion, as we advance into an era characterized by rapid climatic changes, studies like these offer valuable foresight. It is paramount that such insights inform policy-making and infrastructural development, ensuring that our societies remain resilient in the face of the changing nature of rainfall events. For regions like Northern Italy, where changing rainfall patterns could significantly impact urban regions, agriculture, and water resources, addressing these findings is not merely academic but a requirement for sustainable development and preparedness.

Chapter 5

5. Appendix

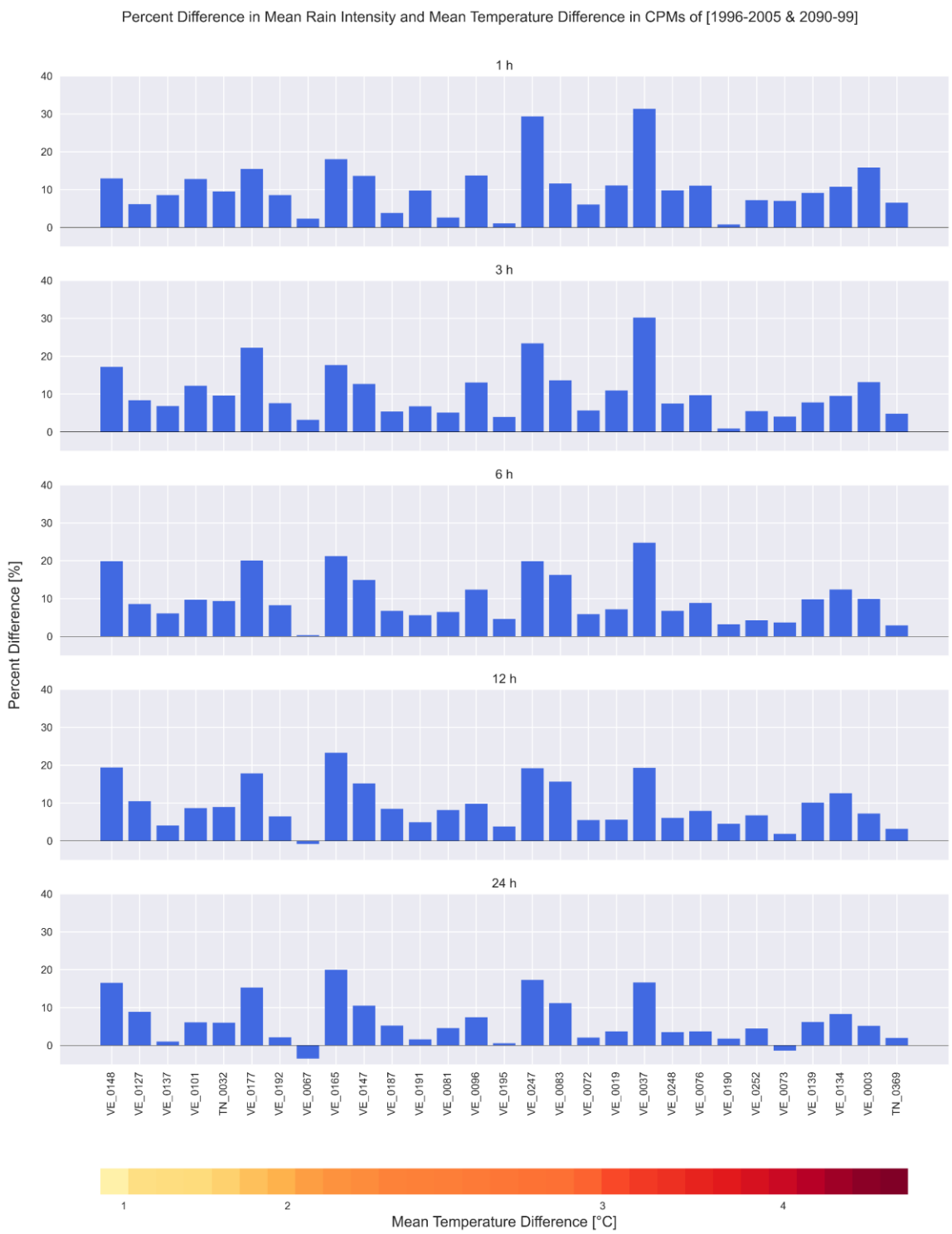

Figure 5-1: Histograms of percent change in mean rain intensity and mean temperature of CPM (1996-2005) and CPM (2090-2099) for all the stations.

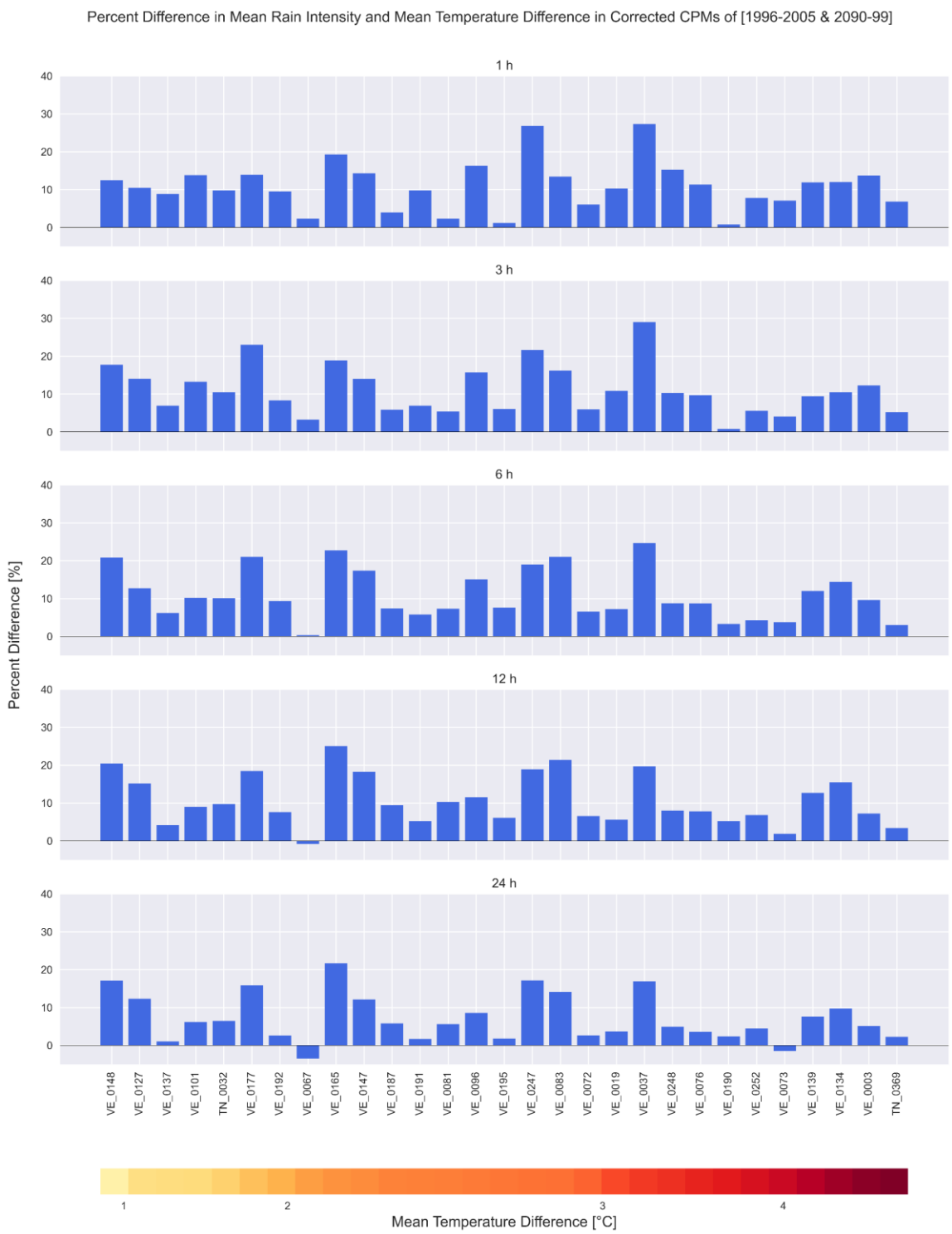

Figure 5-2: Histograms of percent change in mean rain intensity and mean temperature of bias corrected CPMs (1996-2005) and (2090-2099) for all the stations.

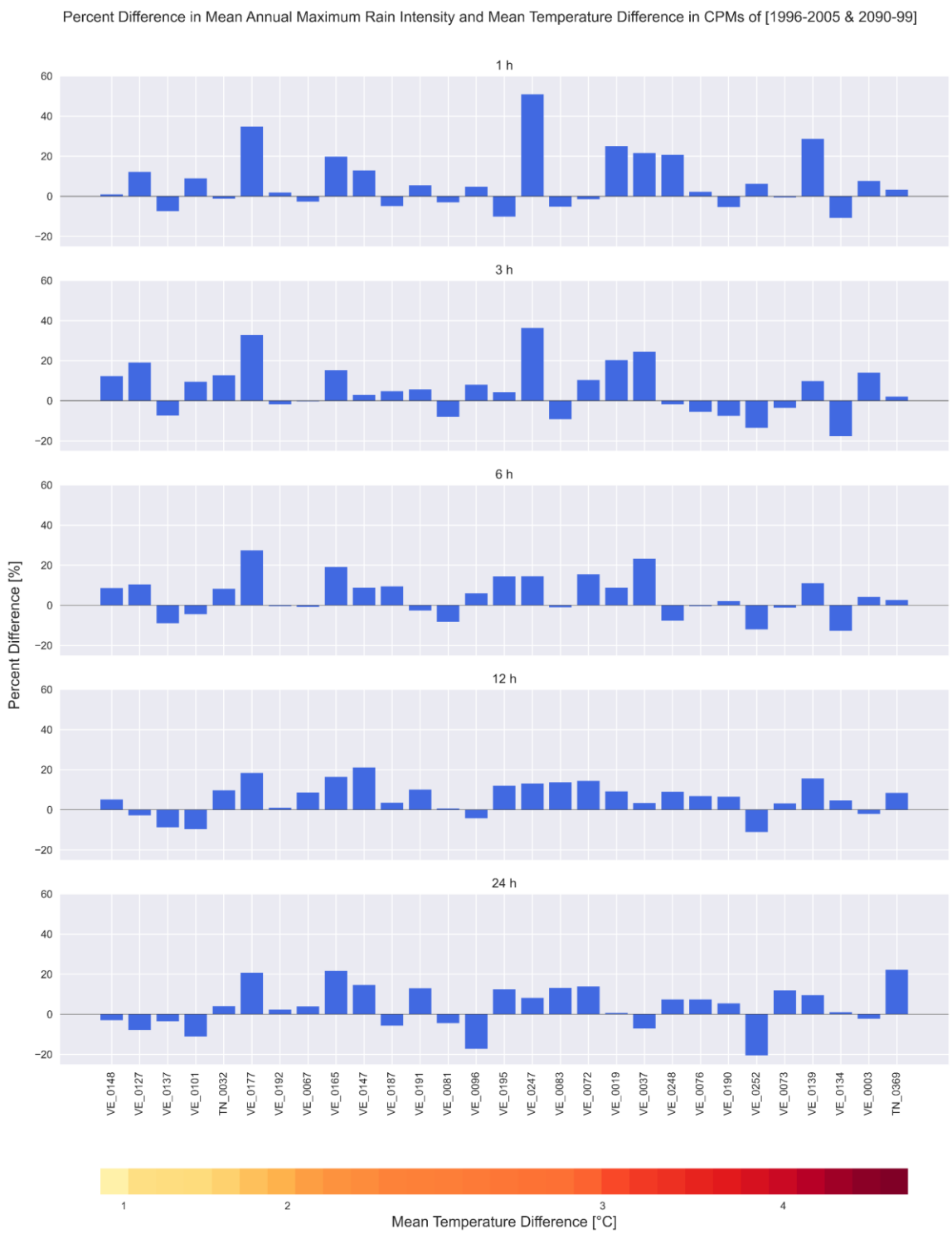

Figure 5-3: Histograms of percent change in mean annual maximum rain intensity and mean temperature of CPMs (1996-2005) and (2090-2099) for all the stations.

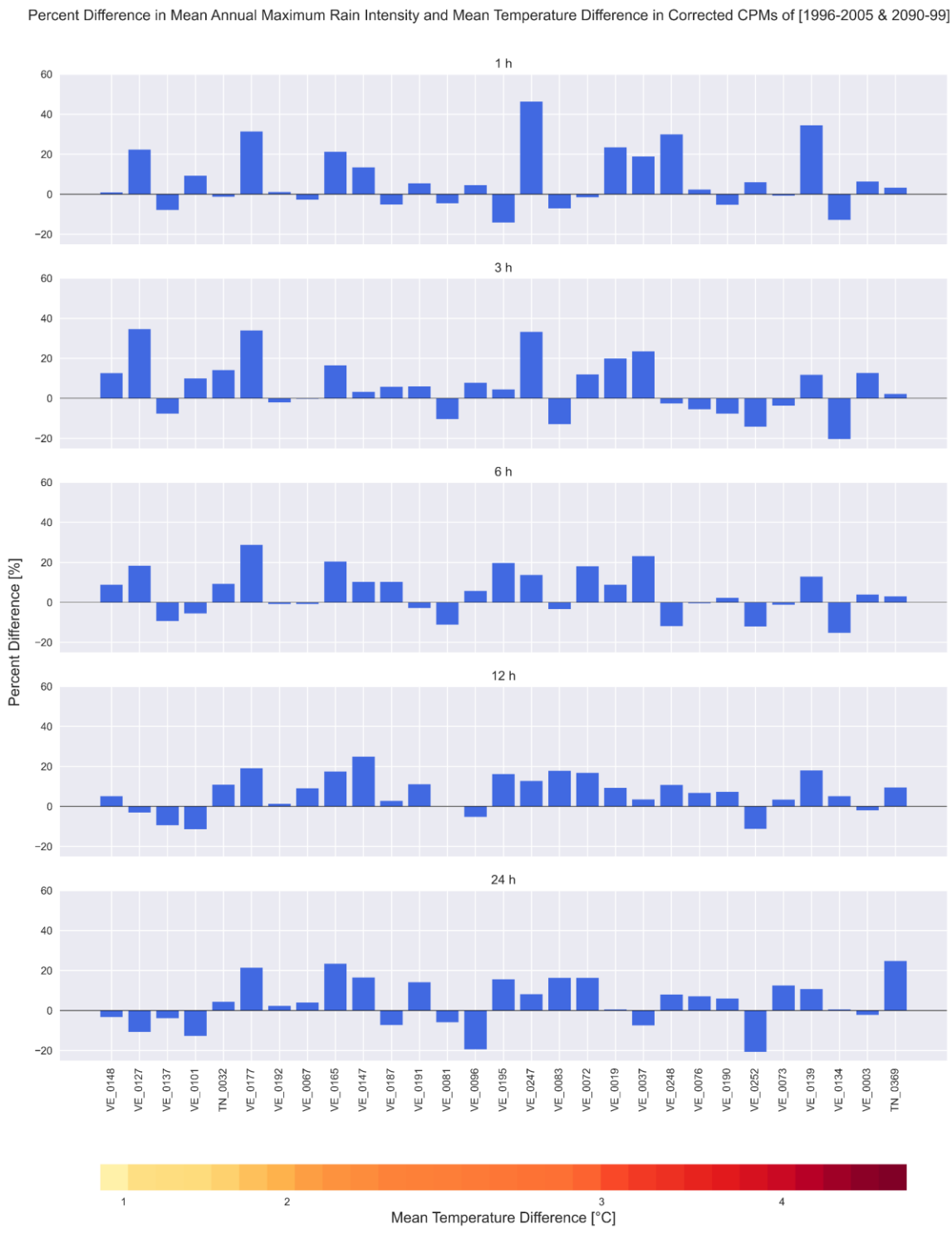

Figure 5-4: Histograms of percent change in mean annual maximum rain intensity and mean temperature of bias corrected CPMs (1996-2005) and (2090-2099) for all the stations.

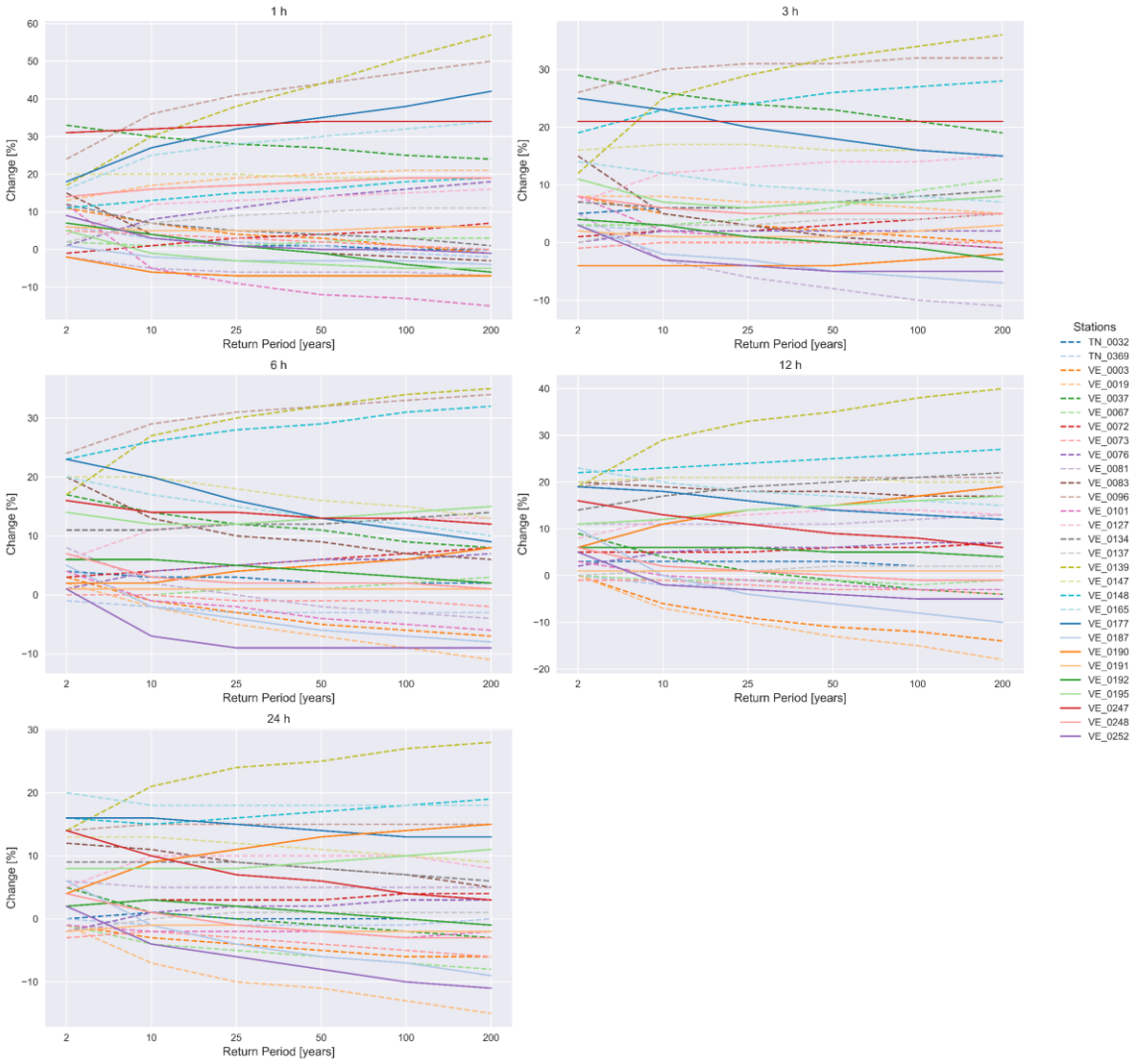

Figure 5-5: Plots of percent change in quantiles of DDFs in CPMs of (1996-2005) and far future scenario (2090-2099) across all return periods for all durations.

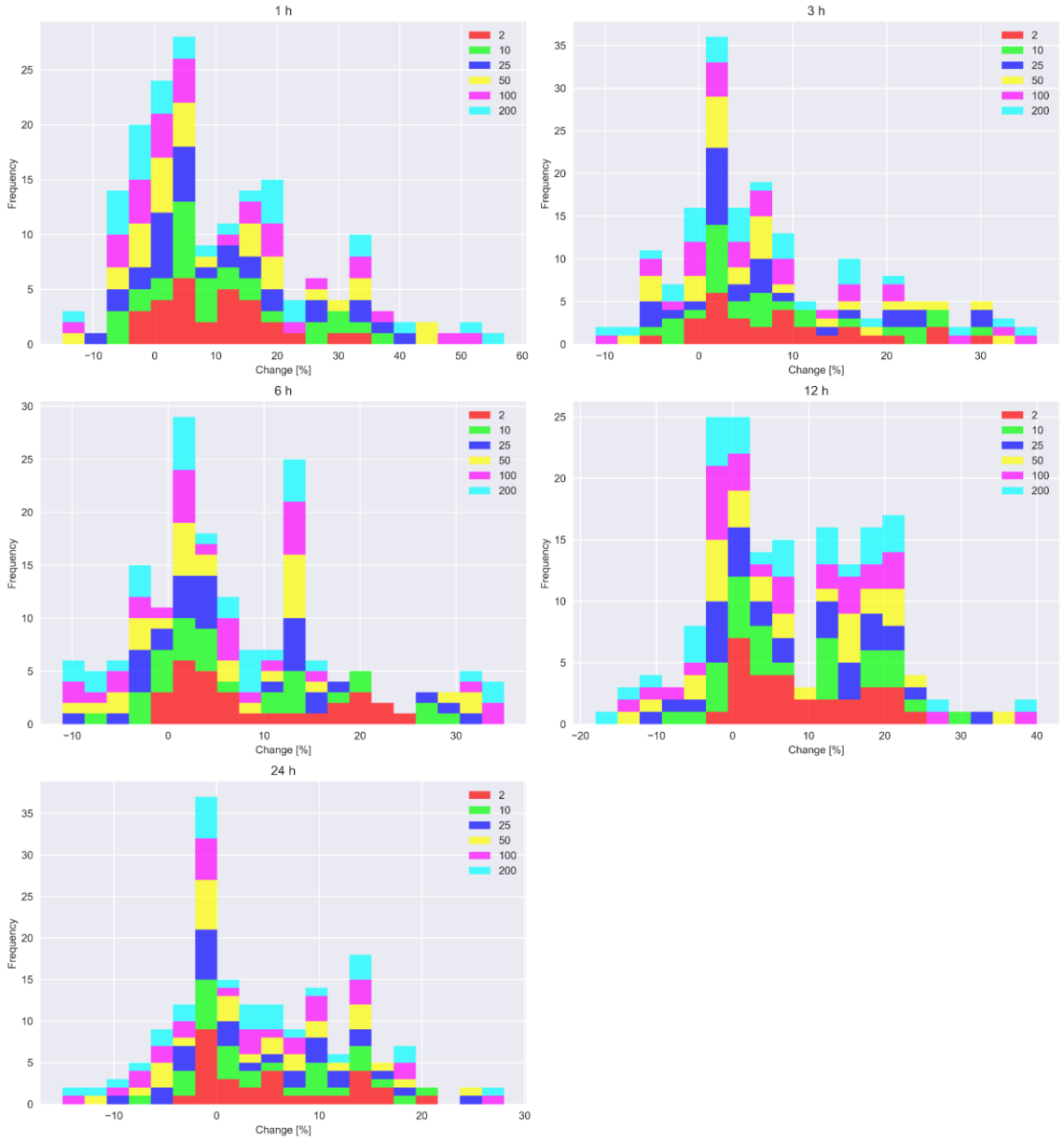

Figure 5-6: Histograms of percent change in quantiles of DDFs in CPMs of (1996-2005) and far future scenario (2090-2099) for all durations. Each color denotes a return period indicated in the legend of each figure.

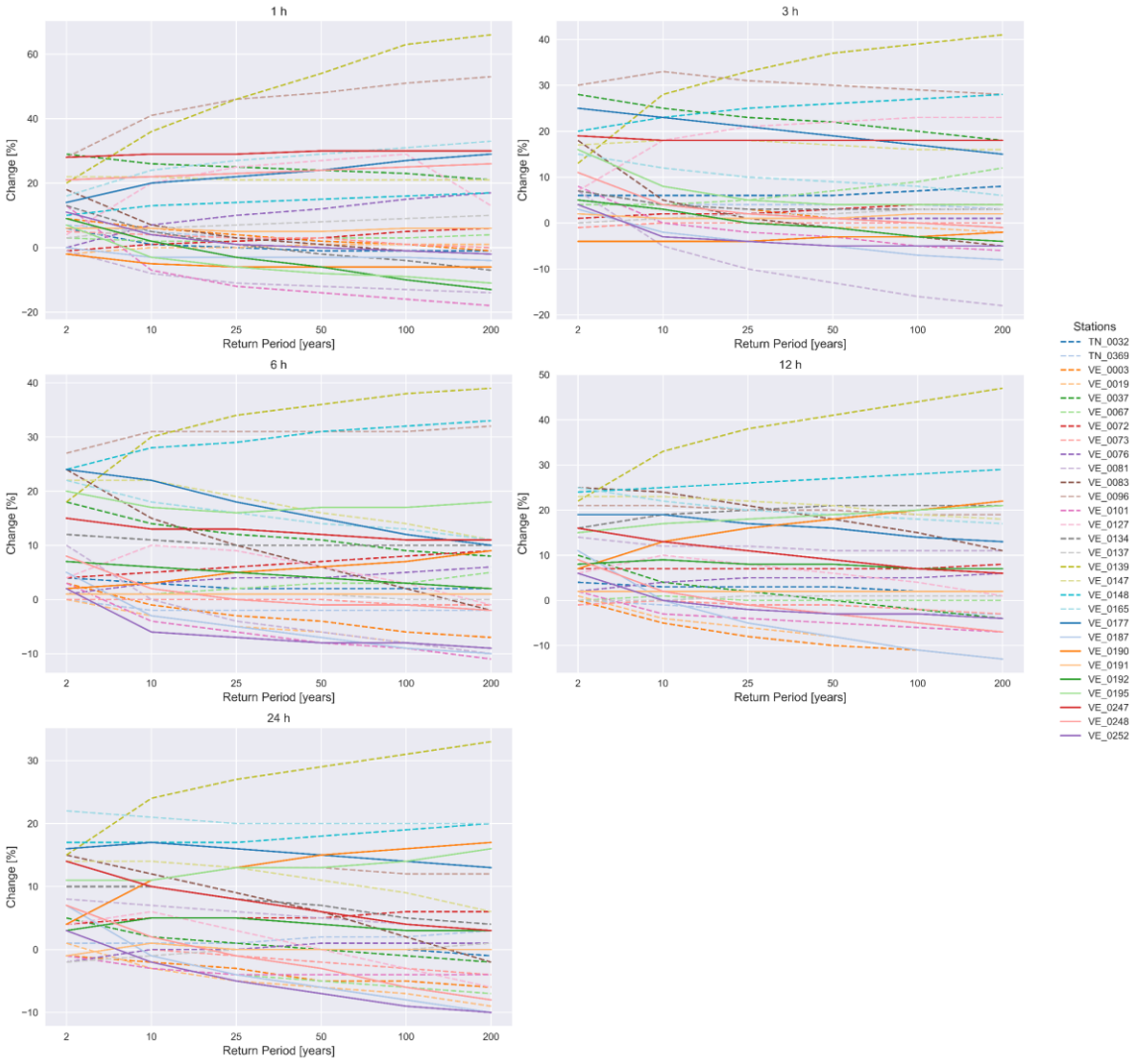

Figure 5-7: Plots of percent change in quantiles of DDFs in bias corrected CPMs of (1996-2005) and far future scenario (2090-2099) across all return periods for all durations.

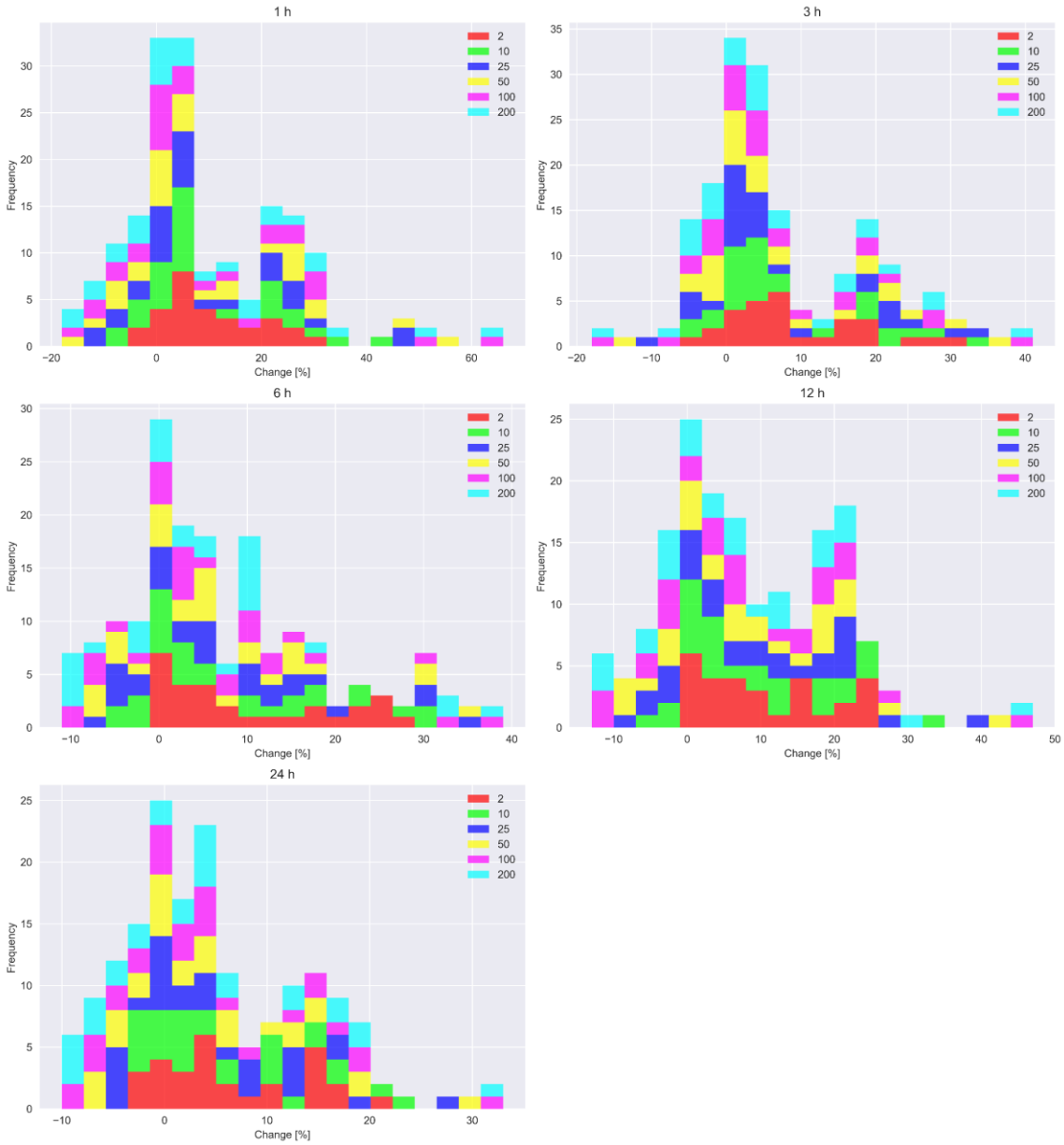

Figure 5-8: Histograms of percent change in quantiles of DDFs in bias corrected CPMs of (1996-2005) and far future scenario (2090-2099) for all durations. Each color denotes a return period indicated in the legend of each figure.

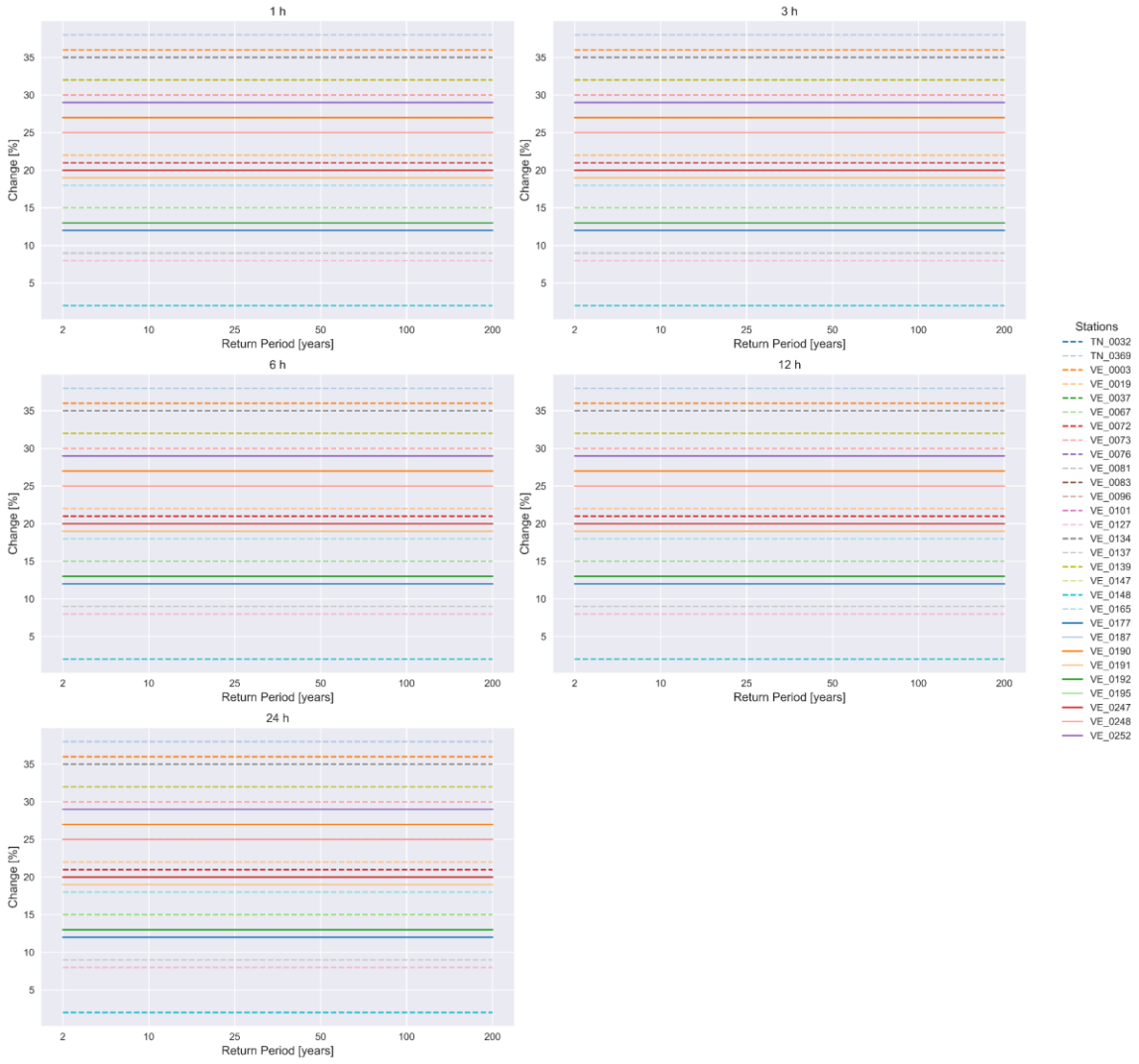

Figure 5-9: Plots of percent change in quantiles of DDFs in bias corrected CPM of (1996-2005) and CC scaled far future projection (2090-2099) across all return periods for all durations.

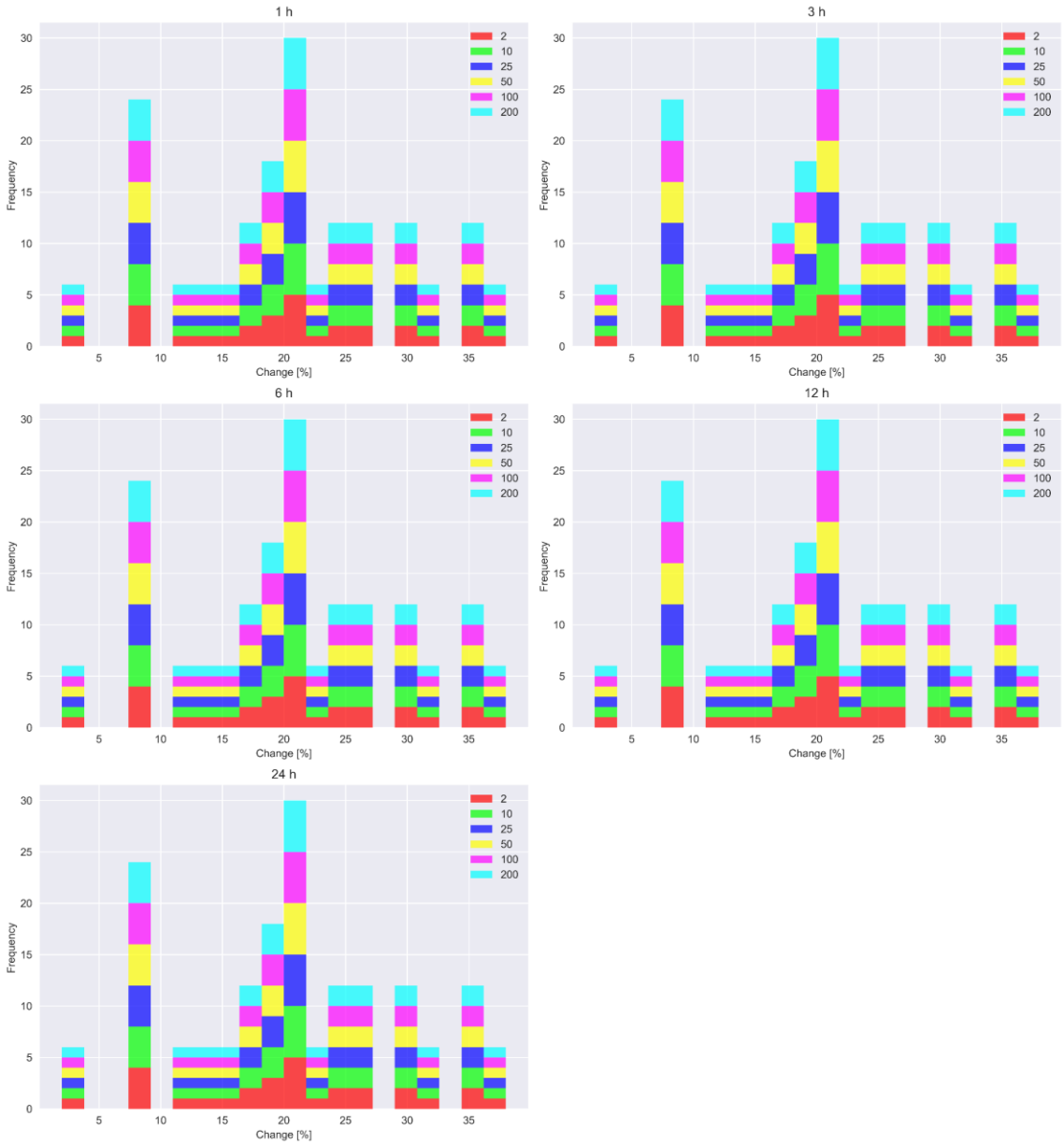

Figure 5-10: Histograms of percent change in quantiles of DDFs in bias corrected CPMs of (1996-2005) and CC scaled far future projection (2090-2099) for all durations. Each color denotes a return period indicated in the legend of each figure.

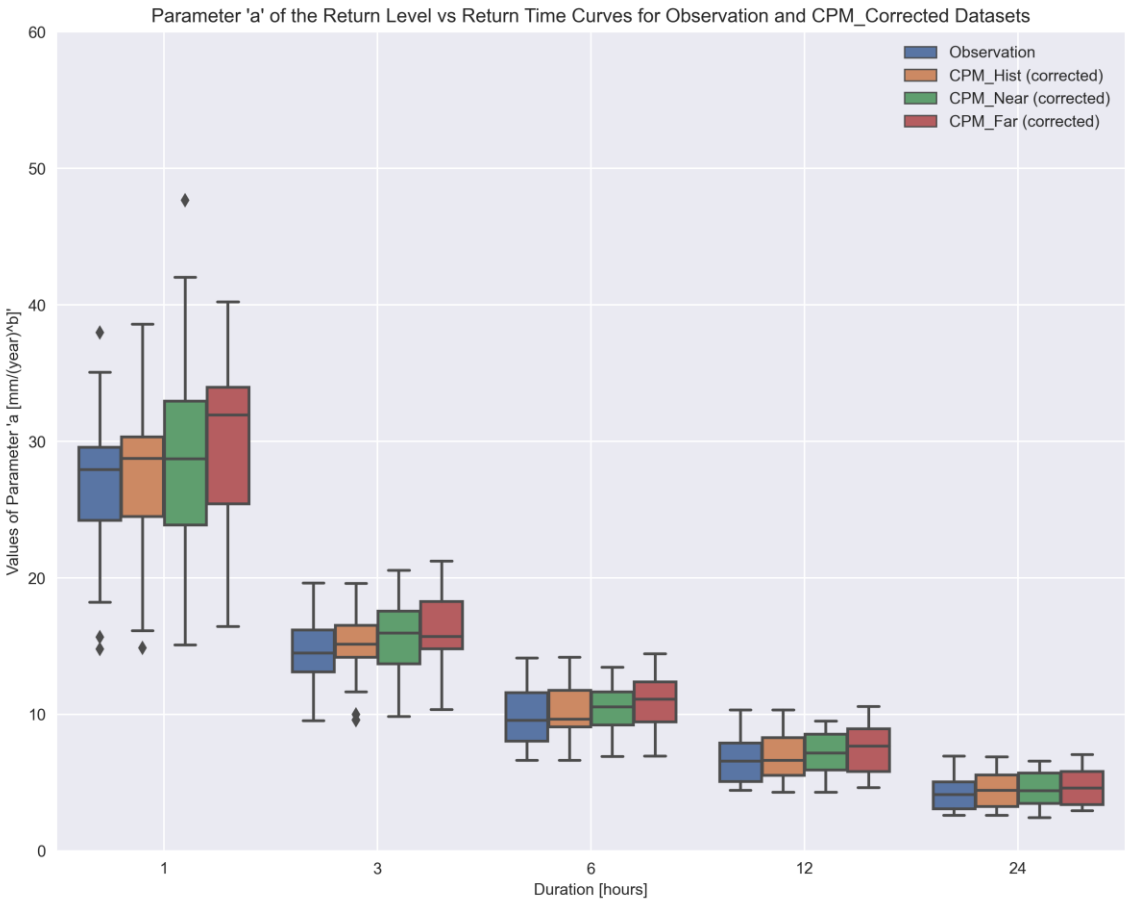

Figure 5-11: This figure shows the value of 'a' parameter when the DDFs quantiles are represented across all return periods for each rainfall duration. Here CPM_Hist, CPM_Near, CPM_Far (corrected) refer to the bias corrected CPM datasets respectively for historical period, near future and far future scenarios.

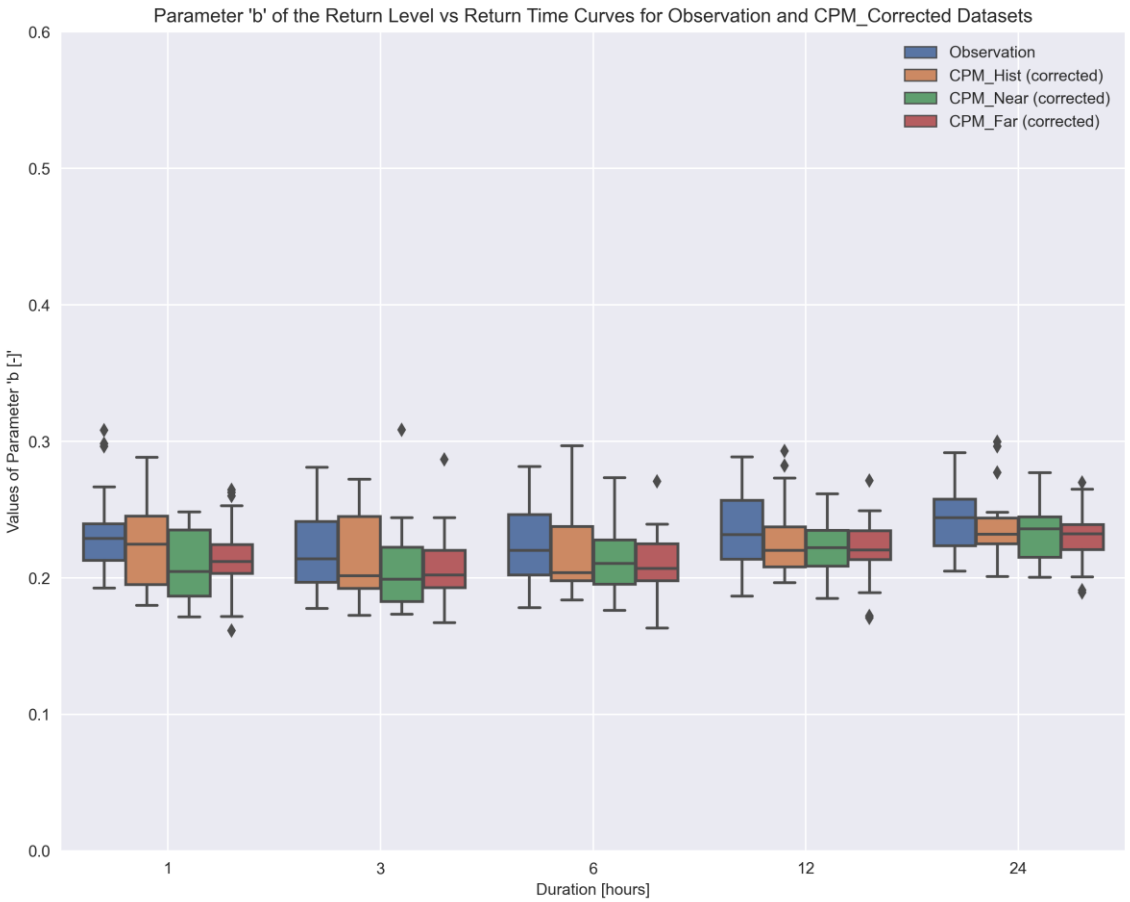

Figure 5-12: This figure shows the value of 'b' parameter when the DDFs quantiles are represented across all return periods for each rainfall duration. Here CPM_Hist, CPM_Near, CPM_Far (corrected) refer to the bias corrected CPM datasets respectively for historical period, near future and far future scenarios.

Chapter 6

6. References

Argüeso, D., Evans, J. P., & Fita, L. (2013). Precipitation bias correction of very high resolution regional climate models. *Hydrology and Earth System Sciences*, *17*(11), 4379–4388. https://doi.org/10.5194/hess-17-4379-2013

Arnbjerg-Nielsen, K., Willems, P., Olsson, J., Beecham, S., Pathirana, A., Bülow Gregersen, I., Madsen, H., & Nguyen, V.-T.-V. (2013). Impacts of climate change on rainfall extremes and urban drainage systems: A review. *Water Science and Technology*, *68*(1), 16–28. https://doi.org/10.2166/wst.2013.251

Balkema, A. A., & De Haan, L. (1974). Residual Life Time at Great Age. *The Annals of Probability*, *2*(5). https://doi.org/10.1214/aop/1176996548

Ban, N., Rajczak, J., Schmidli, J., & Schär, C. (2020). Analysis of Alpine precipitation extremes using generalized extreme value theory in convection-resolving climate simulations. *Climate Dynamics*, *55*(1–2), 61–75. https://doi.org/10.1007/s00382-018-4339-4

Ban, N., Schmidli, J., & Schär, C. (2014). Evaluation of the convection-resolving regional climate modeling approach in decade-long simulations. *Journal of Geophysical Research: Atmospheres*, *119*(13), 7889–7907. https://doi.org/10.1002/2014JD021478

Ban, N., Schmidli, J., & Schär, C. (2015). Heavy precipitation in a changing climate: Does short-term summer precipitation increase faster? *Geophysical Research Letters*, *42*(4), 1165–1172. https://doi.org/10.1002/2014GL062588

Bao, J., Sherwood, S. C., Alexander, L. V., & Evans, J. P. (2017). Future increases in extreme precipitation exceed observed scaling rates. *Nature Climate Change*, *7*(2), 128–132. https://doi.org/10.1038/nclimate3201

Barlage, M., Chen, F., Rasmussen, R., Zhang, Z., & Miguez-Macho, G. (2021). The Importance of Scale-Dependent Groundwater Processes in Land-Atmosphere Interactions Over the Central United States. *Geophysical Research Letters*, *48*(5). https://doi.org/10.1029/2020GL092171

Berg, P., Christensen, O. B., Klehmet, K., Lenderink, G., Olsson, J., Teichmann, C., & Yang, W. (2019). Summertime precipitation extremes in a EURO-CORDEX 0.11° ensemble at an hourly resolution. *Natural Hazards and Earth System Sciences*, *19*(4), 957–971. https://doi.org/10.5194/nhess-19-957-2019

Berg, P., & Haerter, J. O. (2013). Unexpected increase in precipitation intensity with temperature—A result of mixing of precipitation types? *Atmospheric Research*, *119*, 56–61. https://doi.org/10.1016/j.atmosres.2011.05.012

Berthou, S., Kendon, E. J., Chan, S. C., Ban, N., Leutwyler, D., Schär, C., & Fosser, G. (2020). Pan-European climate at convection-permitting scale: A model intercomparison study. *Climate Dynamics*, *55*(1–2), 35–59. https://doi.org/10.1007/s00382-018-4114-6

Cannon, A. J. (2008). Probabilistic Multisite Precipitation Downscaling by an Expanded Bernoulli–Gamma Density Network. *Journal of Hydrometeorology*, *9*(6), 1284–1300. https://doi.org/10.1175/2008JHM960.1

Chen, G., Ming, Y., Singer, N. D., & Lu, J. (2011). Testing the Clausius-Clapeyron constraint on the aerosol-induced changes in mean and extreme precipitation: AEROSOL-INDUCED PRECIPITATION CHANGES. *Geophysical Research Letters*, *38*(4), n/a-n/a. https://doi.org/10.1029/2010GL046435

Cheng, L., & AghaKouchak, A. (2014). Nonstationary Precipitation Intensity-Duration-Frequency Curves for Infrastructure Design in a Changing Climate. *Scientific Reports*, *4*(1), 7093. https://doi.org/10.1038/srep07093

Coles, S. (2001). *An Introduction to Statistical Modeling of Extreme Values*. Springer London. https://doi.org/10.1007/978-1-4471-3675-0

Coppola, E., Sobolowski, S., Pichelli, E., Raffaele, F., Ahrens, B., Anders, I., Ban, N., Bastin, S., Belda, M., Belusic, D., Caldas-Alvarez, A., Cardoso, R. M., Davolio, S., Dobler, A., Fernandez, J., Fita, L., Fumiere, Q., Giorgi, F., Goergen, K., … Warrach-Sagi, K. (2020). A first-of-its-kind multi-model convection permitting ensemble for investigating convective phenomena over Europe and the Mediterranean. *Climate Dynamics*, *55*(1–2), 3–34. https://doi.org/10.1007/s00382-018-4521-8

Dai, A., Rasmussen, R. M., Liu, C., Ikeda, K., & Prein, A. F. (2020). A new mechanism for warm-season precipitation response to globalwarming based on convection-permitting simulations. *Climate Dynamics*, *55*(1–2), 343–368. https://doi.org/10.1007/s00382-017-3787-6

Dallan, E., Borga, M., Zaramella, M., & Marra, F. (2022). Enhanced Summer Convection Explains Observed Trends in Extreme Subdaily Precipitation in the Eastern Italian Alps. *Geophysical Research Letters*, *49*(5). https://doi.org/10.1029/2021GL096727

Davison, A. C., & Smith, R. L. (1990). Models for Exceedances over High Thresholds. *Journal of the Royal Statistical Society. Series B (Methodological)*, *52*(3), 393–442.

De Michele, C. (2003). A Generalized Pareto intensity-duration model of storm rainfall exploiting 2-Copulas. *Journal of Geophysical Research*, *108*(D2), 4067. https://doi.org/10.1029/2002JD002534

Donat, M. G., Lowry, A. L., Alexander, L. V., O'Gorman, P. A., & Maher, N. (2016). More extreme precipitation in the world's dry and wet regions. *Nature Climate Change*, *6*(5), 508–513. https://doi.org/10.1038/nclimate2941

Drobinski, P., Alonzo, B., Bastin, S., Silva, N. D., & Muller, C. (2016). Scaling of precipitation extremes with temperature in the French Mediterranean region: What explains the hook shape? *Journal of Geophysical Research: Atmospheres*, *121*(7), 3100–3119. https://doi.org/10.1002/2015JD023497

Drobinski, P., Silva, N. D., Panthou, G., Bastin, S., Muller, C., Ahrens, B., Borga, M., Conte, D., Fosser, G., Giorgi, F., Güttler, I., Kotroni, V., Li, L., Morin, E., Önol, B., Quintana-Segui, P., Romera, R., & Torma, C. Z. (2018). Scaling precipitation extremes with temperature in the Mediterranean: Past climate assessment and projection in anthropogenic scenarios. *Climate Dynamics*, *51*(3), 1237–1257. https://doi.org/10.1007/s00382-016-3083-x

Fischer, E. M., & Knutti, R. (2015). Anthropogenic contribution to global occurrence of heavy-precipitation and high-temperature extremes. *Nature Climate Change*, *5*(6), 560–564. https://doi.org/10.1038/nclimate2617

Fischer, E. M., Sedláček, J., Hawkins, E., & Knutti, R. (2014). Models agree on forced response pattern of precipitation and temperature extremes. *Geophysical Research Letters*, *41*(23), 8554–8562. https://doi.org/10.1002/2014GL062018

Fisher, R. A., & Tippett, L. H. C. (1928). Limiting forms of the frequency distribution of the largest or smallest member of a sample. *Mathematical Proceedings of the Cambridge Philosophical Society*, *24*(2), 180–190. https://doi.org/10.1017/S0305004100015681

Formetta, G., Marra, F., Dallan, E., Zaramella, M., & Borga, M. (2022). Differential orographic impact on sub-hourly, hourly, and daily extreme precipitation. *Advances in Water Resources*, *159*, 104085. https://doi.org/10.1016/j.advwatres.2021.104085

Fosser, G., Kendon, E. J., Stephenson, D., & Tucker, S. (2020). Convection-Permitting Models Offer Promise of More Certain Extreme Rainfall Projections. *Geophysical Research Letters*, *47*(13). https://doi.org/10.1029/2020GL088151

Fosser, G., Khodayar, S., & Berg, P. (2015). Benefit of convection permitting climate model simulations in the representation of convective precipitation. *Climate Dynamics*, *44*(1–2), 45–60. https://doi.org/10.1007/s00382-014-2242-1

Fowler, H. J., Ali, H., Allan, R. P., Ban, N., Barbero, R., Berg, P., Blenkinsop, S., Cabi, N. S., Chan, S., Dale, M., Dunn, R. J. H., Ekström, M., Evans, J. P., Fosser, G., Golding, B., Guerreiro, S. B., Hegerl, G. C., Kahraman, A., Kendon, E. J., …

Whitford, A. (2021). Towards advancing scientific knowledge of climate change impacts on short-duration rainfall extremes. *Philosophical Transactions of the Royal Society A: Mathematical, Physical and Engineering Sciences*, *379*(2195), 20190542. https://doi.org/10.1098/rsta.2019.0542

Fowler, H. J., Wasko, C., & Prein, A. F. (2021). Intensification of short-duration rainfall extremes and implications for flood risk: Current state of the art and future directions. *Philosophical Transactions of the Royal Society A: Mathematical, Physical and Engineering Sciences*, *379*(2195), 20190541. https://doi.org/10.1098/rsta.2019.0541

Gençay, R., & Selçuk, F. (2004). Extreme value theory and Value-at-Risk: Relative performance in emerging markets. *International Journal of Forecasting*, *20*(2), 287–303. https://doi.org/10.1016/j.ijforecast.2003.09.005

Grimshaw, S. D. (1993). Computing Maximum Likelihood Estimates for the Generalized Pareto Distribution. *Technometrics*, *35*(2), 185–191. https://doi.org/10.1080/00401706.1993.10485040

Gudmundsson, L., Bremnes, J. B., Haugen, J. E., & Engen-Skaugen, T. (2012). Technical Note: Downscaling RCM precipitation to the station scale using statistical transformations – a comparison of methods. *Hydrology and Earth System Sciences*, *16*(9), 3383–3390. https://doi.org/10.5194/hess-16-3383-2012

Gumbel, E. J. (1958). *Statistics of Extremes*. Columbia University Press. https://doi.org/10.7312/gumb92958

Hardwick Jones, R., Westra, S., & Sharma, A. (2010). Observed relationships between extreme sub-daily precipitation, surface temperature, and relative humidity:

RELATIONSHIP BETWEEN PRECIP, TEMP, AND RH. *Geophysical Research Letters*, *37*(22), n/a-n/a. https://doi.org/10.1029/2010GL045081

Holmes, J. D., & Moriarty, W. W. (1999). Application of the generalized Pareto distribution to extreme value analysis in wind engineering. *Journal of Wind Engineering and Industrial Aerodynamics*, *83*(1–3), 1–10. https://doi.org/10.1016/S0167-6105(99)00056-2

Hosking, J. R. M. (1990). L-Moments: Analysis and Estimation of Distributions Using Linear Combinations of Order Statistics. *Journal of the Royal Statistical Society. Series B (Methodological)*, *52*(1), 105–124.

Jenkinson, A. F. (1955). The frequency distribution of the annual maximum (or minimum) values of meteorological elements. *Quarterly Journal of the Royal Meteorological Society*, *81*(348), 158–171. https://doi.org/10.1002/qj.49708134804

Kendon, E. J., Roberts, N. M., Fowler, H. J., Roberts, M. J., Chan, S. C., & Senior, C. A. (2014). Heavier summer downpours with climate change revealed by weather forecast resolution model. *Nature Climate Change*, *4*(7), 570–576. https://doi.org/10.1038/nclimate2258

Kharin, V. V., Zwiers, F. W., Zhang, X., & Hegerl, G. C. (2007). Changes in Temperature and Precipitation Extremes in the IPCC Ensemble of Global Coupled Model Simulations. *Journal of Climate*, *20*(8), 1419–1444. https://doi.org/10.1175/JCLI4066.1

Kharin, V. V., Zwiers, F. W., Zhang, X., & Wehner, M. (2013). Changes in temperature and precipitation extremes in the CMIP5 ensemble. *Climatic Change*, *119*(2), 345–357. https://doi.org/10.1007/s10584-013-0705-8

Knist, S., Goergen, K., & Simmer, C. (2020). Evaluation and projected changes of precipitation statistics in convection-permitting WRF climate simulations over Central Europe. *Climate Dynamics*, *55*(1–2), 325–341. https://doi.org/10.1007/s00382-018-4147-x

Kodra, E., Steinhaeuser, K., & Ganguly, A. R. (2011). Persisting cold extremes under 21st-century warming scenarios: GLOBAL WARMING AND COLD EXTREMES. *Geophysical Research Letters*, *38*(8), n/a-n/a. https://doi.org/10.1029/2011GL047103

Kooperman, G. J., Pritchard, M. S., & Somerville, R. C. J. (2014). The response of US summer rainfall to quadrupled CO_2 climate change in conventional and superparameterized versions of the NCAR community atmosphere model. *Journal of Advances in Modeling Earth Systems*, *6*(3), 859–882. https://doi.org/10.1002/2014MS000306

Koutsoyiannis, D. (2004). Statistics of extremes and estimation of extreme rainfall: I. Theoretical investigation / Statistiques de valeurs extrêmes et estimation de précipitations extrêmes: I. Recherche théorique. *Hydrological Sciences Journal*, *49*(4), 3. https://doi.org/10.1623/hysj.49.4.575.54430

Lenderink, G., & Fowler, H. J. (2017). Understanding rainfall extremes. *Nature Climate Change*, *7*(6), 391–393. https://doi.org/10.1038/nclimate3305

Lenderink, G., Mok, H. Y., Lee, T. C., & Van Oldenborgh, G. J. (2011). Scaling and trends of hourly precipitation extremes in two different climate zones – Hong Kong and the Netherlands. *Hydrology and Earth System Sciences*, *15*(9), 3033–3041. https://doi.org/10.5194/hess-15-3033-2011

Libertino, A., Allamano, P., Laio, F., & Claps, P. (2018). Regional-scale analysis of extreme precipitation from short and fragmented records. *Advances in Water Resources*, *112*, 147–159. https://doi.org/10.1016/j.advwatres.2017.12.015

Lind, P., Belušić, D., Christensen, O. B., Dobler, A., Kjellström, E., Landgren, O., Lindstedt, D., Matte, D., Pedersen, R. A., Toivonen, E., & Wang, F. (2020). Benefits and added value of convection-permitting climate modeling over Fenno-Scandinavia. *Climate Dynamics*, *55*(7–8), 1893–1912. https://doi.org/10.1007/s00382-020-05359-3

Liu, B., Tan, X., Gan, T. Y., Chen, X., Lin, K., Lu, M., & Liu, Z. (2020). Global atmospheric moisture transport associated with precipitation extremes: Mechanisms and climate change impacts. *WIREs Water*, *7*(2). https://doi.org/10.1002/wat2.1412

Mailhot, A., & Duchesne, S. (2010). Design Criteria of Urban Drainage Infrastructures under Climate Change. *Journal of Water Resources Planning and Management*, *136*(2), 201–208. https://doi.org/10.1061/(ASCE)WR.1943-5452.0000023

Mamoon, A. A., Rahman, A., & Joergensen, N. E. (2019). Assessment of Climate Change Impacts on IDF Curves in Qatar Using Ensemble Climate Modeling Approach. In S. K. Singh & C. T. Dhanya (Eds.), *Hydrology in a Changing World* (pp. 153–

169). Springer International Publishing. https://doi.org/10.1007/978-3-030-02197-9_7

Marani, M., & Ignaccolo, M. (2015). A metastatistical approach to rainfall extremes. *Advances in Water Resources*, *79*, 121–126. https://doi.org/10.1016/j.advwatres.2015.03.001

Maraun, D., Wetterhall, F., Ireson, A. M., Chandler, R. E., Kendon, E. J., Widmann, M., Brienen, S., Rust, H. W., Sauter, T., Themeßl, M., Venema, V. K. C., Chun, K. P., Goodess, C. M., Jones, R. G., Onof, C., Vrac, M., & Thiele-Eich, I. (2010). Precipitation downscaling under climate change: Recent developments to bridge the gap between dynamical models and the end user. *Reviews of Geophysics*, *48*(3), RG3003. https://doi.org/10.1029/2009RG000314

Marra, F., Borga, M., & Morin, E. (2020). A Unified Framework for Extreme Subdaily Precipitation Frequency Analyses Based on Ordinary Events. *Geophysical Research Letters*, *47*(18). https://doi.org/10.1029/2020GL090209

Marra, F., Nikolopoulos, E. I., Anagnostou, E. N., & Morin, E. (2018). Metastatistical Extreme Value analysis of hourly rainfall from short records: Estimation of high quantiles and impact of measurement errors. *Advances in Water Resources*, *117*, 27–39. https://doi.org/10.1016/j.advwatres.2018.05.001

Martel, J.-L., Brissette, F. P., Lucas-Picher, P., Troin, M., & Arsenault, R. (2021). Climate Change and Rainfall Intensity–Duration–Frequency Curves: Overview of Science and Guidelines for Adaptation. *Journal of Hydrologic Engineering*, *26*(10), 03121001. https://doi.org/10.1061/(ASCE)HE.1943-5584.0002122

Martel, J.-L., Mailhot, A., & Brissette, F. (2020). Global and Regional Projected Changes in 100-yr Subdaily, Daily, and Multiday Precipitation Extremes Estimated from Three Large Ensembles of Climate Simulations. *Journal of Climate*, *33*(3), 1089–1103. https://doi.org/10.1175/JCLI-D-18-0764.1

Meredith, E. P., Ulbrich, U., Rust, H. W., & Truhetz, H. (2021). Present and future diurnal hourly precipitation in 0.11° EURO-CORDEX models and at convection-permitting resolution. *Environmental Research Communications*, *3*(5), 055002. https://doi.org/10.1088/2515-7620/abf15e

Milly, P. C. D., Betancourt, J., Falkenmark, M., Hirsch, R. M., Kundzewicz, Z. W., Lettenmaier, D. P., & Stouffer, R. J. (2008). Stationarity Is Dead: Whither Water Management? *Science*, *319*(5863), 573–574. https://doi.org/10.1126/science.1151915

Min, S.-K., Zhang, X., Zwiers, F. W., & Hegerl, G. C. (2011). Human contribution to more-intense precipitation extremes. *Nature*, *470*(7334), 378–381. https://doi.org/10.1038/nature09763

Miniussi, A., & Marani, M. (2020). Estimation of Daily Rainfall Extremes Through the Metastatistical Extreme Value Distribution: Uncertainty Minimization and Implications for Trend Detection. *Water Resources Research*, *56*(7). https://doi.org/10.1029/2019WR026535

Myhre, G., Alterskjær, K., Stjern, C. W., Hodnebrog, Ø., Marelle, L., Samset, B. H., Sillmann, J., Schaller, N., Fischer, E., Schulz, M., & Stohl, A. (2019). Frequency of extreme precipitation increases extensively with event rareness under global

warming. *Scientific Reports*, *9*(1), 16063. https://doi.org/10.1038/s41598-019-52277-4

O'Gorman, P. A. (2015). Precipitation Extremes Under Climate Change. *Current Climate Change Reports*, *1*(2), 49–59. https://doi.org/10.1007/s40641-015-0009-3

O'Gorman, P. A., & Schneider, T. (2009). The physical basis for increases in precipitation extremes in simulations of 21st-century climate change. *Proceedings of the National Academy of Sciences*, *106*(35), 14773–14777. https://doi.org/10.1073/pnas.0907610106

Orr, H. G., Ekström, M., Charlton, M. B., Peat, K. L., & Fowler, H. J. (2021). Using high-resolution climate change information in water management: A decision-makers' perspective. *Philosophical Transactions of the Royal Society A: Mathematical, Physical and Engineering Sciences*, *379*(2195), 20200219. https://doi.org/10.1098/rsta.2020.0219

Otten, A., & Van Montfort, M. A. J. (1980). Maximum-likelihood estimation of the general extreme-value distribution parameters. *Journal of Hydrology*, *47*(1–2), 187–192. https://doi.org/10.1016/0022-1694(80)90056-6

Pfahl, S., O'Gorman, P. A., & Fischer, E. M. (2017). Understanding the regional pattern of projected future changes in extreme precipitation. *Nature Climate Change*, *7*(6), 423–427. https://doi.org/10.1038/nclimate3287

Pickands, J. (1975). Statistical Inference Using Extreme Order Statistics. *The Annals of Statistics*, *3*(1), 119–131.

Pisarenko, V. F., & Sornette, D. (2003). Characterization of the Frequency of Extreme Earthquake Events by the Generalized Pareto Distribution. *Pure and Applied Geophysics*, *160*(12), 2343–2364. https://doi.org/10.1007/s00024-003-2397-x

Poujol, B., Mooney, P. A., & Sobolowski, S. P. (2021). Physical processes driving intensification of future precipitation in the mid- to high latitudes. *Environmental Research Letters*, *16*(3), 034051. https://doi.org/10.1088/1748-9326/abdd5b

Prein, A. F., Rasmussen, R. M., Ikeda, K., Liu, C., Clark, M. P., & Holland, G. J. (2017). The future intensification of hourly precipitation extremes. *Nature Climate Change*, *7*(1), 48–52. https://doi.org/10.1038/nclimate3168

Prescott, P., & Walden, A. T. (1980). Maximum likelihood estimation of the parameters of the generalized extreme-value distribution. *Biometrika*, *67*(3), 723–724. https://doi.org/10.1093/biomet/67.3.723

Rosenberg, E. A., Keys, P. W., Booth, D. B., Hartley, D., Burkey, J., Steinemann, A. C., & Lettenmaier, D. P. (2010). Precipitation extremes and the impacts of climate change on stormwater infrastructure in Washington State. *Climatic Change*, *102*(1–2), 319–349. https://doi.org/10.1007/s10584-010-9847-0

Schlef, K. E., Kunkel, K. E., Brown, C., Demissie, Y., Lettenmaier, D. P., Wagner, A., Wigmosta, M. S., Karl, T. R., Easterling, D. R., Wang, K. J., François, B., & Yan, E. (2023). Incorporating non-stationarity from climate change into rainfall frequency and intensity-duration-frequency (IDF) curves. *Journal of Hydrology*, *616*, 128757. https://doi.org/10.1016/j.jhydrol.2022.128757

Singleton, A., & Toumi, R. (2013). Super-Clausius-Clapeyron scaling of rainfall in a model squall line. *Quarterly Journal of the Royal Meteorological Society*, *139*(671), 334–339. https://doi.org/10.1002/qj.1919

Smith, R. L. (1989). Extreme Value Analysis of Environmental Time Series: An Application to Trend Detection in Ground-Level Ozone. *Statistical Science*, *4*(4). https://doi.org/10.1214/ss/1177012400

Sun, Y., Solomon, S., Dai, A., & Portmann, R. W. (2007). How Often Will It Rain? *Journal of Climate*, *20*(19), 4801–4818. https://doi.org/10.1175/JCLI4263.1

Tabari, H. (2020). Climate change impact on flood and extreme precipitation increases with water availability. *Scientific Reports*, *10*(1), 13768. https://doi.org/10.1038/s41598-020-70816-2

Trenberth, K. E. (1999). [No title found]. *Climatic Change*, *42*(1), 327–339. https://doi.org/10.1023/A:1005488920935

Trenberth, K. E., Dai, A., Rasmussen, R. M., & Parsons, D. B. (2003). The Changing Character of Precipitation. *Bulletin of the American Meteorological Society*, *84*(9), 1205–1218. https://doi.org/10.1175/BAMS-84-9-1205

Utsumi, N., Seto, S., Kanae, S., Maeda, E. E., & Oki, T. (2011). Does higher surface temperature intensify extreme precipitation?: TEMPERATURE AND EXTREME RAINFALL. *Geophysical Research Letters*, *38*(16), n/a-n/a. https://doi.org/10.1029/2011GL048426

Vanden Broucke, S., Wouters, H., Demuzere, M., & Van Lipzig, N. P. M. (2019). The influence of convection-permitting regional climate modeling on future projections of extreme precipitation: Dependency on topography and timescale.

Climate Dynamics, *52*(9–10), 5303–5324. https://doi.org/10.1007/s00382-018-4454-2

Wasko, C., Sharma, A., & Johnson, F. (2015). Does storm duration modulate the extreme precipitation-temperature scaling relationship?: EFFECT OF STORM DURATION ON SCALING. *Geophysical Research Letters*, *42*(20), 8783–8790. https://doi.org/10.1002/2015GL066274

Wehner, M. F. (2013). Very extreme seasonal precipitation in the NARCCAP ensemble: Model performance and projections. *Climate Dynamics*, *40*(1–2), 59–80. https://doi.org/10.1007/s00382-012-1393-1

Westra, S., Fowler, H. J., Evans, J. P., Alexander, L. V., Berg, P., Johnson, F., Kendon, E. J., Lenderink, G., & Roberts, N. M. (2014). Future changes to the intensity and frequency of short-duration extreme rainfall: FUTURE INTENSITY OF SUB-DAILY RAINFALL. *Reviews of Geophysics*, *52*(3), 522–555. https://doi.org/10.1002/2014RG000464

Zhang, X., Zwiers, F. W., Li, G., Wan, H., & Cannon, A. J. (2017). Complexity in estimating past and future extreme short-duration rainfall. *Nature Geoscience*, *10*(4), 255–259. https://doi.org/10.1038/ngeo2911

Zorzetto, E., Botter, G., & Marani, M. (2016). On the emergence of rainfall extremes from ordinary events: EXTREMES EMERGE FROM ORDINARY EVENTS. *Geophysical Research Letters*, *43*(15), 8076–8082. https://doi.org/10.1002/2016GL069445

CSA (Canadian Standards Association). 2019. Technical guide: Development, interpretation and use of rainfall intensity-duration-frequency (IDF) information: Guideline for Canadian water resources practitioners. Mississauga, ON, Canada: CSA.

Ball, J., M. Basbister, R. Nathan, W. WEeks, E. Weinmann, M. Retallick, and I. Testoni. 2019. Australian rainfall and runoff: A guide to flood estimation, 1526. Symonston, ACT, Australia: Commonwealth of Australia (Geoscience Australia).